



Norwegian University of
Science and Technology

Time-lapse Processing of 2D Seismic over the Japan Trench

Arindam Guha

Master of Science in Petroleum Geoscience and Engineering

Submission date: June 2018

Supervisor: Børge Arntsen, IGP

Norwegian University of Science and Technology
Department of Geoscience and Petroleum

Abstract

The seismic surveys SR97-101 (baseline) and D19 (monitor), acquired over the Japan Trench, were processed using an open-source software (*Madagascar*) with aims on detecting changes from the Tohoku-Oki earthquake. The surveys were interpolated to a datum plane using a modified Shepard algorithm together with differential NMO function to fix the source and receiver coordinates. The data were then processed through frequency filter, despiking, debubble filter, and top mute. After sorting the data into CMP gathers, velocity scanning and picking were used with inner muted semblances in order to avoid picking of multiples when using an automatic picking algorithm. The data were NMO corrected with smoothed velocity models where the monitor survey had refractive events being overcorrected at shallow depths, which were solved by reducing the fold prior to stacking. The data were then stacked to observe the first seismic images of the subduction zone.

The CMP gathers were then processed through a Kirchhoff pre-stack time migration and an experimental depth migration was performed using the full acoustic wave pre-stack migration on the common shot gathers. Similar overcorrections were observed on the shallow depth common offset image gathers obtained from the time migration, and where the monitor survey went through similar procedures done prior to stacking. The migrated stacks were converted to SEG-Y format for interpretation in Petrel where the baseline survey was shifted to the east due to problems with the navigation and to make the stacks comparable. Horst and graben structures, thrust complex, and deformations zone were characterized on the baseline survey and compared with the monitor survey. 11.84 m uplift was observed on the backstop interface on the Okhotsk Plate while 5.92 m subsidence was observed on the Oceanic Plate near the trench with high uncertainties due to the navigational shift. Large changes on the horst structure on the Okhotsk Plate were also observed, but discussed to be unrealistic. The depth migration was unstable due to unstable depth velocity models and resulted in depth errors, but managed to image reflectors at shallow depth with better resolution compared to the time migration.

Sammendrag

De seismiske linjene SR97-101 (grunnlinjen) og D19 (overvåkningslinjen), samlet inn over den japanske dyphavsgropen, ble prosessert med en åpen kildekode (*Madagascar*) med formål om å observere endringer oppstått på grunn av Tohoku-Okijordskjelvet. Linjene ble interpolert til et datumplan ved bruk av en modifisert Shepard-algoritme sammen med en differensial NMO funksjon for å korrigere kilde og receiver mottakere. Dataene ble prosessert gjennom frekvenskorrigering, fjerning av "boble-effekt" og støy. Etter CMP-sortering ble det utført hastighetsanalyse og hastighetsplukking med innvendig fjerning av semblance-verdier for å unngå plukk av multipler under bruk av en automatisk hastighetsplukker. Dataene ble NMO-korrigert med glattede hastighetsmodeller der overvåkningslinjen hadde overkorrigerte refraksjonssignaler på grunne dyp som ble fikset ved å redusere folds før stacking. Deretter ble dataene stacked for å observere de første seismiske avbildningene av subduksjonsonen.

CMP-dataene ble brukt til en Kirchhoff før-stack migrasjon og en eksperimentell dybdemigrasjon med full akustisk før-stack bølgemigrasjon ble gjennomført med "common shot" data. Små overkorreksjoner ble observert på grunne deler av "common offset image" data fra tidsmigrasjonen, og hvor overvåkningslinjen måtte gjennom samme prosedyrer gjort før stacking. Migrerte data ble konvertert til SEG-Y format og tolket i Petrel hvor grunnlinjen ble forskjøvet til øst på grunn av feil med navigasjonen og for å sammenligne linjene. Horst og graben strukturer, skyvedekker og deformasjoner ble observert i grunnlinjen, og sammenlignet med overvåkningslinjen. 11.84 m heving ble observert på toppen av deformasjonssonen på Okhotsk-platen mens 5.92 m synkning ble observert på stillehavsplaten nær dyphavsgropen med forbeholdt usikkerhet grunnen naviasjonsforskyvningen. Store endringer ble også observert på horst strukturen på Okhotsk-platen, men diskutert om å være urealistisk. Dybdemigrasjonen var ustabil på grunn av ustabile dybde-hastighetsmodeller og ga feil dybde på linjene, men klarte å vise tydeligere reflektorer på grunne dyp med bedre oppløsning sammenlignet med tidsmigrasjonen.

Preface

The thesis consists of a processing sequence done on time-lapse seismic crossing the Japan trench, before and after the Tohoku earthquake in 2011. The thesis is written during spring 2018, and is a final product from the specialization course TPG4570. My supervisor has been Professor Børge Arntsen.

Norwegian University of Science and Technology in Trondheim, June 2018

Arindam Guha

Acknowledgement

This master thesis has been carried out at the Norwegian University of Science and Technology under the supervision of Professor Børge Arnsten.

I would like to express my gratitude to my supervisor for providing this exciting project. His support, feedback and guidance through the semester has helped me a long way, and at the end helped me to complete this thesis.

I would also like to thank Associated Professor Wiktor Weibull for helping me from Stavanger. Learning Madagascar as an open-source software has been exciting, challenging and tough with long days. Hence, I am grateful to be provided this opportunity with great mentors.

I would like to thank my father Ashis Kumar Guha, my mother Mita Guha, my girlfriend Ann Isabel C. Rosvoll and her parents for their love and support.

Five years of studying have proven to be a fun and challenging road and I am proud to take this further with me in life.

*Good, better, best.
Never let it rest.
'Til your good is better and your better is best.
- St. Jerome.*

Norwegian University of Science and Technology in Trondheim, June 2018

Arindam Guha

Contents

Abstract	i
Sammendrag	ii
Preface	iii
Acknowledgement	iv
List of Figures	vii
List of Tables	xiii
1 Introduction	1
1.1 Area of interest	1
1.2 Objectives and previous work	4
1.3 Structure of the thesis	5
2 Tectonic and geological history	6
3 Theory	9
3.1 Seismic Acquisition	9
3.1.1 Time-lapse seismic acquisition	10
3.1.2 Bubble signal	11
3.1.3 Ghost reflector	11
3.1.4 Wavelet shapes and phases	12
3.2 Time-lapse Datum Correction	13
3.3 Main Time-lapse Processing Steps	13
3.3.1 Resampling	14
3.3.2 Gain correction	15
3.3.3 Shot to CMP	15
3.3.4 Mute	16
3.3.5 Velocity analysis, NMO correction and stacking	16
3.3.6 Filtering of seismic data	18
3.3.7 Migration	19
4 Data	22
4.1 Acquisition parameters	22
4.2 Problems with the data	24

5	Methods	25
5.1	Madagascar processing software	25
5.2	Data Regulation and geometry correction	25
5.2.1	Modified Shepard's method and differential NMO	28
5.3	Frequency filter and despiking	29
5.4	Debubbling filter	30
5.5	Muting	33
5.6	CMP sorting	35
5.7	Velocity analysis, NMO correction and stacking	37
5.8	Pre-stack migration	42
5.8.1	Kirchhoff migration	42
5.8.1.1	Procedure in Madagascar	43
5.8.2	Full acoustic wave migration	44
5.8.2.1	Procedure in Madagascar	45
5.9	Conversion from RSF to SEG-Y	46
6	Results	47
6.1	Processing results	47
6.2	Pre-stack time migration	59
6.3	Seismic interpretation and observation	62
6.3.1	Time-lapse interpretation	64
6.4	Pre-stack depth migration	69
7	Discussion	75
8	Conclusion and recommendation	79
	References	83
	Appendices	
A	Madagascar processing workflow	I
A.1	Data regulation and geometry correction	I
A.2	Frequency filter, despiking and debubble filter	II
A.3	Top mute	II
A.4	CMP sorting, velocity analysis, NMO correction and stacking	III
A.5	Kirchhoff Pre-stack time migration	V
A.6	Full acoustic wave pre-stack depth migration	V
A.7	Amplitude correction and Conversion from RSF to SGY	VII
B	Figures	VIII

List of Figures

1.1	A: Tectonic settings in the northeastern parts of Japan where the red arrows shows the relative motion between the plate boundaries. B: Distribution of previous earthquakes where the most recent are highlighted in yellow stars. Edited from Ozawa et al. (2011).	2
1.2	Plot of seismic moment rate functions for the largest magnitude earthquakes in history, i.e. Tohoku-Oki, Alaska, Sumatra-Andaman, Chile, and Hokkaidō. The Tohoku-Oki earthquake was recorded with the highest seismic moment rate and shortest duration in history. Figure from Lay and Kanamori (2011).	3
1.3	Bathymetric map of the Japan Trench with the 2D seismic lines acquired prior and after the Tohoku-Oki earthquake. The monitor surveys are highlighted in orange. Figure provided from personal communication (Arntsen, 2017).	4
2.1	Schematic illustration showing the breakup of Rodinia (Late Proterozoic supercontinent) by a Pacific super plume and evolution of the Pacific rim. Figure edited from Taira (2001).	6
2.2	Schematic illustration showing the supercontinent Pangea and possible location of proto-Japan during the Late Permian and Late Jurassic period. Figure from Taira (2001).	7
2.3	Schematic reconstruction from 130 Ma. Figure from Taira (2001).	8
3.1	A schematic illustration of marine 2D seismic acquisition where a vessel tows one source parallel with one towed seismic receiver lines. Figure edited from Rigzone (2017).	10
3.2	Illustration of cable feathering and streamer curvature. Figure edited from Gadallah and Fisher (2005).	10
3.3	Typical source signature where Primary (P) and Bubble (B) signals are observed. The ghost reflection of the Primary signal is marked by the red arrow. Figure edited from Landrø (2011).	11
3.4	Illustration of ghost reflection and its frequency pattern. Figure from McGuire and Miller (1989) and Gadallah and Fisher (2005).	12
3.5	Typical wavelets used for scenarios of increasing and decreasing Acoustic Impedance (AI). Figure from Simm and White (2002).	12
3.6	Illustration of field static correction. Figure from Landrø (2011).	13
3.7	A typical shot recorded and displayed in shot domain. The offset is plotted against travelttime to observe the waves recorded. Figure edited from (Onajite, 2013).	14
3.8	Example of Gain correction. Figure edited from (Onajite, 2013).	15

3.9	Schematic illustration of gathers. Figure edited from (Hardy, 1999). . . .	15
3.10	Before and after Top mute of a shot gather. The green ellipses illustrates areas of noise, while the red line shows the selected “Top Mute”. . . .	16
3.11	Schematic illustration of NMO correction and stacking of one reflection. Figure edited from (Hardy, 1999).	17
3.12	Schematic illustration of Ormsby filter types. Figure edited from (Hardy, 1999).	18
3.13	Left figure shows the F-K domain of a CMP gather. Middle and right figures illustrate the primary and multiple reflection in F-K domain with NMO correction where primaries are overcorrected. Figure edited from Hardy (1999) and Landrø (2011).	19
3.14	Illustration of the effect of migration on dipping layer reflection. Figure edited from Gadallah and Fisher (2005) and Schulte (2012).	20
3.15	Illustration of an anticline before and after migration. Migration collapses the bow-ties to reveal the true image of the layer.	20
4.1	Schematic model of seismic acquisition parameters for the baseline (SR97-101) and monitor (D19) surveys. The red dot illustrates the source (air gun) and the red triangle is the Buoy tail attached at the end of the streamer cable. Edited from Hardy (1999).	23
5.1	Source and Receiver coordinates for the monitor survey D19 with selected intervals for each trace-coordinate.	26
5.2	Source and Receiver coordinates for the monitor survey D19 with selected intervals for each trace-coordinate after applying the parameters in Table 5.1. The red polygon illustrates the pre-defined datum plane used for the interpolation with parameters from Table 4.1. .	27
5.3	Frequency spectrum of the raw baseline and monitor surveys.	29
5.4	Frequency spectrum of the baseline and monitor survey after applying a band-pass filter with low-cut of 3 Hz and high-cut of 50Hz.	29
5.5	Trace display of the direct wave and first reflection response at small offset from the baseline (a-c) and monitor surveys (d-f).	30
5.6	Desired source wavelets for the monitor and baseline surveys. The wavelets were created with emphasize on the first reflection shape, but began at the travelttime similar to the direct wave recorded at small offset.	31
5.7	Trace display before and after applying debubble filter on the first reflection response at small, medium, and large offsets and depth. . . .	32
5.8	Shot gather of shallow depth events from the baseline (a-c) and monitor surveys (d-f). The debubbled shot gather is also despiked.	33
5.9	Shot gather of shallow, medium, and deep depth events from the baseline (a-c) and monitor surveys (d-f) after applying top mute. . . .	34
5.10	CMP gather from the baseline survey before and after CMP trace removal (a-b) and a CMP gather of the monitor survey (c) at Location 1 (L1). Their locations are set to be approximately the same. The amplitudes are multiplied by 100 and 1000, respectively for display. The resolution is poor due to the CMP spacing, which was 25 m in the baseline survey and 6.25 m in the monitor survey.	36

5.11	CMP gather at three locations (L1, L2, L3) with their corresponding velocity semblances before and after inner mute. The locations are approximated to be at the same location in both surveys for comparison. The TWT (y-axis) of the CMP gathers are shortened to illustrate the NMO curvatures at the various depths/locations. The CMP gathers were also interpolated to create a smoother display.	40
5.12	Subsurface model of the Kirchhoff pre-stack time migration. Figure from Bancroft et al. (1998).	42
5.13	Schematically illustration of the reserve migration in two-space dimension. The wavefield is injected from the recorded maximum surface t_{max}	44
5.14	Source wavelet and corresponding frequency spectrum used for both surveys.	45
6.1	Comparison of shallow unmigrated stack before and after debubbling filter and gain correction on the baseline (a-c) and monitor (d-f) surveys. The bubble was observed as a strong continuous reflection. For location, see B1 and M1 in Fig. 6.8.	47
6.2	Frequency spectrum of the debubbled baseline and monitor surveys. The low amplitude decays are observed as the destructive primary-ghost interference.	48
6.3	The direct wave response from small offset from the baseline (a) and monitor (b) surveys before and after applying the debubble filter (and band-pass filter). Bubble residue are present after the filter.	49
6.4	Comparison of velocity profiles at the three CMP locations (L1,L2,L3) before and after semblance mute, and after smoothing. The red circles mark the areas that indicated picked velocities of multiple reflections. However, there are also some multiples picked outside these circles. See Fig. 5.11 for their corresponding CMP gather and semblance scans. . . .	52
6.5	Velocity model obtained from performing the velocity analysis and automatic picking for the baseline survey without dividing the CMP data prior to the velocity analysis. The anomalies are marked with the arrows where velocities higher than 1480 m/s have been picked.	53
6.6	Velocity models for the surveys obtained before and after semblance mute, and after smoothing of the semblance muted velocity models. . .	54
6.7	NMO corrected CMP gathers at the three locations. The total TWT has been limited for comparison. The folds from the monitor survey were reduced to 40 as displayed in Figs. 6.7g to 6.7i. The undercorrected reflections (red) are believed to be the multiples in the data while overcorrected event (green) is believed to be a refrational event.	55

6.8	Unmigrated stack (brute stack) of the surveys indicating large diffractions and the first observation of the subduction zone and the Japan trench. It can also be observed that the monitor survey is shorter than the baseline survey as expected and with more data acquired towards the West and a TWT up to 18 seconds. The brute stacks are obtained using the unmuted velocity semblance, which gave the velocity models displayed in Figs. 6.6a and 6.6b. Location 1 from the baseline survey (B1) and corresponding monitor survey (M1) are displayed in Fig. 6.1.	56
6.9	Unmigrated brute stack with amplitude recovery where the seabed and second layer strong reflection multiples are observed and marked. It can also be observed that there is a continuation of these multiples until the energy is lost at very large depths.	57
6.10	Unmigrated stack of the surveys after applying the semblance muted velocity model. The multiples are suppressed, but still visible.	58
6.11	NMO corrected COI gathers obtained from the Kirchhoff Pre-stack time migrations. Small overcorrections are observed at shallow depths while refractions are corrected as well for both surveys. These events are also destructive for large offset reflections in the monitor survey, and hence why the folds are reduced. The undercorrected reflections are the multiples in the data.	60
6.12	Time migrated stacks obtained using the semblance muted velocity models. The diffractions are collapsed, and the reflectors moved to their true positions. The migration method assumed only one ray path. Multiples are still weakly present in both surveys.	61
6.13	Polarity of the seismic wavelet.	62
6.14	Seismic interpretation of various layers and faults on the time migrated baseline survey. The stack is ten time vertically exaggerated. Strong continuous reflections was observed at the Pacific Plate with horst and graben structures along a series of normal faulting. Contourite and contourite channels were also interpreted close to the trench where the uppermost oceanic marine sediments were believed to be scraped as it closes the trench. The Pacific Plate was observed to subduct beneath the Okhotsk Plate with possible interaction with the Okhotsk Plate in an up-dip manner (marked by light green polygon and the question mark). The Japan Trench is observed at approximately 9.8-10 s.	63
6.15	Reduced time migrated stack of the baseline and monitor survey. Irrelevant parts of both surveys are removed to make them comparable.	65
6.16	Time-lapse observation of the horst structure. The red polygons illustrate the interpreted horizon and faults on the monitor survey while the green polygon are from the baseline survey. The changes in amplitudes on the monitor survey made it difficult to observe the continuation of the reflector on the left side of the horst structure. As drawn, two new fault were observed to be present in the monitor survey. For location, see B2 and M2 in Fig. 6.15.	66
6.17	Time-lapse comparison of the seabed changes on the backstop interface. An uplift of 16ms was observed at highest. For location, see B3 and M3 in Fig. 6.15.	67

6.18	Time-lapse comparison of the subduction zone near the trench. Only polygons interpreted at the monitor survey are displayed on the baseline survey, since differences were difficult to observe. The top of the Oceanic plate was be observed by some continuous reflectors subducting below the Okhotsk Plate. For location, see B4 and M4 in Fig. 6.15.	67
6.19	Time-lapse comparison of the seabed changes on the Oceanic Plate close to the trench. A subsidence of approximately average of 8ms was observed. For location, see B5 and M5 in Fig. 6.15.	68
6.20	Reduced velocity model for comparing. Large velocity changes are observed where velocity reduction is observed near the trench and across the Oceanic Moho interface.	68
6.21	Velocity models obtained from Dix conversion. The Dix conversion converted the velocities to interval velocities where it can be clearly observed that there are some low velocities present in between layer where it should theoretically increase, and an overestimation of high velocities near the trench observed in layers on the continental plate near close to the trench.	70
6.22	Velocity models obtained from the depth conversion. These have also been smoothed to avoid the low velocities at high depths. Low velocities at deep depths are still visible in the baseline and not the monitor velocity depth model.	70
6.23	Smoothed velocity model obtained from the depth conversion. These are also smoothed to eliminate low velocities at large depth, but these are however still present in the model.	70
6.24	Depth migrated stacks obtained by using the smoothed depth velocity models. The migration is very sensitive to the velocity changed, especially observed on the Oceanic Plate in the monitor survey, and which gave the unstable migration. The seabed in both surveys revealed to be SEG reverse polarities.	71
6.25	TQC stacks obtained from converting the depth migrated stack to time using the smoothed depth velocity model. The program <i>sfdepth2time</i> gave artificial noise at large depths that eliminates the reflectors, and assumed to be due to underestimation of the depths. The polarity in the data were revealed to be SEG negative.	72
6.26	Comparison of shallow sections from the baseline time migrated, depth migrated and TQC stacks. The seabed (blue polygon) was mapped on the time migrated stack and displayed on the TQC stack to observe the differences and errors in the migration. However, it could be clearly observed that both depth and TQC stacks were beneficial to image the shallow depths where onlap reflectors are observed toward the sequence boundary. Beware that SEG positive polarity is used in Fig. 6.26a while SEG negative is used in Figs. 6.26b and 6.26c. For location, see B6 on Figs. 6.24 and 6.25.	73

6.27	Comparison of shallow sections obtained from the monitor time migrated, depth migrated and TQC stack. The seabed (green polygon) was mapped on the time migrated stack and displayed on the TQC stack to observe the differences and errors in the migration. However, it could be clearly observed that both depth and TQC stacks were also beneficial to image the shallow depths where onlap reflectors are observed toward the sequence boundary. Beware that SEG positive polarity is used in Fig. 6.27a while SEG negative is used in Figs. 6.27b and 6.27c. For location, see M6 on Figs. 6.24 and 6.25.	74
7.1	A schematic illustration of the depth velocity model in the baseline survey. Figure from Jamstec (2015).	77
B.1	Sections of the baseline and monitor surveys, which are depth migrated stacks by Kwok et al. (2017) and Kodaira et al. (2017).	VIII

List of Tables

4.1	Acquisition parameters for the baseline and monitor surveys.	23
5.1	Shift and rotation parameters	26
5.2	3D geometry for the survey files in Madagascar.	28
5.3	Frequency notch calculated for source and receiver depths using Eq. 3.3.	29
5.4	Parameters for upper mute using Eq.5.1.	34
5.5	3D geometry for the CMP converted surveys.	35
5.6	3D geometry for the stacked surveys.	41
5.7	Transposed 3D geometry for the Kirchhoff pre-stack time migration.	43

1 | Introduction

Acquisition and processing of seismic data have had an enormous growth and focus the last two decades. It all evolved from classical earthquake studies in the 1900s to the beginning of Petroleum Exploration in the 1930s with aims to determine subsurface structures (Landrø and Amundsen, 2018). Seismic data have hence also been one of the first evidences to show co-seismic fault ruptures of a subduction zone where an earthquake breaches the seafloor and the trench axis. Many associate seismic data towards the Petroleum Exploration, but such studies of earthquakes and tectonic movements also show how important it is to implement this type of data. Nevertheless, the great importance of information revealed by imaging underground geology.

Introduction of computers in 1960s enabled geophysicists to process and image large amounts of data. During this period it was usual to collect two-dimensional (2D) seismic data acquired on land and at sea. The development of three-dimensional (3D) seismic began early in the 1970s and became a game changer for identifying subsurface geology (Landrø and Amundsen, 2018). Stronger computers, software, and processing techniques developed towards the 21st with better algorithms and faster processing time.

1.1 Area of interest

The northeastern parts of Japan are associated with 90 % of the world's earthquakes through history. The area, often called western parts of the Pacific Ring of Fire, has been exposed to various sudden sea-floor displacement occurring during the subduction process where the Pacific Plate is subducting beneath the Continental Okhotsk Plate (Fig. 1.1A). The Pacific Plate is subducting at a rate ranging from 8 to 8.5 cm/year and causing massive stress build up, which eventually burst out as massive energy during slip and causes the earthquakes. These could result in huge tsunamis entering populated areas nearby in Japan (Simons et al., 2011; Lay and Kanamori, 2011; Nakamura et al., 2013).

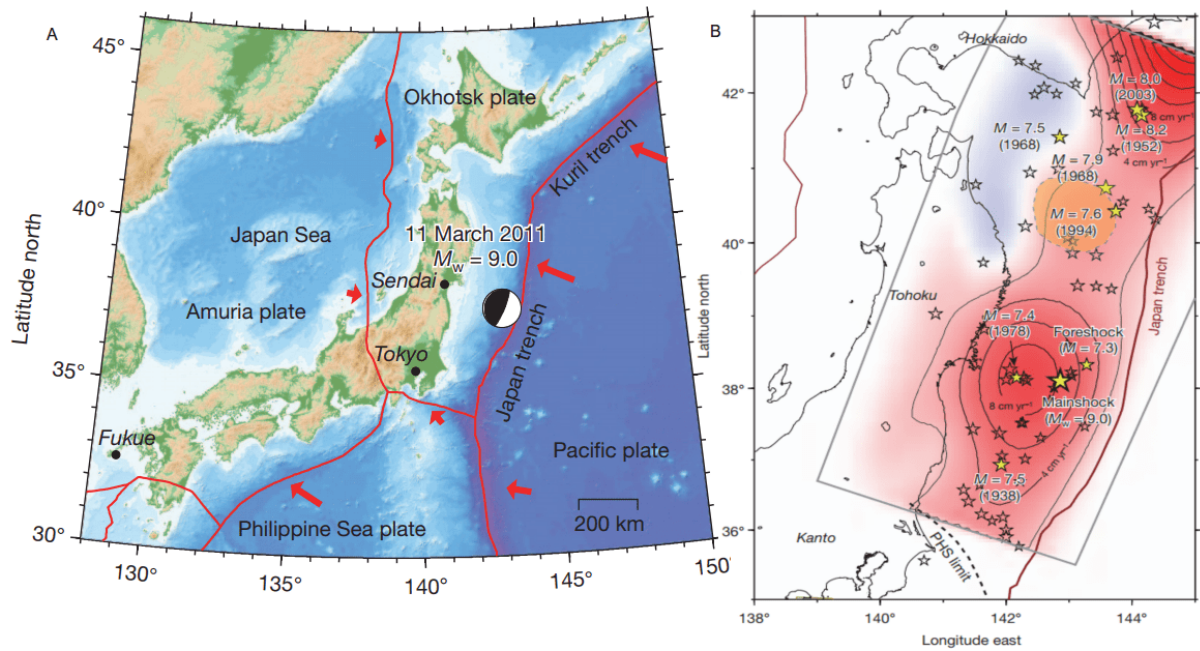


Figure 1.1: A: Tectonic settings in the northeastern parts of Japan where the red arrows shows the relative motion between the plate boundaries. B: Distribution of previous earthquakes where the most recent are highlighted in yellow stars. Edited from Ozawa et al. (2011).

There are records of massive earthquakes measured at magnitudes of 7 on the Richter Scale (Moment magnitude of $M_w = 7$) on the northeastern parts of the Japan Trench (Fig. 1.1B). Other records show surface-wave magnitudes up to 7.9 on the northernmost parts of the trench since 1923. There are only a few locations in the world that have experienced larger magnitudes than this, i.e. in areas such as Chile, Alaska, and Kamchatka (Ozawa et al., 2011; Lay and Kanamori, 2011).

On 11 March 2011, another massive earthquake occurred along the Japan Trench with its epicenter approximately 100 km off the coast of Sendai (Fig. 1.1). The earthquake, referred to as the Tohoku-Oki earthquake, had a magnitude of $M_w = 9$ that lasted for 150 seconds. This was definitely the largest earthquake with the highest seismic moment rate and shortest duration ever recorded (Fig. 1.2). The earthquake caused an uplift of 5 m covering 150 000 km^2 of the seafloor. Tsunami waves ranging 3-15 m were initiated and penetrated 10 km inland killing approximately 20 000 people and displaced half a million people from their homes. The high waves disrupted the Fukushima nuclear power plant and caused nuclear accidents spreading radiation (Lay and Kanamori, 2011).

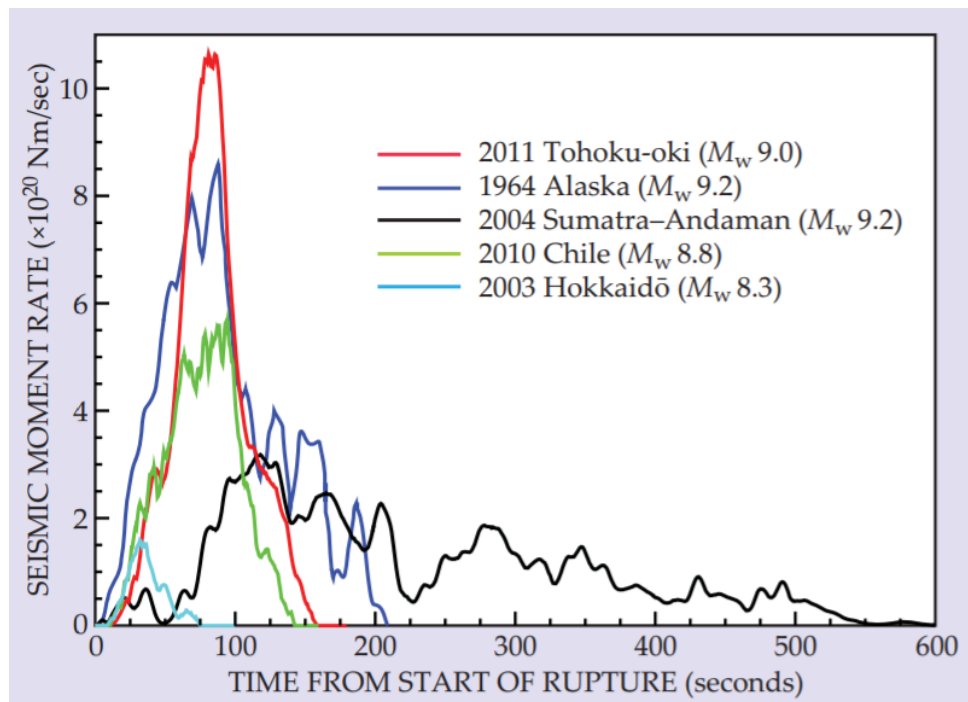


Figure 1.2: Plot of seismic moment rate functions for the largest magnitude earthquakes in history, i.e. Tohoku-Oki, Alaska, Sumatra-Andaman, Chile, and Hokkaidō. The Tohoku-Oki earthquake was recorded with the highest seismic moment rate and shortest duration in history. Figure from Lay and Kanamori (2011).

Large coseismic slip (30 - 60 cm) was revealed on the shallow parts of the plate boundary, which was based on seismological, geodetic and tsunami wave inversion studies. Bathymetric (waterdepth measurements) and seafloor geodetic research showed large displacement near the trench with movements of 50 m east - southeast and 7 - 10 m upwards (Simons et al., 2011; Ozawa et al., 2011; Fujii et al., 2011).

Collaborative marine seismic acquisition has been conducted by the Japan Marine Science and Technology Center (JAMSTEC), Tohoku University, and the Central Research Institute of Power Industry since 1997, and with motives to study and understand the physical process of crustal evolution and deformation of the Northeastern Japan arc. This particular arc has been related to several earthquakes that have occurred and of high interest for this purpose (Takahashi et al., 2000, 2004). The seismic reflection data have also been integrated with scientific drilling results by Deep Sea Drilling Projects (DSDP), Ocean Drilling Program (ODP) and others to establish a tectonic history where the Japan Trench is dominated by basal erosion (Nakamura et al., 2013).

A total of 3120 km of multichannel seismic (MCS) has been acquired by the vessel R/V Kairei from JAMSTEC. Among these, there are three particular 2D lines that have been acquired prior to and after the Tohoku-Oki earthquake (Fig. 1.3). These surveys were repeated as a part of a monitoring program to reveal co-seismic slip behaviours by comparison of the seismic sections (Tsuru et al., 2002).

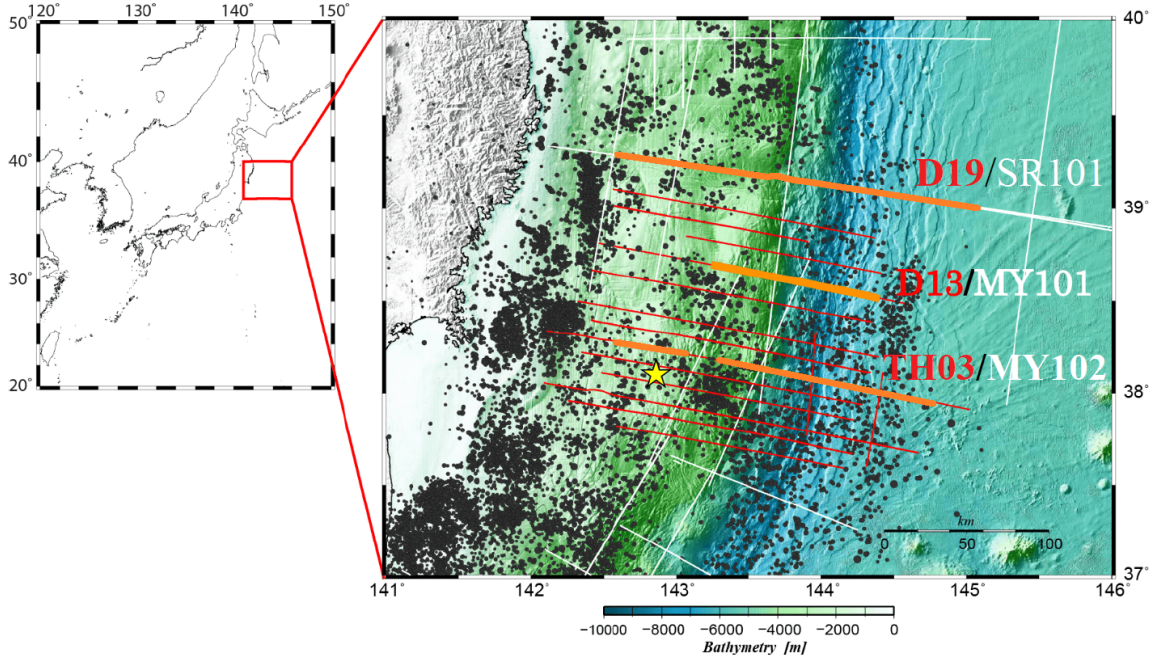


Figure 1.3: Bathymetric map of the Japan Trench with the 2D seismic lines acquired prior and after the Tohoku-Oki earthquake. The monitor surveys are highlighted in orange. Figure provided from personal communication (Arntsen, 2017).

1.2 Objectives and previous work

This thesis will aim at investigating the processing steps by focusing on time-lapse processing of the seismic lines SR97-101, acquired prior to the Tohoku-Oki earthquake, and D19, acquired after the earthquake. The seismic line SR97-101 has been processed earlier by Tsuru et al. (2000, 2002) and Takahashi et al. (2004) in the late 1990s when processing techniques were rapidly developing while D19 was acquired in the new technical era and processed by Boston et al. (2014), Kodaira et al. (2017), and Kwok et al. (2017). In the previous research regarding SR97-101, normal faulting on the oceanic plate were observed together with horst and graben structures. They also found evidence of the boundary between the oceanic layers and the upper mantle (Moho discontinuity) at approximately 12-13 km depth, and deformation fronts on the continental plate close to the trench. The recent studies of D19 indicated similar founding, but not compared in a time-lapse manner with SR971-101. Hence, there are limited studies of time-lapse seismic of these lines in recent time, and mark this of great interest.

A fairly new modern software *Madagascar* will be used to reprocess these surveys. It is an open-source software package with limited studies on real seismic data. However, it contains a wide range of capabilities, which will be used during the processing sequences. Reprocessing seismic data is an important aspect of processing to improve results from previous studies, which this paper will attempt on doing.

General acquisitions have often challenges related to navigation accuracy and gun (source) and receiver positions, which plays an enormous role for especially time-lapse processing. This paper will hence propose a method aiming at solving these issues related to the selected seismic surveys. Studies on the surveys had various methods to increase the resolution by performing pre-stack migrations after noise reductions such as trace-editing, multiple suppression etc. This paper will hence focus on comparing the results with these studies and also include a specific time and depth migration. The depth migration will however be presented as an experimental phase related to these surveys and not used to for the time-lapse comparison.

1.3 Structure of the thesis

The thesis will begin with the tectonic and geological history related to the study area followed by a theoretical chapter about 2D seismic processing related to time-lapse seismic. Next follows a description of the surveys and the methods used for processing the data. A pre-stack time migration of the baseline survey is already obtained from my specialization project, and the results will be used with some corrections and improvements. The obtained results from the time-lapse processing will hence be described and the migrated sections presented, followed by a seismic interpretation related to the obtained pre-stack time migrations. A own subsection will hence describe the experimental depth migration. At the end, a discussion of the results will be presented and compared with related papers.

2 | Tectonic and geological history

The Japanese arc system is known to have one of the longest geological history among the Western Pacific arcs. The oldest (low to medium pressure metamorphic ophiolites) and deep-water sedimentary rocks are discussed to be dated from Pre-Cambrian and Ordovician period and originate back to the breakup and rifting of Rodinia (Proterozoic supercontinent) (Fig. 2.1).

The Japanese arc began to grow on the margin of the proto-Asian continental block, which was gradually formed by the continental rifting blocks (cratons) Yangtze (South China), Sino-Korea (North Korea), and Siberia. The edges of the block changed from passive rift margin to an active subduction of the proto-Pacific ocean floor approximately 450 Ma, which then gave a gradually rise of the Japanese landmass (Fig. 2.1) (Taira, 2001; Barnes, 2003).

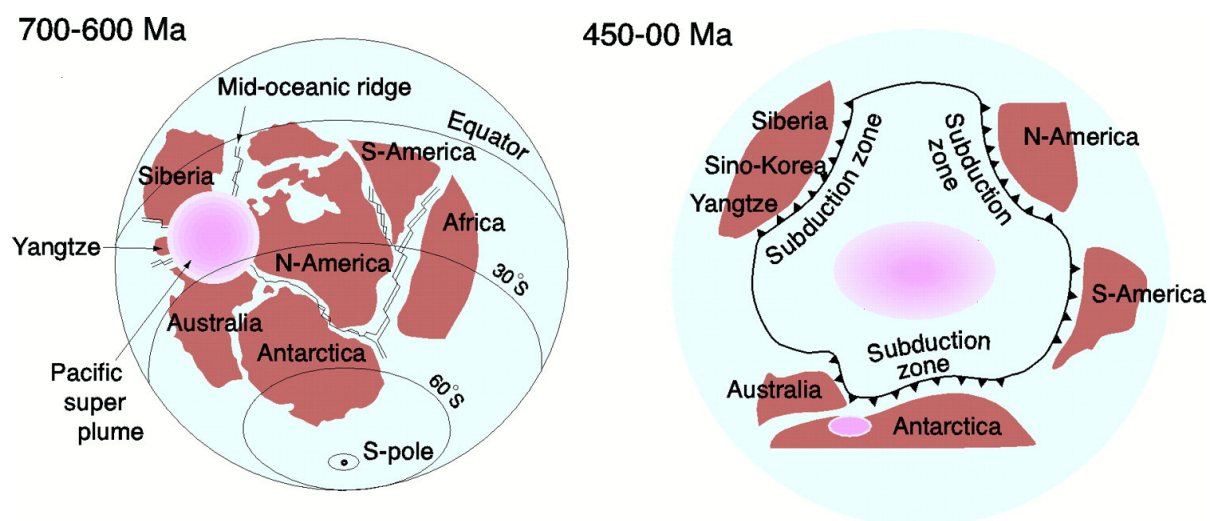


Figure 2.1: Schematic illustration showing the breakup of Rodinia (Late Proterozoic supercontinent) by a Pacific super plume and evolution of the Pacific rim. Figure edited from Taira (2001).

The continental blocks merged into the supercontinent Pangea approximately 250 Ma. The northern parts consisting of the blocks Sino-Korean and Yangtze among others later created the supercontinent Laurasia while the supercontinent Gondwana was formed in the south. The development of the proto-Japanese area took place as the eastern continental margin on the Yangtze block (Fig. 2.2) (Taira, 2001; Barnes, 2003).

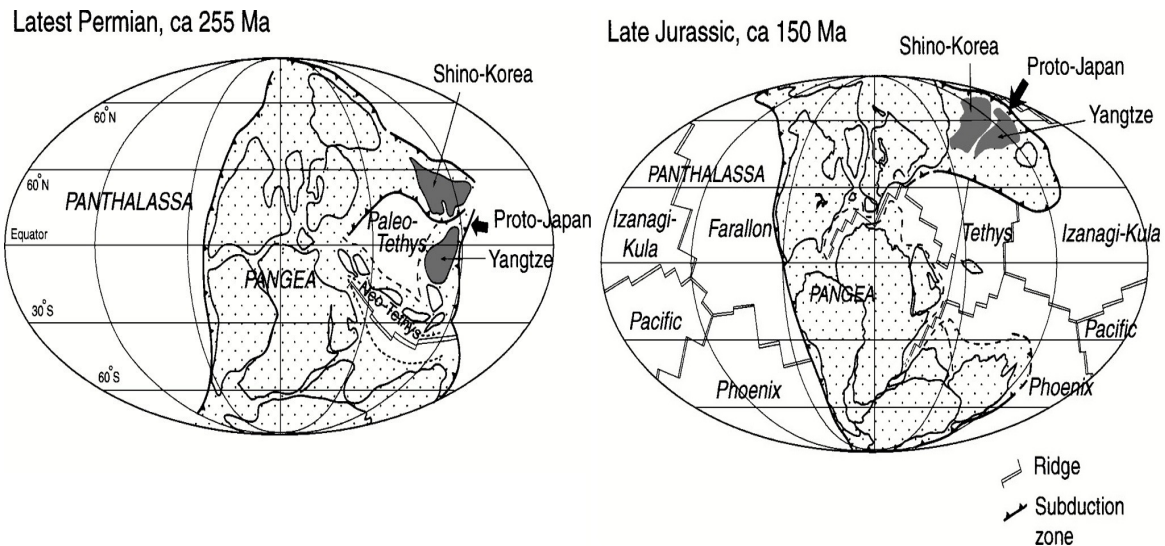


Figure 2.2: Schematic illustration showing the supercontinent Pangea and possible location of proto-Japan during the Late Permian and Late Jurassic period. Figure from Taira (2001).

The subduction of the ridge between two oceanic plates into the offshore trench created the basement rocks of Japan. Followed by a process of superheated magma and several high-pressure metamorphism, the igneous basement was formed. A collision of the Shino-Korea and Yangtze cratons in the beginning of Triassic resulted in the metamorphic belts of the current Japanese Islands. This event created other metamorphic belts as well situated in the current central and western Japan (Taira, 2001; Barnes, 2003).

The subduction resulted in the breakup of Pangea, which began approximately 200 Ma with extension of the Tethys Sea ridge. The breakup separated Pangea into the Laurasia and Gondwana supercontinents as mentioned earlier, which again exposed the pro-Japan area for ocean floor sediments and volcanic features during the Jurassic period (Barnes, 2003). The majority of the basement rocks was however formed during the Jurassic-Paleogene under the continuous process of subduction, high-pressure metamorphism and plate collisions. The Okhotsk Plate (a new plate) was formed on the northern edges of Laurasia during the Cretaceous. The plate occurred through relocation of the subduction trench towards the oceanward side of the new oceanic plate. During the Paleogene, the Okhotsk Plate collided with the Eurasian Plate (Fig. 2.3) (Taira, 2001).

A 160 km wide insular high at the shelf edge on northern Honshu Islands (The Oyashio landmass) supplied sediments land- and seawards in the beginning of Eocene. The landmass subsided between the end of Oligocene to Miocene with tuff volcanism near the present arc. The Japan sea opened during the Early Miocene allowing the landmass subside below sea level. This was associated with the tectonic erosion of the continental slope and landwards migration of the trench axis (Huene et al., 1994).

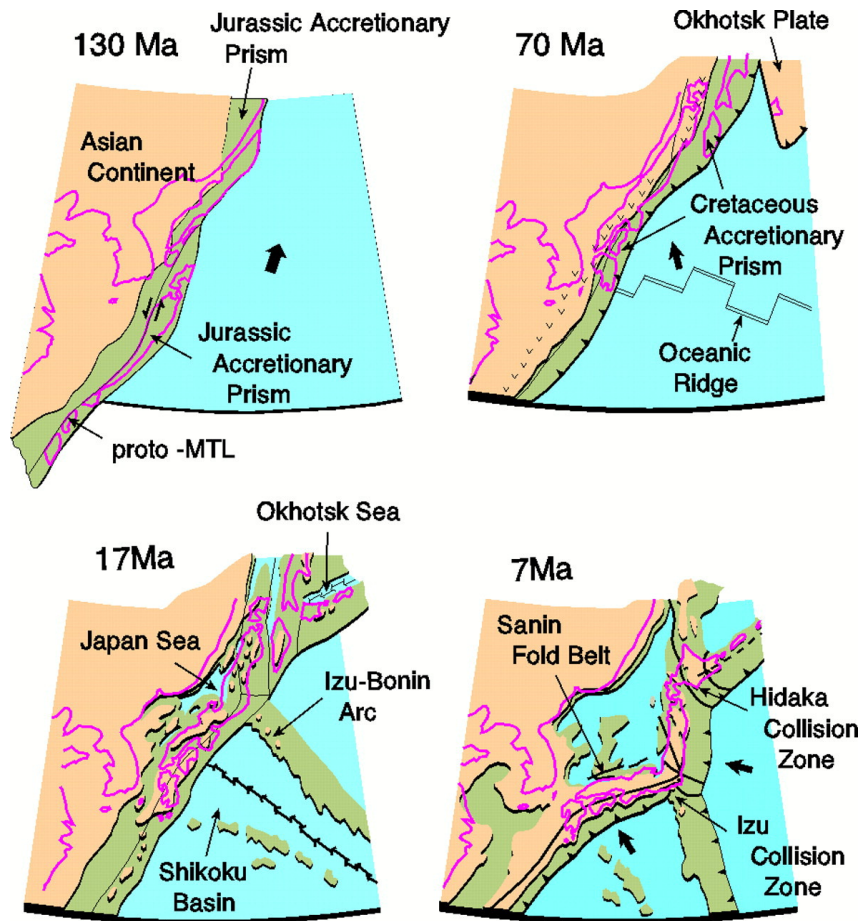


Figure 2.3: Schematic reconstruction from 130 Ma. Figure from Taira (2001).

The Shikoku Basin and Izu-Bonin arc were created during the seafloor opening, and the spreading pushed igneous belts that had developed on the continent's edge into two separate Island arcs (Japanese and Kurile). The spreading created many horst and graben structures as a result (Taira, 2001). A clockwise rotation of 45° took place on the southwestern portion of Japan, and the rotation moved 21 cm/year for 1.8 million years along the continental margin margin before coming to rest at present situation approximately 15 Ma (Barnes, 2003).

3 | Theory

3.1 Seismic Acquisition

Seismic surveys are in general acquired by commercial contractors and can be differentiated between land and marine acquisition of 2D and 3D surveys. With focus on marine seismic surveys, the contractors use surface-induced seismic pulses generated by air guns or other acoustic sources to acquire the subsurface data. A ship tows one or more energy sources parallel with one (2D survey) or more (3D surveys) receiver lines. The hydrophones (pressure sensors) on the receiver lines pick up the reflected pulses that bounce off the the subsurface layers. Propagation fundamentals will not be explained, but the first waves to arrive are the P-wave (Body waves). The hydrophones convert these signals into electrical energy that are digitized and transmitted to a recording system onboard the vessel. The data are typically stored as SEG-Y format and bandlimited where the useful information are approximately 5 - 20 Hz for deep reflections and 5 - 80 Hz for shallow reflections (Onajite, 2013). A reflected pulse illustrates changes in Acoustic Impedance (velocity multiplied with density), which often represents a boundary between different properties (beds/lithology). The reflection coefficient between the two boundaries is calculated using Eq. 3.1 (Li, 2013; Rigzone, 2017).

$$RC = \frac{Z_n - Z_{n-1}}{Z_n + Z_{n-1}} = \frac{V_n \rho_n - V_{n-1} \rho_{n-1}}{V_n \rho_n + V_{n-1} \rho_{n-1}} \quad (3.1)$$

An illustration of a 2D marine acquisition is displayed in Fig. 3.1 where a single source with a single streamer line consisting of a certain number of channels (Hydrophones) is towed by the vessel. The hydrophones are often spaced 12.5 or 25 m in length and the streamer length can be up to 5 - 6 km. The streamer tow depths can vary from 4 - 5 m for shallow, high resolution surveys in good weather conditions to 8 - 10 m for deeper surveys where low frequencies are targeted. (IAGC, 2002). This type of acquisition assumes that the 2D data recorded only represents horizontal and vertical data (Li, 2013). An actual acquisition of this type is very much controlled by the weather conditions, i.e. wind, temperature, and water current. The impact of water currents tend to cause an offset deviation from straight as displayed in Fig. 3.2. The deviation is often known as feathering where the angle α is created between the nominal cable location and actual location. However, the variation in vessel steering and currents cause the cable shape to depart and creates streamer curvatures. The deeper the tow depths of the streamers are, the less effected are the streamers by the weather noise (Gadallah and Fisher, 2005; Li, 2013).

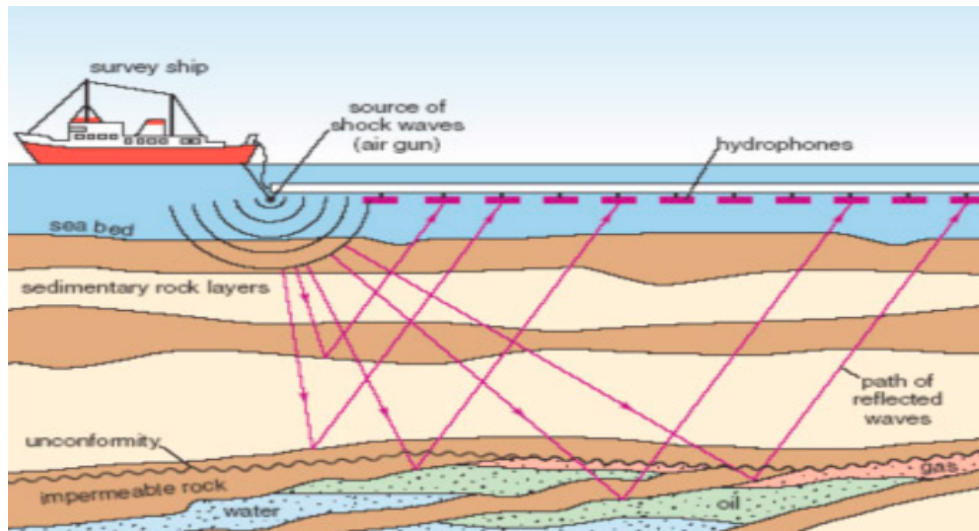


Figure 3.1: A schematic illustration of marine 2D seismic acquisition where a vessel tows one source parallel with one towed seismic receiver lines. Figure edited from Rigzone (2017).

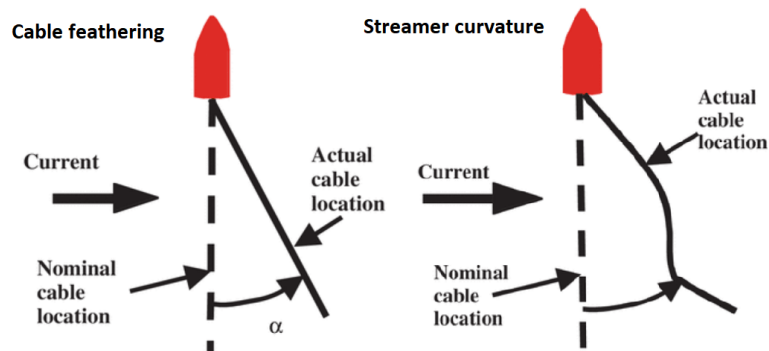


Figure 3.2: Illustration of cable feathering and streamer curvature. Figure edited from Gadallah and Fisher (2005).

3.1.1 Time-lapse seismic acquisition

A time-lapse acquisition is defined as a survey repeated over the same area and is often used to detect changes in the subsurface over time. The source and receiver positions should be kept at the same location during the acquisition, but are vulnerable to factors mentioned earlier which causes the misalignments (Yang, 2012). Common noise levels for streamers are approximately 2 - 3 μ bar in calm weather, and a scenario with a 6 km streamer length can create a cable offset displacement of 105 m with only 1° between nominal cable and actual cable position (Gadallah and Fisher, 2005). However, geophones (source gun) and hydrophones are equipped with GPS allowing their coordinates to be measured, and wings/fins were developed in the 1990s, which allowed the streamers to be steered into wanted positions in both x-y coordinates and depth. This would minimize the displacement errors for seismic acquisition and most certainly minimize errors related to time-lapse acquisition (Landrø, 2011).

3.1.2 Bubble signal

The air gun has an undesirable after-effects where it generates so-called bubble signals. The compressed air released by firing a shot into the water creates an air bubble that rapidly expands. The pressure inside the bubble becomes less than the surrounding water pressure, and the bubble contracts as a result. Another signal is hence created that expands when the air pressure is again higher than the water pressure. This particular contraction repeats itself until all energy is dissipated as illustrated in Fig. 3.3 (Gadallah and Fisher, 2005). The primary-bubble ratio (Eq. 3.2) is often used to describe this effect where the highest ratio is desirable, but strongly dependent on the frequency content. Methods for increasing this ratio are for example a combination of different gun chamber volumes, clustering air guns, and wave shaping kits (Landrø, 2011). The source signatures are also a concern for time-lapse acquisitions as they vary from one survey to another (Yang, 2012).

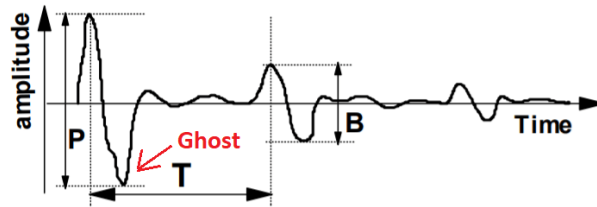


Figure 3.3: Typical source signature where Primary (P) and Bubble (B) signals are observed. The ghost reflection of the Primary signal is marked by the red arrow.

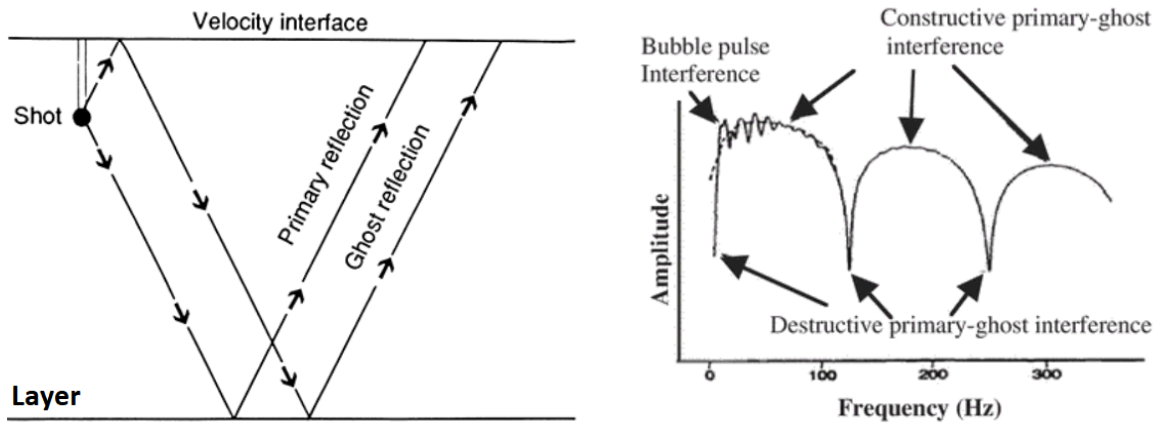
Figure edited from Landrø (2011).

$$\frac{\text{Total Amplitude } P}{\text{Total Amplitude } B} = \text{Primary} - \text{Bubble ratio} \quad (3.2)$$

3.1.3 Ghost reflector

A ghost reflector is a direct consequence of the air gun and streamer being towed below the water surface. The shot from the air gun bursts energy in all direction and the upward-travelling energy is reflected at the water-air interface as displayed in Fig. 3.4a, and explained by negative reflection coefficient (Eq. 3.1). It interferes with the downwards-travelling energy and appears as an event just below the primary reflector with negative/opposite amplitude (Fig. 3.3) (McGuire and Miller, 1989; Gadallah and Fisher, 2005). The frequency notch (low amplitude) of the source ghost spectrum can be calculated using Eq. 3.3 where c denotes water velocity and z_g the depth of the receiver. Deghosting filters can be used to attenuate the ghost while physical methods such as ocean bottom cable equipped with hydrophone sensors for measuring pressure and particle velocities are proposed to minimize the effect of the ghost (Landrø, 2011).

$$f_{notch} = \frac{c}{2z_g} \quad (3.3)$$



(a) Propagation of ghost reflection. (b) Frequency domain attribution from the air gun.

Figure 3.4: Illustration of ghost reflection and its frequency pattern. Figure from McGuire and Miller (1989) and Gadallah and Fisher (2005).

3.1.4 Wavelet shapes and phases

Seismic reflections can come in many phases and shapes. They are often differentiated between minimum and zero phase, and the source wavelet can be shifted and/or convolved with a desired wavelet during processing (Fig. 3.5). The polarity of marine seismic data is identified by observing the seabed reflector where it goes from low to high AI.

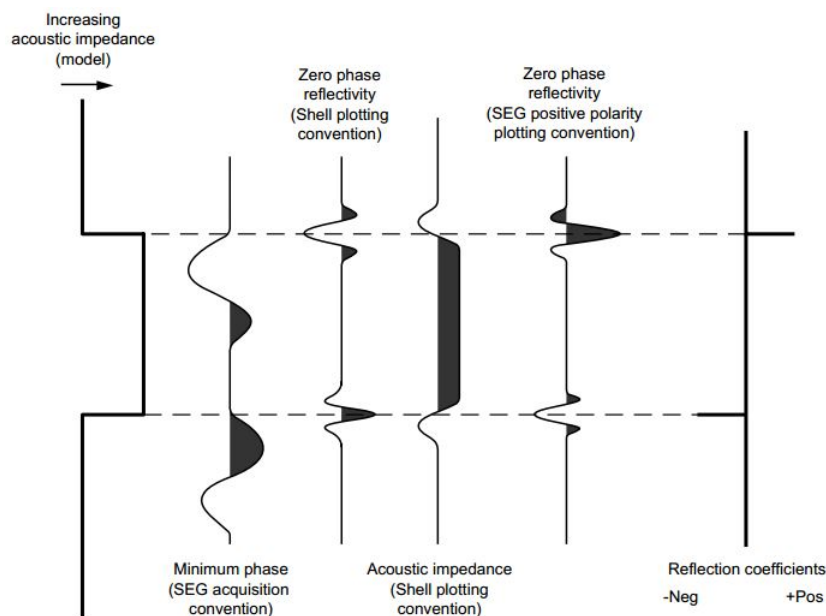


Figure 3.5: Typical wavelets used for scenarios of increasing and decreasing Acoustic Impedance (AI). Figure from Simm and White (2002).

3.2 Time-lapse Datum Correction

Certain elements are quite important for the time-lapse seismic to be comparable. A main part of the *pre-processing* steps are to perform a datum correction to align and correct the field geometry and statics of the surveys. The actual shot and receiver x-y-z coordinates collected from the navigation data are shifted to a predefined datum plane by removing the effect of elevation and variation (Fig. 3.6). To do this, one needs to know the velocity (P-wave and S-wave) between the free surface and datum level. Errors in geometry could potentially give errors in velocities, and these static errors can only be fixed by applying geometric corrections (Gadallah and Fisher, 2005; Landrø, 2011). Many algorithms can be used to fix this issue and only the selected method will be further described in Chapter 5.

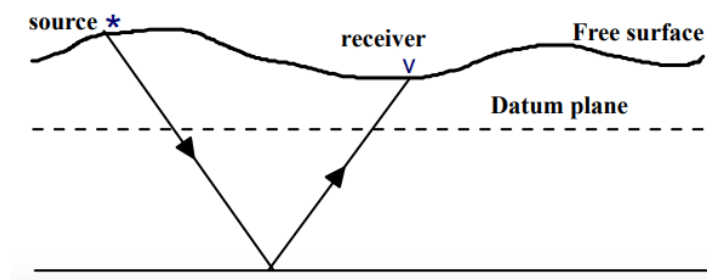


Figure 3.6: Illustration of field static correction. Figure from Landrø (2011).

3.3 Main Time-lapse Processing Steps

Seismic processing aims at improving the quality of acquired data through increasing signal-noise ratio and to image subsurface structures as detailed as possible. For a time-lapse survey, many processing steps needs to be similar in both type and parameters, i.e. mute design, debubble filter, velocity analysis, migration etc. The baseline survey is often used as a reference for the repeated survey to be processed through the similar processing sequences in the same order to minimize errors (Yang, 2012). A range of standard processing steps will therefore be briefly explained relative to the objectives of this thesis. One should be aware that there are many processing steps in different orders, and not necessarily in the specific order given below.

The common shot domain is often used to observe the data during the beginning of the processing steps. Typical events such as direct, reflection, refraction and multiple waves are observable as displayed in Fig. 3.7. The first arrival is the direct wave, which is followed by reflected waves at low offsets. The order of arrival on other offset changes as each wave have their own velocity (Onajite, 2013). The internal multiples occur especially when there are large reflection coefficient present (Gelius, 2007). The reflection's hyperbolic curvature can be expressed by the offset distance between source and receiver creating a delay in arrival time. This can be mathematically described by Eq. 3.1 where v_n is the velocity in layer n , t_0 is the two-way vertical travelttime defined in Eq. 3.2 where z is the depth of the reflected layer. The equation of travelttime thus become more complicated when considering dipping and multiple layers.

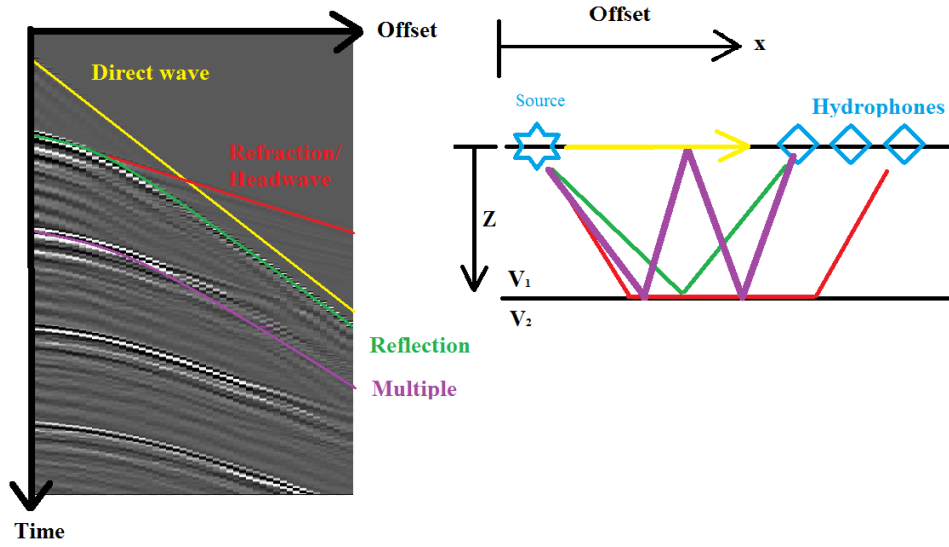


Figure 3.7: A typical shot recorded and displayed in shot domain. The offset is plotted against travelttime to observe the waves recorded. Figure edited from (Onajite, 2013).

$$t_x = \sqrt{t_0^2 + \frac{x^2}{v_n^2}} \quad (3.1)$$

$$t_0 = \frac{2z}{v_n} \quad (3.2)$$

3.3.1 Resampling

Resampling is a procedure done to reduce the seismic data to a certain sampling rate or higher to avoid aliasing, which is a distortion of frequency by insufficient sampling of the data. The procedure is done to reduce the noise of the data and also due to limited information greater than approximately 100 Hz (Onajite, 2013). Eq. 3.3 is used to calculate the frequency content of the seismic data at various sampling periods (T in milliseconds). The minimum requirements for the highest frequencies to be recovered from sampled data is calculated using Eq. 3.4. The data are often resampled from 2 to 4 ms, which corresponds to a change of f_N from 250 Hz to 125 Hz respectively, and is believed to improve the resolution (Hardy, 1999).

$$f = \frac{1}{T} \quad (3.3)$$

$$f_N = \frac{1}{2}f \quad (3.4)$$

3.3.2 Gain correction

Amplitude recover is a procedure used to gain amplitudes of the seismic traces. This method is used as a compensation for the time dependent loss due geometric spreading, transmission loss, and absorption effects. Geometric spreading is an effect where the amplitude decays proportional to the distance r of the source ($1/r$) and the wave energy ($1/r^2$). Transmission and absorption effects results in attenuated signal strength as well. A simple gain correction can be defined by Eq. 3.5 where $g(t)$ is an exponential function. An example of an amplitude recovery of one trace is displayed in Fig. 3.8. Amplifying the traces would also cause an amplification of noises as well (Landrø, 2011).

$$A_{out}(t) = g(t) \cdot A_{in}(t) \quad (3.5)$$

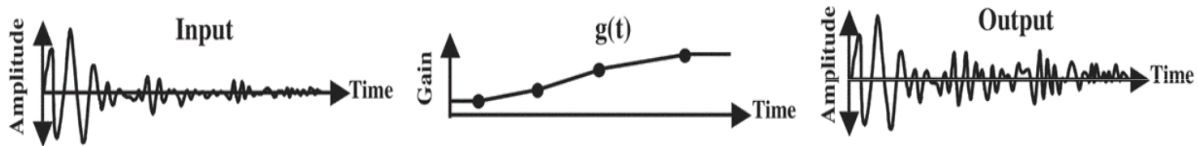


Figure 3.8: Example of Gain correction. Figure edited from (Onajite, 2013).

3.3.3 Shot to CMP

There are typically four types of gather, i.e. common shot, midpoint, receiver, and offset gather, which the data can be sorted into (Fig. 3.9). The initial display mentioned earlier is in group of traces sorted as common shot gathers (Fig. 3.7). The data are often converted to gathers such as Common Mid-Point gather to overcome the noise problem and additionally to estimate the earth velocity in different layers. The traces are sorted with their source-receiver midpoint falling on the same point. When considering a horizontal spacing x , the CMP spacing will hence be $x/2$. A CMP gather contains $n/2$ receivers where n is the number of receivers. A CMP fold is defined as the total number of traces, which can be calculated using Eq. 3.6 where n is the number of receivers, Δx the CMP spacing, and Δl the shot spacing (Hardy, 1999).

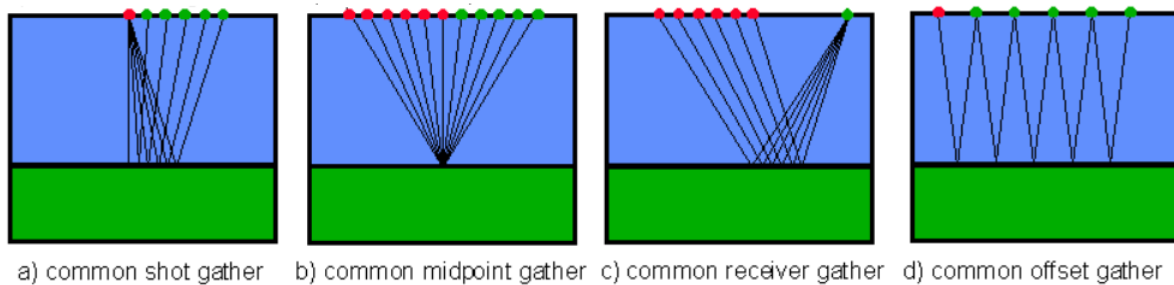


Figure 3.9: Schematic illustration of gathers. Figure edited from (Hardy, 1999).

$$fold = \frac{n\Delta x}{\Delta l} \quad (3.6)$$

3.3.4 Mute

Unwanted parts of the data such as refraction and direct wave is removed by applying a mute. Top mute is a term used for removing top parts of the data and the procedure can be done in any gather domains. The muting procedure can also be performed on bottom parts of the data as well. An illustration of a top mute is displayed in Fig. 3.10 where the direct wave, refraction, and some noises are removed by applying a muting algorithm that mutes everything above the line and keeps the data below (Hardy, 1999).

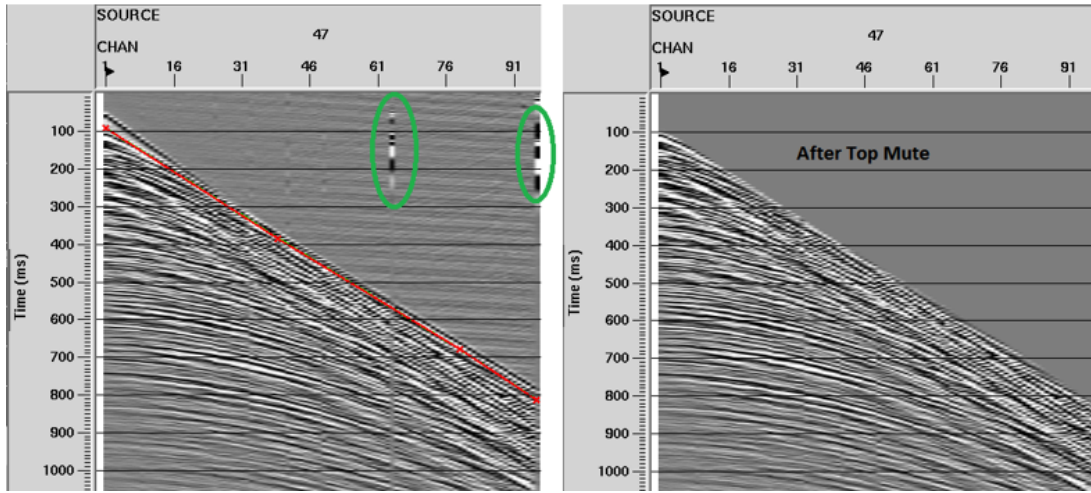


Figure 3.10: Before and after Top mute of a shot gather. The green ellipses illustrates areas of noise, while the red line shows the selected “Top Mute”.

3.3.5 Velocity analysis, NMO correction and stacking

Velocity analysis is performed to obtain velocities that flattens the reflection hyperbola on a CMP gather. The semblance function (Eq. 3.7) is commonly used as a velocity spectrum for picking the velocities suited for stacking. The term $f_{i,t(i)}$ in Eq. 3.7 represents the seismic amplitude of the i – th trace within a CMP gather of total M traces for the two-way travel time t_i . This traveltim is connected to the stacking velocity v_{st} in the travel time function in Eq. 3.8 (Landrø, 2011).

$$SE(t) = \frac{\sum_t \left[\sum_{i=1}^M f_{i,t(i)} \right]^2}{\sum_t \sum_{i=1}^M f_{i,t(i)}^2} \quad (3.7)$$

$$t_i = \sqrt{t_0^2 + \frac{x_i^2}{v_{st}^2}} \quad (3.8)$$

The Normal Moveout (NMO) curvature (previously expressed as hyperbolic curvature) undergoes a correction where the reflections line up on the gather after applying the picked stacking velocity (Fig. 3.11). If the picked velocity is too low, the NMO curve will be overcorrected and vice versa. The typical trend of flattening reflections is a velocity increase with depths where velocities lower than 1430 m/s and higher than 6700 m/s are very unlikely to occur. Stacking sums the traces and should increase the signal-noise ratio, resolution, and attenuate multiple reflection due to reducing multiple-amplitudes after stacking if the correct velocities are picked (Hardy, 1999; Landrø, 2011).

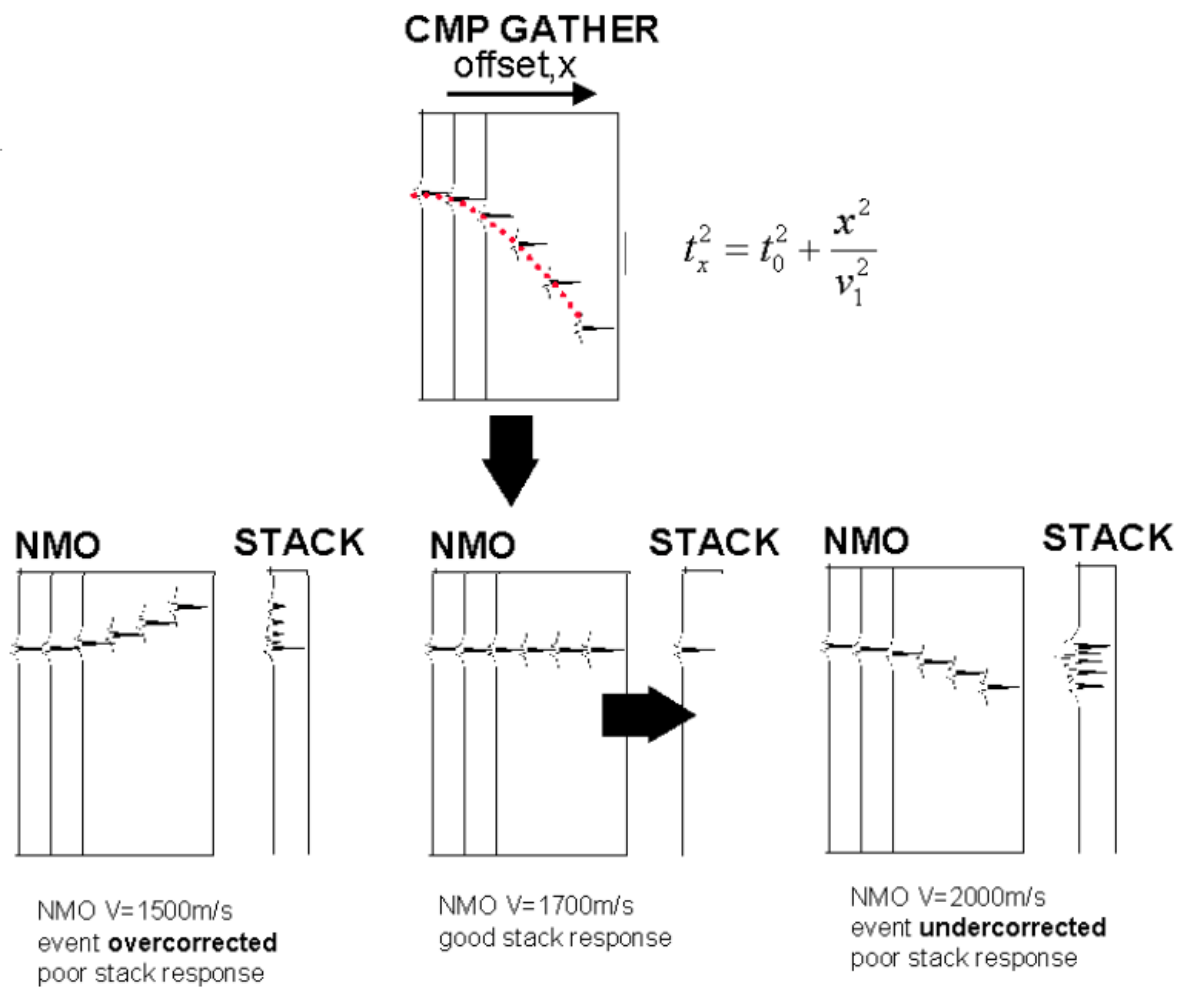


Figure 3.11: Schematic illustration of NMO correction and stacking of one reflection.
Figure edited from (Hardy, 1999).

3.3.6 Filtering of seismic data

Seismic data can be shaped through various filters such as *Frequency filter*, *deconvolution*, and multiple attenuation filters such *f-k* and *radon* filters. These methods are described below and could be applied to the data prior to a velocity analysis for a possible better result.

- **Frequency filtering**

Wind and instrumental noises are generated at high frequencies outside the seismic band, while ground roll and vessel (propeller and possible tail buoy) generate noises at low frequencies. A method used to removed these frequencies is to apply a frequency filter such as low-pass, high-pass, band-pass or notch filters (Fig. 3.12). The filters can also be categorized under types with their effect on the amplitudes in the frequency domain. Here, filters can be such as Ormsby (linear slope) and Butterworth (curved slope). The filters schematically illustrated in Fig. 3.12 uses an Ormsby approach (Hardy, 1999).

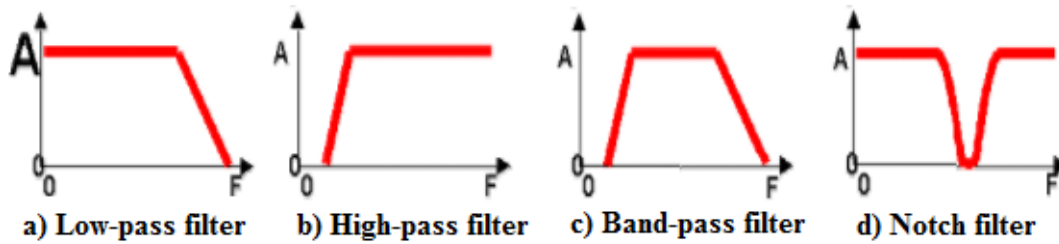


Figure 3.12: Schematic illustration of Ormsby filter types. Figure edited from (Hardy, 1999).

- **Deconvolution**

Ghost reflectors, bubble signals, and multiples could be removed using a deconvolution, which is a reverse process of convolution. The seismic signal can be expressed as a convolution between a wavelet $w(t)$ and impulse response of the the earth $f(t)$ as shown in Eq. 3.9. The deconvolution (inverse filter) $w^{-1}(t)$ of the wavelet is then defined by Eq. 3.10, which is used to remove all unwanted effects and increase the vertical resolution (Gelius, 2007; Landrø, 2011).

$$y(t) = w(t) * f(t) \quad (3.9)$$

$$w(t) * w^{-1}(t) = \delta(t) \quad (3.10)$$

A way to remove the effect of debubble signal can be done using the Wiener filter, which transforms a wavelet into a more compact form. The filter uses a desired wavelet to derive the optimal filter that converts the input data to the desired output data, for example shaping the source wavelet from air guns to a desired wavelet. Methods such as *Predictive deconvolution* can be used to compress long pulses with aims to replace it with primary only, and with aims to weaken and remove multiples (Gelius, 2007).

- **F-K and Radon filter**

The data can be illustrated in the Frequency-wavenumber (F-K) domain by applying a Fourier transform (Fig. 3.13). The dimension is controlled by trace spacing and must be sampled according to the Nyquist criteria similar to resampling in time. The various type types can possibly be more visually separated in F-K domain. A mute can hence be applied in this domain before applying a reverse transformation to time domain (Hardy, 1999). Landrø (2011) proposes a theory where the primaries can be separated from the multiples by applying a NMO correction where primaries are overcorrected (Fig. 3.13).

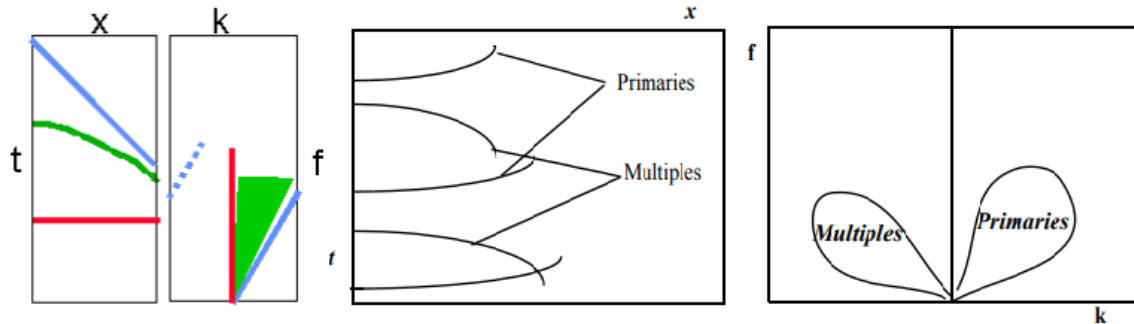


Figure 3.13: Left figure shows the F-K domain of a CMP gather. Middle and right figures illustrate the primary and multiple reflection in F-K domain with NMO correction where primaries are overcorrected. Figure edited from Hardy (1999) and Landrø (2011).

Another transformation, Radon transform, can be used to transform the data into the Radon domain. The curvatures (reflection, refraction, multiples etc.) are mapped to a point in this domain. In domains of hyperbolic and parabolic Radon transforms, one can use CMP gathers and their NMO corrected gathers to detect and remove multiples in similar matter with muting. A special case of Radon transform is also the Tau-P filter, which will not be described (Hardy, 1999).

3.3.7 Migration

The gathers described earlier are illustrated for horizontal layer assumptions and where the reflection point lies at midpoint (CMP). In reality of dipping layer, the reflection point will be shifted either up-dip or down-dip as illustrated in Fig. 3.14a. Applying a migration algorithm will move the apparent position, which has an apparent angle, to its actual position as illustrated in Fig. 3.14b (Gadallah and Fisher, 2005; Schulte, 2012; Onajite, 2013). Other effects such as bow-ties (synclinal structures) and diffractions are collapsed and focused by performing a migration (Fig. 3.15). Anticlines are a typical structural shape which appear wider than they actually are, and are shorten by the migration.

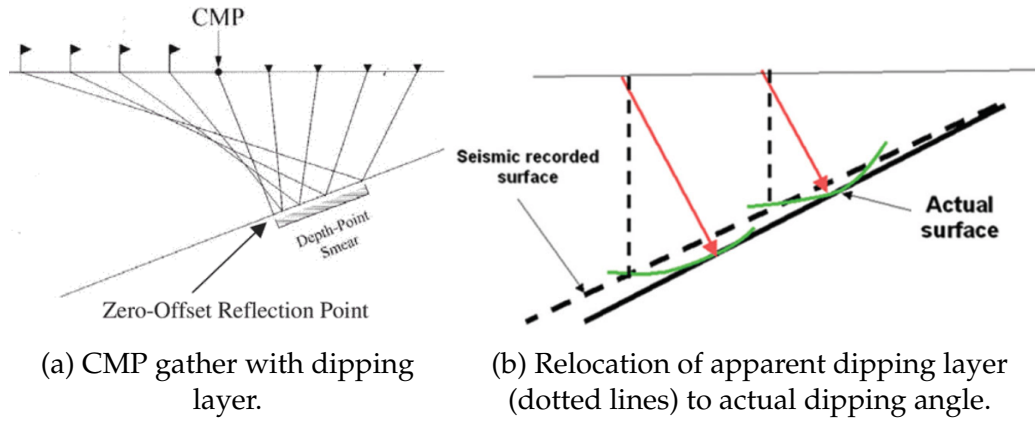


Figure 3.14: Illustration of the effect of migration on dipping layer reflection. Figure edited from Gadallah and Fisher (2005) and Schulte (2012).

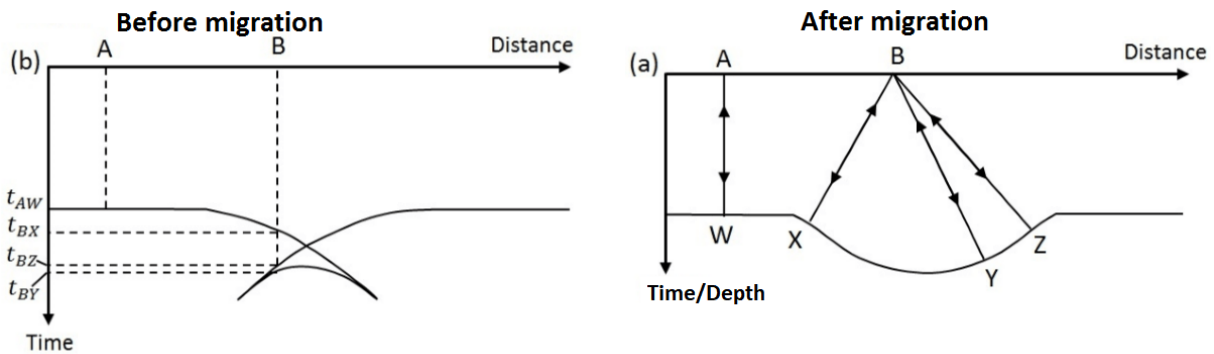


Figure 3.15: Illustration of an anticline before and after migration. Migration collapses the bow-ties to reveal the true image of the layer.

Migration can be described as an art of reversing wave propagation effects in order to obtain a clear image of the subsurface. It is often differentiated into the four following types (Landrø, 2011):

- Post-stack time migration
- Post-stack depth migration
- Pre-stack time migration
- Pre-stack depth migration

Pre- and Post-stack migrations depend on economical factors as they both are time- and cost consuming steps. Pre-stack is usually a more expensive method to migrate the data prior to stacking. Some structures are impossible or difficult to stack prior to migration and where pre-stack migrations would benefit. This method is also proposed to improve resolution within areas of high complex (Schulte, 2012).

A velocity model is required as input in a migration algorithms, and the quality of the migration is highly dependent on the velocity model to produce the final migrated image. The velocities are often obtained from the stacking velocities. Choices of

algorithms can be differentiated between time and depth migration, and is contractor dependant. Time migrated images are displayed in two-way travelttime (TWT) whereas the depth migrated images are displayed in true vertical depth (TVD). Time migration ignores ray bending at velocity boundaries and assume the diffraction shapes as hyperbolic (Hardy, 1999). Depth migration are migrated in the depth domain by using interval velocities in depth. The stacking velocities are assumed to be approximately root mean square velocities V_{RMS} and converted to interval velocities using Dix equation (Eq. 3.11) where n denotes the layer (Schulte, 2012).

$$V_{int,n} = \left[\frac{t_n V_{rms,n}^2 - t_{n-1} V_{rms,n-1}^2}{t_n - t_{n-1}} \right]^{\frac{1}{2}} \quad (3.11)$$

A detailed velocity model might be needed as the depth migration is highly sensitive to the velocities. Incorrect models would produce inaccurate depths of the layers. The depth migration can handle both vertical and lateral variation in velocities, and requires more computational power and time than time migration. This will in return have higher cost for the processing partners (Onajite, 2013).

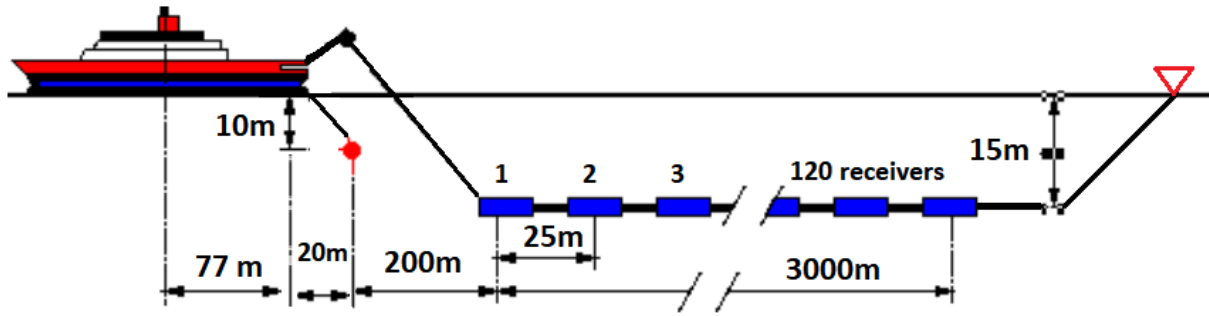
Methods such as Kirchhoff, Finite-Difference and Fourier transformation are optional methods for time migration where Kirchhoff migration is a utilized good option for pre-stack time migration. It can handle irregular acquisition geometry and is flexible for production subsets of output image volumes (common offset volumes) for Amplitude versus Offset analysis. Depth migrations can be performed using Finite-Difference, Ray-theoretical, Image-ray tracing (could also be called Kirchhoff) or methods such as acoustic wave migration. Kirchhoff Pre-stack depth migration (Raypath) is also a good option for handling steep dips, turning rays, anisotropy and more (Landrø, 2011; Onajite, 2013). These migration methods will not be explained any further in details, but the selected methods will be described in Chapter 5.

4 | Data

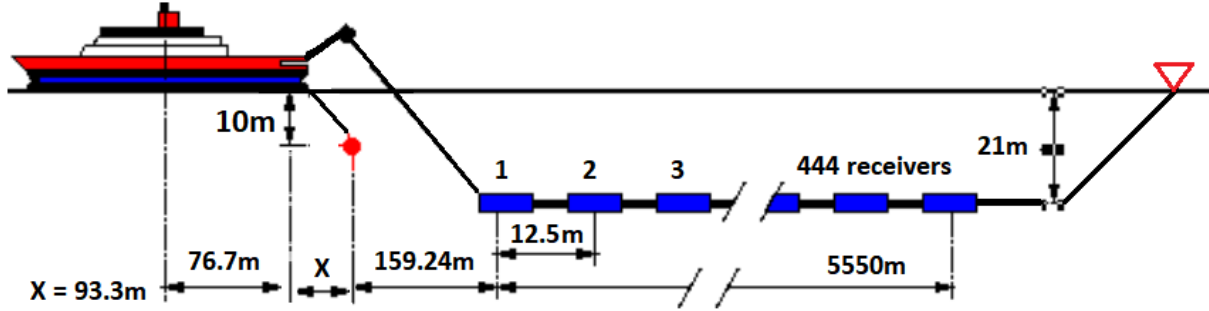
4.1 Acquisition parameters

The seismic surveys SR97-101 and D19 were acquired by the JAMSTEC vessel *R/V Kairei* in 1997 and 2011, respectively. Survey SR97-101, hereby termed as the baseline survey, was acquired using four air guns with 100 cu. in. (≈ 16.4 L) in volume each. The cable streamer consisted of 120 receivers with receiver interval of 25 m, which gives a total cable length of 3000 m. The air guns (source) was placed at 10 m depth while the streamer cable was placed at 15 m depth. The distance between the source and the receivers was 200 m (minimum offset), which gives a maximum offset of 3200 m. A number of 5494 shots were performed with 50 m shot interval and where a total of 659 280 traces were recorded. The data was sampled with 4 ms sampling interval and with a total recorded length of 13.5 s (TWT). The total length of the baseline survey is approximately 280 km.

The seismic survey D19, hereby termed as the monitor survey, was acquired using four air guns with 1950 cu. in. (≈ 32.0 L) each. Here, the cable streamer consisted of 444 receivers with 12.5 m interval, which gives a total cable length of 5550 m. The air guns was also towed at same water depths as the baseline survey while the streamer cable was placed at 21 m depth. The minimum offset of the monitor survey was 159.24 m and the maximum offset 5709.24 m. The total shots for the monitor survey was 4201 with same shot interval as the baseline survey. This gives a total number of 1 865 244 traces recorded in the monitor survey. The monitor survey was sampled with sampling interval of 2 ms and a total recorded length of 18 s (TWT). The total length of the monitor survey is approximately 210 km. The schematic acquisition parameters of the baseline and monitor survey are visualized in Fig. 4.1 and their parameters listed in Table 4.1.



(a) Acquisition parameters for the baseline survey SR97-101.



(b) Acquisition parameter for the monitor survey D19.

Figure 4.1: Schematic model of seismic acquisition parameters for the baseline (SR97-101) and monitor (D19) surveys. The red dot illustrates the source (air gun) and the red triangle is the Buoy tail attached at the end of the streamer cable. Edited from Hardy (1999).

Table 4.1: Acquisition parameters for the baseline and monitor surveys.

Parameters	Baseline survey	Monitor survey
Nr. of air guns	4	4
Air gun volume	1000 cu. in. ($\approx 16.4L$)	1950 cu. in. ($\approx 30.0L$)
Depth of air guns	10 m	10 m
Nr. of receivers	120	444
Receiver interval	25 m	12.5 m
Depth of receivers	15 m	21m
Total cable length	3000 m	5550 m
Minimum offset	200 m	159.24 m
Maximum offset	3200 m	5709.24 m
Nr. of shots	5494	4201
Nr. of traces	659 280	1 865 244
Total recorded length	13.5 s	18s
Sampling interval	4 ms	2 ms
Total seismic length	≈ 280 km	≈ 210 km

4.2 Problems with the data

There are significant errors in the baseline navigation file, which makes the first and last GPS shot point not comparable with the monitor survey. The monitor survey was also acquired with more data towards the east and less data towards the west compared to what the baseline survey covers. These situations have hence created difficulties when considering time-lapse interpretation as it requires input of the navigation coordinates (either first or last coordinates) to be matched. To overcome this problem, a manually navigational shift of the baseline survey will be performed from an arbitrary nominal line from origin. This will highly result in both horizontal and vertical displacement errors when consideration the tectonic displacement related to the earthquake. The results from the *time-lapse* seismic interpretation should therefore be treated with caution as it contains displacement errors caused by incorrect shift of navigation. Visual seismic observations will therefore be emphasized on when comparing the surveys.

Imaging subsurface structures across the Japan Trench is extremely difficult and requires a dedicated large-offset acquisition. As the baseline acquisition was performed with maximum offset being 3.2 km and monitor acquisition with 5.55 km, there will be limited features at deep depths. The data quality is considered to be poor at certain depths due to the limited seismic energy reaching the receivers. Another issue related to the surveys is the repeatability problems, which needs to be taken into account throughout all steps and will be discussed in Chapter 7 (Kristensen, 2017).

5 | Methods

5.1 Madagascar processing software

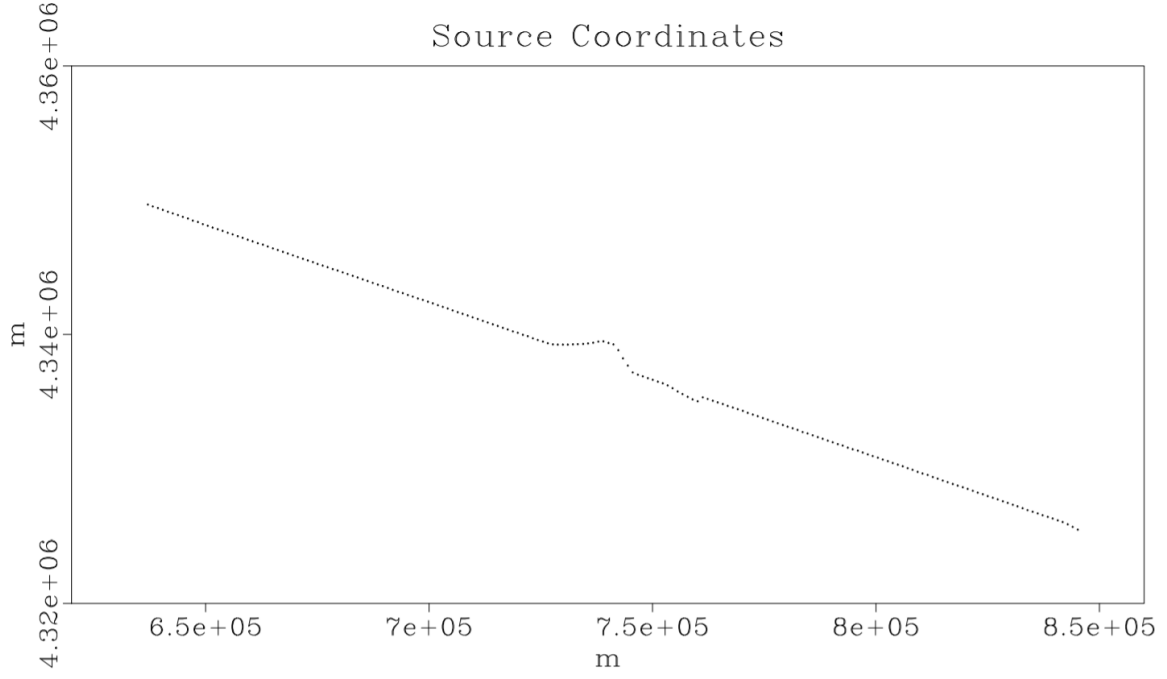
Madagascar is one of the most extensive open-source packages for processing seismic data on various platforms such as Linux, Solaris, MacOS, and Windows (under Cygwin environment) (Oren and Nowack, 2018). It is made up of several software packages designed to perform specific tasks. The file formats are in Regularly Sampled Format (RSF), which is simpler for managing SEG-Y formats. The main scripts *Bash* and *SConstruct* are used to create computational experiments and flows, and are written in Python based syntax. The software operates on UNIX commands and executes a command by calling a program and choose files to be read from and to (Steinsbø, 2013; Madagascar Development Team, 2018). All scripts used in this thesis can be found in the Appendix A. Their mathematical algorithms and parameters will hence be further described in this chapter.

5.2 Data Regulation and geometry correction

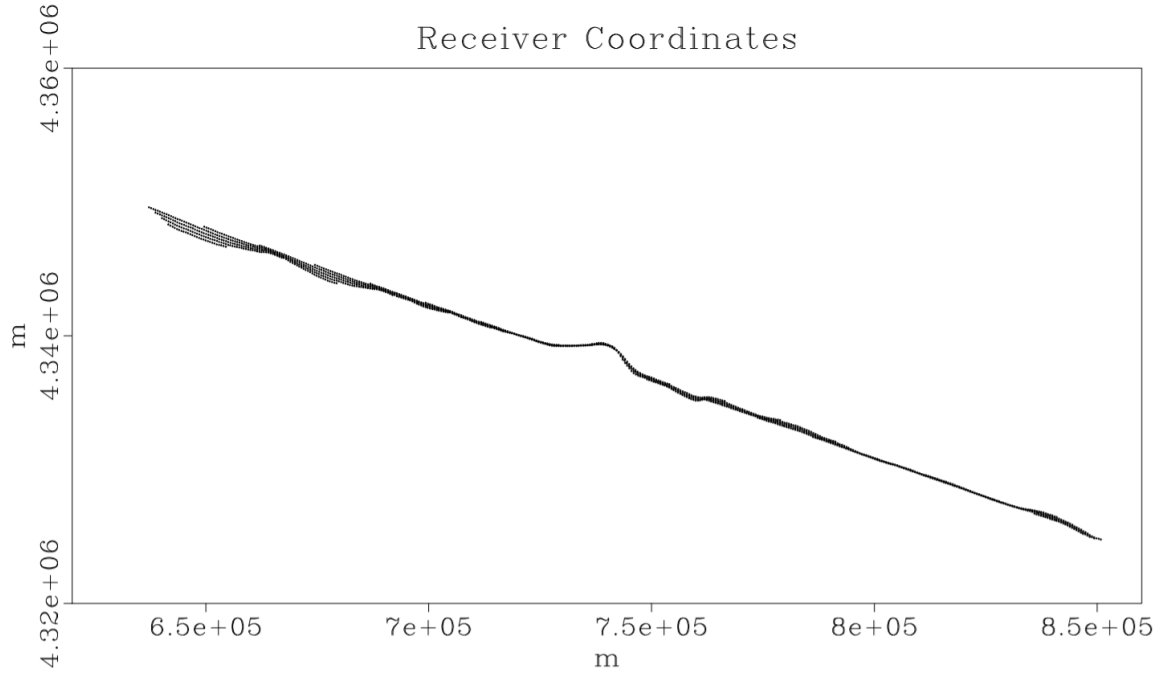
The baseline and monitor acquisition files were 11GB and 64GB, respectively, and were stored as the typical SEG-Y format. The first step of the processing was to convert these files from SEG-Y to RSF format using *Sfsegypread*. The program allows us to separate the raw data from the header file containing information from the acquisition. Due to the problems described in Chapter 4.2, only header information from the monitor survey will be further used and described in this section.

The GPS coordinates from the monitor survey header file are extracted and displayed in Fig. 5.1 for both source and receiver positions. Fig. 5.1 does not represent all shot and receiver coordinates, but only selected intervals of the total traces. The header file was scaled, shifted and rotated using *Sfheaderrot*. The main parameters used with this program are shown in Table 5.1 and the output displayed in Fig. 5.2.

A RSF header file was created using *sfmakehdr3d* with the parameters from Table 4.1, and with origin at (0,0) where the source and receiver positions were placed along the positive x-axis. This is displayed in Fig. 5.2 as a red polygon. The aim was to transfer the information from these original trace coordinates onto the pre-datum plan (header file) created. This was done by performing an interpolation between the points using a modified version of the algorithm called Shepard's method and differential NMO, which will be described next.



(a) Source coordinates displayed with selected coordinates for every 10 000 trace.

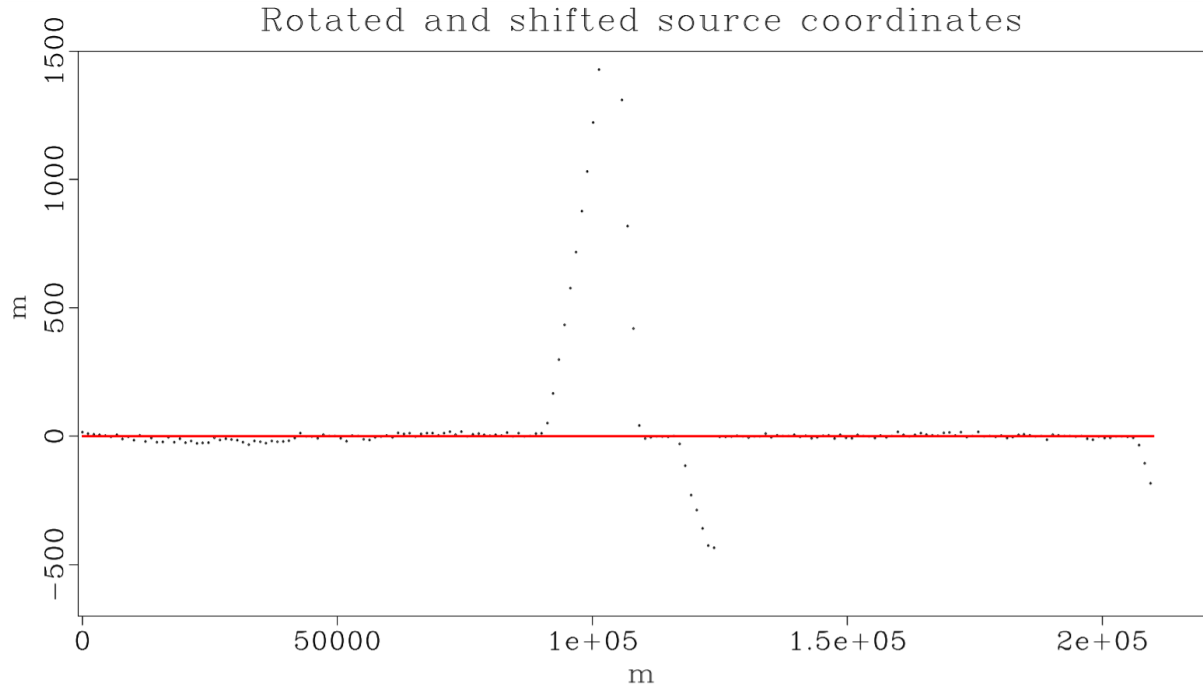


(b) Receiver coordinates displayed with selected coordinates for every 1000 trace.

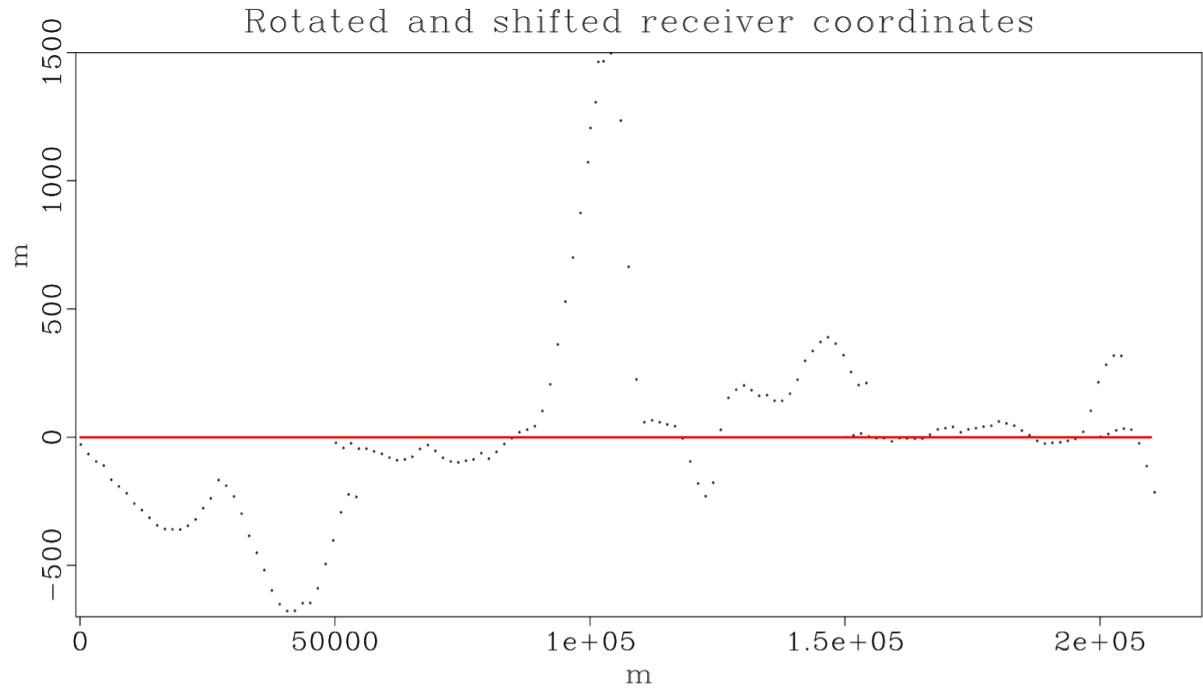
Figure 5.1: Source and Receiver coordinates for the monitor survey D19 with selected intervals for each trace-coordinate.

Table 5.1: Shift and rotation parameters

Parameters	Values
X-shift	4157971
Y-shift	39362650
Counterclockwise rotation, Θ	6.585



(a) Source coordinates displayed with selected coordinates for every 10 000 trace.



(b) Receiver coordinates displayed with selected coordinates for every 12 000 trace.

Figure 5.2: Source and Receiver coordinates for the monitor survey D19 with selected intervals for each trace-coordinate after applying the parameters in Table 5.1. The red polygon illustrates the pre-defined datum plane used for the interpolation with parameters from Table 4.1.

5.2.1 Modified Shepard's method and differential NMO

The Shepard's method, also known as the inverse distance weighted interpolation, is one of the most commonly used techniques to interpolating scatter points in an area. It uses the assumptions that each interpolated value is influenced by the neighbouring points and less influenced by the distant points. This can be mathematically described by a simplified version shown in Eq. 5.1 where n denotes the number of scatter points, f the function value at each scatter point which is the data set value and w_i a weight function assigned to each scatter point. The weight function is defined in Eq. 5.2 where h_i is the Euclidean distance (Eq. 5.3) from interpolation point to scatter point i and R is the distance from interpolation point to the furthest scatter point (Amidror, 2002).

$$F(x, y) = \sum_{i=1}^n w_i(x, y) f(x_i, y_i) \quad (5.1)$$

$$w_i = \frac{\left[\frac{R-h_i}{Rh_i} \right]^2}{\sum_{j=1}^n \left[\frac{R-h_j}{Rh_j} \right]^2} \quad (5.2)$$

$$h_i = \sqrt{(x - x_i)^2 + (y - y_i)^2} \quad (5.3)$$

The specific program used for the interpolation, *sfdatareg3d*, was modified by Weibull (2017) where he defined the correction for traveltime to datum plane as an offset function using the differential NMO and a constant water velocity of 1500 m/s ($v_{NMO} = 1500$ m/s). The program requires the value of interpolation radius R , which was set to be the 2000 m and represents the maximum deviation distance to interpolate. The program also transformed the data from a 2D geometry to a 3D geometry with shots, receiver and time axis, which then was sampled from 2 ms to 4 ms using *sfwindow* with sampling parameter $d1=0.004$ (Table 5.2).

Table 5.2: 3D geometry for the survey files in Madagascar.

(a) Baseline survey.

Window size	Sampling dimension	axis origin	Label and unit
n1 = 3375	d1 = 0.004	o1 = 0	Time (s)
n2 = 120	d2 = 25	o2 = 200	Offset (m)
n3 = 5494	d3 = 50	o3 = 0	Shots (m)

(b) Monitor survey.

Window size	Sampling dimension	axis origin	Label and unit
n1 = 4501	d1 = 0.004	o1 = 0	Time (s)
n2 = 444	d2 = 12.5	o2 = 159.24	Offset (m)
n3 = 4201	d3 = 50	o3 = 0	Shots (m)

5.3 Frequency filter and despiking

The data were transformed into the frequency domain using *sfspectra* to observe the frequency spectrum (Fig. 5.3). The source and receiver frequency notches were calculated using Eq. 3.3 (Table 5.3). The receiver frequency notch was then used as a guideline for creating a band-pass filter using *sfbandpass* with a low-cut of 3 Hz (*flo*=3) and a high-cut of 50 Hz (*fhi*=50). The band-pass algorithm uses a Butterworth approach where the number of poles *np* controls the slope of the filter and set to be 8. The frequency spectra after applying the band-pass filter are displayed in Fig. 5.4.

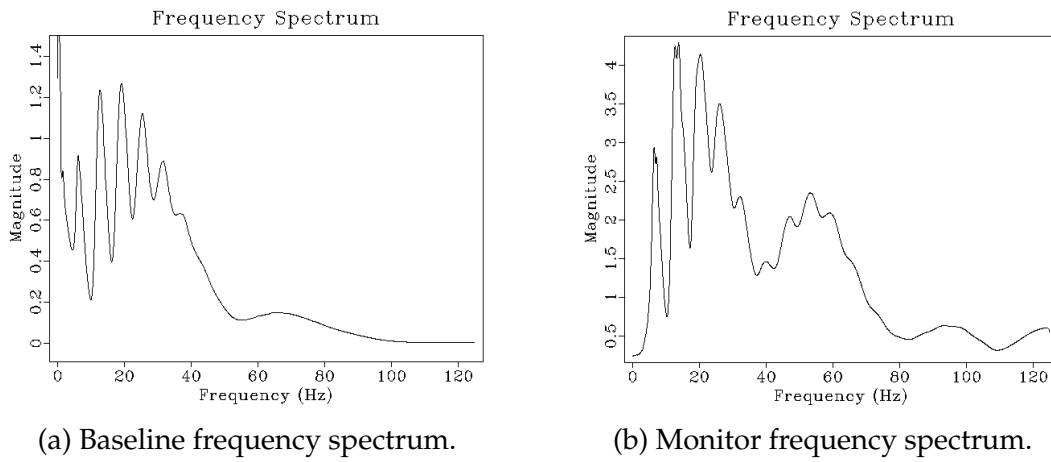


Figure 5.3: Frequency spectrum of the raw baseline and monitor surveys.

Table 5.3: Frequency notch calculated for source and receiver depths using Eq. 3.3.

Survey	Source depth	Source notch	Receiver depth	Receiver notch
Baseline survey	10 m	75 Hz	15 m	50 Hz
Monitor survey	10 m	75 Hz	21 m	35.71 Hz

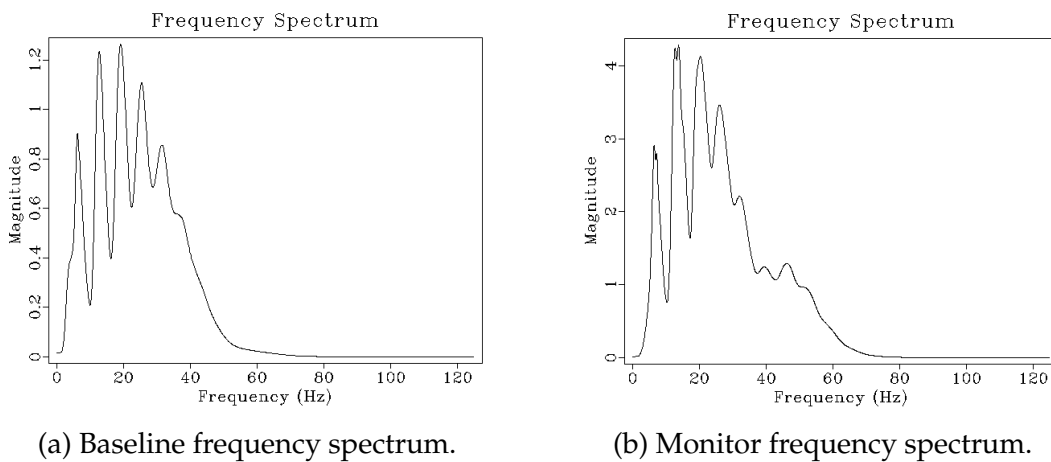


Figure 5.4: Frequency spectrum of the baseline and monitor survey after applying a band-pass filter with low-cut of 3 Hz and high-cut of 50Hz.

The program *sfdespike2* was used to minimize any abnormal spikes in the data after the band-pass filtering. The despiking is performed by sliding 2-D medias over the data and is controlled by the sliding window width with *wide1* and/or *wide2*. Only *wide2* was used and set to be 3 for both surveys.

A recorded trace was extracted from the data sets to illustrate the effect of the band-pass filter at small offsets (Fig. 5.5). The effect of despiking is hence not illustrated as it does not contain any significant differences for this particular trace. The extracted traces were also used as a guideline for creating the debubbling filter explained in the upcoming subsection.

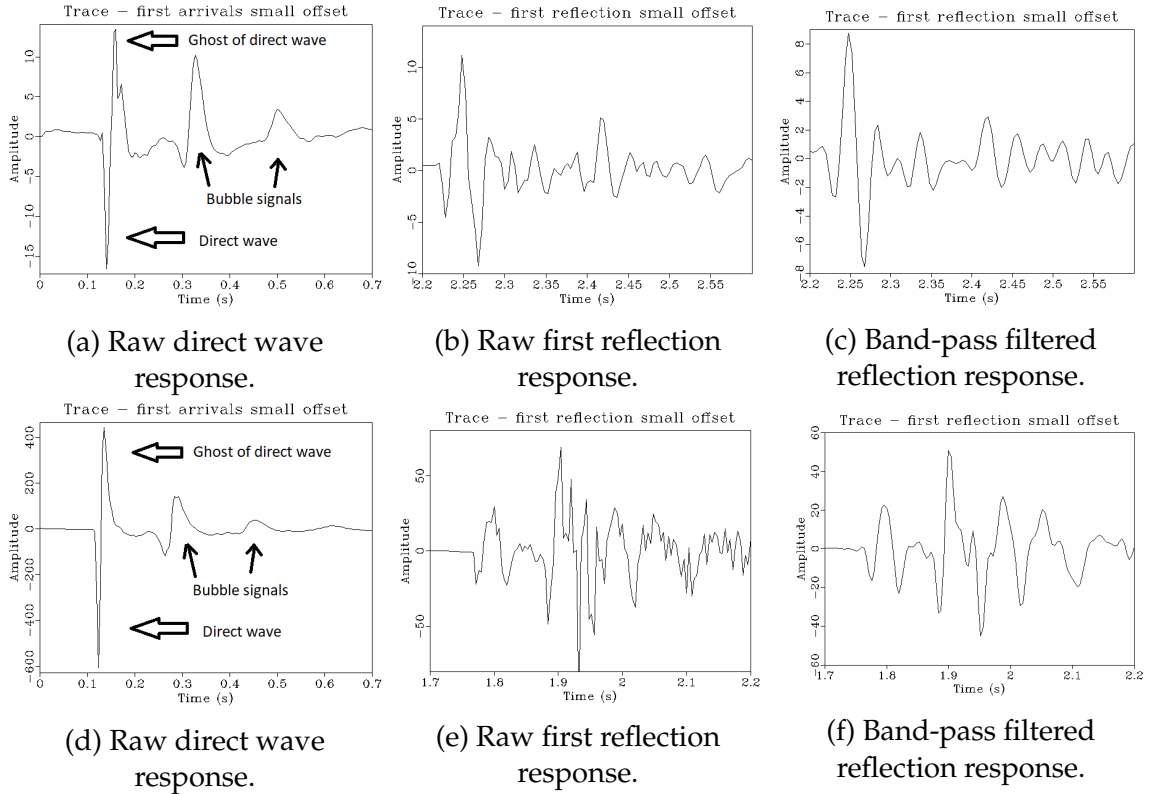
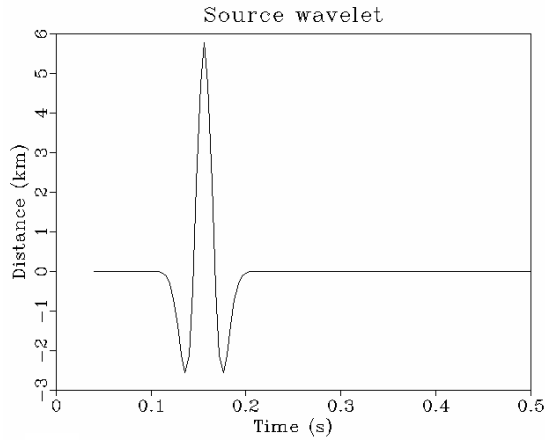


Figure 5.5: Trace display of the direct wave and first reflection response at small offset from the baseline (a-c) and monitor surveys (d-f).

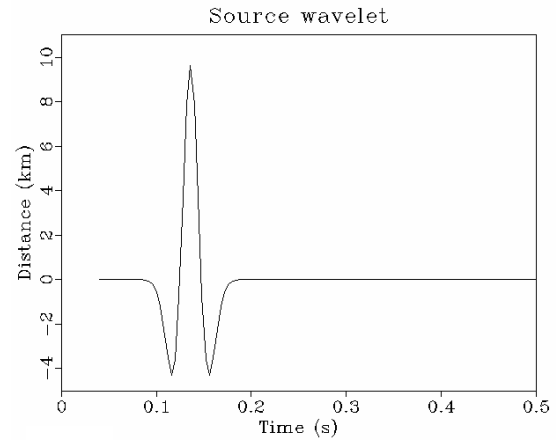
5.4 Debubbling filter

The air guns used in both surveys were not tuned prior to the acquisition, which gave a wavelet with no defined source signature. The bubble oscillation appeared approximately 200 ms after the direct wave displayed in Fig. 5.5a and approximately 190 ms in Fig. 5.5d. The bubble reflector was attempted to be removed by applying a shaping filter to the data using *sfshape*. The wavelets used for the filters were created by convolving a spike (source pulse) containing a desired amplitude with a ricker wavelet containing a dominant frequency. The shaping algorithm uses the wavelet as a desired input wavelet to shape the data. The output of this algorithm was then convolved with the data using *sfshape2*.

The source wavelets were created with emphasize on the shape of the first reflection, but using the travel time for the direct wave at small offset (Fig. 5.6). Their dominant frequency (peak frequency) were selected to be 20 Hz. The shaping filter *sfshape* is also controlled by the parameters *pnoise* and *nshape*, which are the relative additive noise and length of filter in number samples, respectively. These were selected to be 0.1 and 200 for the baseline survey, respectively, and 5 and 200 for the monitor survey, respectively. The shaping filter gave the following removals displayed in Fig. 5.7 for small, medium, and large offset and depths.

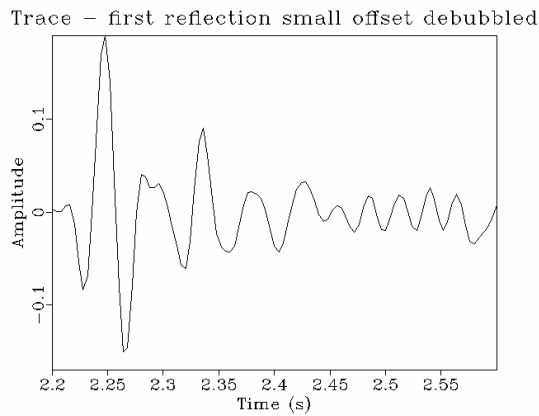


(a) Desired source wavelet for the baseline survey.

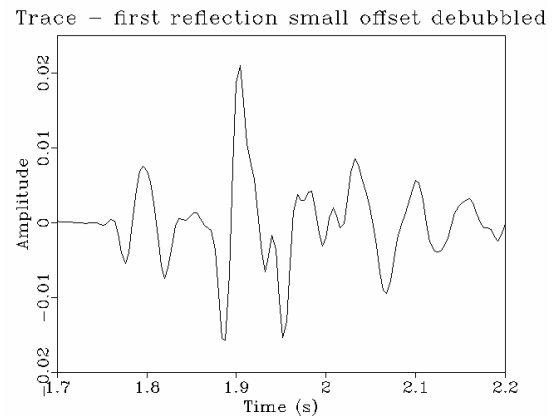


(b) Desired source wavelet for the monitor survey.

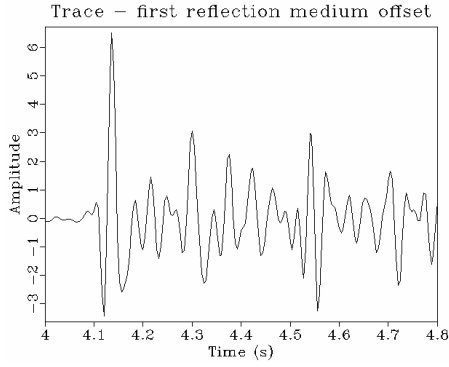
Figure 5.6: Desired source wavelets for the monitor and baseline surveys. The wavelets were created with emphasize on the first reflection shape, but began at the travelttime similar to the direct wave recorded at small offset.



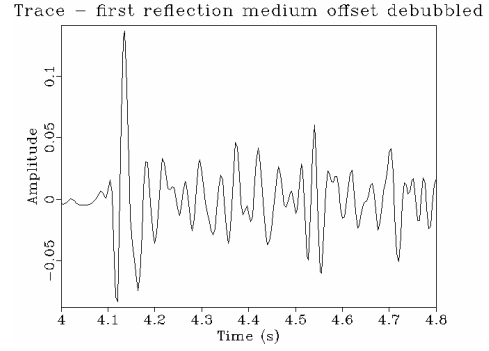
(a) Baseline survey: First small offset reflection debubbled.



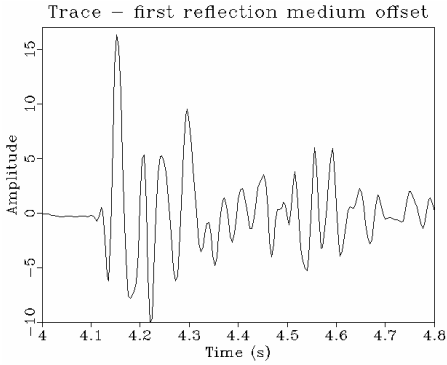
(b) Monitor survey: First small offset reflection debubbled.



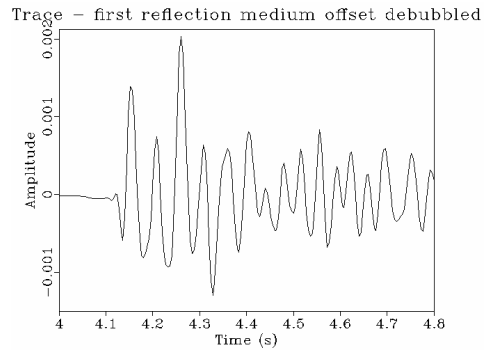
(c) Baseline survey: First medium offset reflection



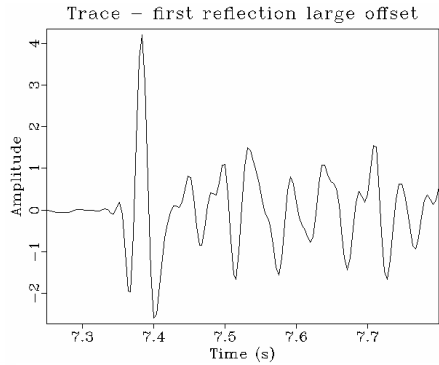
(d) Baseline survey: First medium offset reflection debubbled.



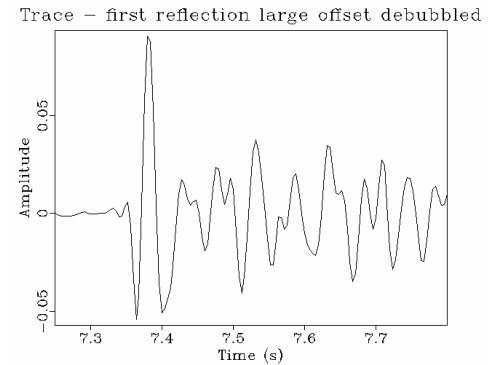
(e) Monitor survey: First medium offset reflection.



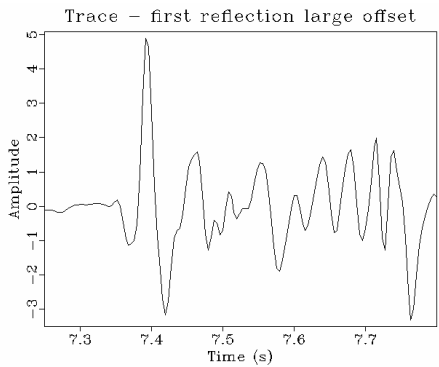
(f) Monitor survey: First medium offset reflection debubbled.



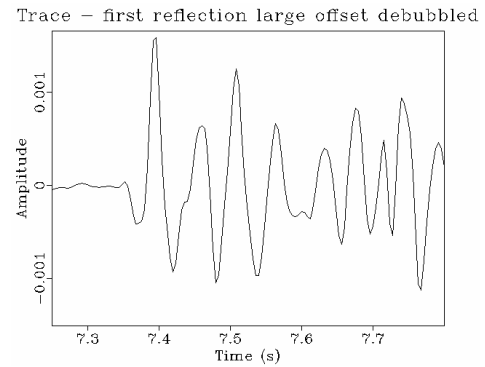
(g) Baseline survey: First large offset reflection



(h) Baseline survey: First large offset reflection debubbled.



(i) Monitor survey: First large offset reflection



(j) Monitor survey: First large offset reflection debubbled.

Figure 5.7: Trace display before and after applying debubble filter on the first reflection response at small, medium, and large offsets and depth.

5.5 Muting

The shot gathers were used as a way to display the data and as a quality control for the various processing steps at the early phases. The gathers before and after applying the various filters are hence displayed in Fig. 5.8. The top parts of the data were removed by using *sfmutter*, which uses the weight algorithm defined in Eq. 5.1 and multiplies the input data with either one or zero depending on the parameters set in the equation. A linear equation for this muting algorithm was created with the default values of $\Delta t = 0.15$ and $x_0 = 0$. The total shots were separated into smaller parts before applying the mute to each part. The shot separation and muting parameters are displayed in Table 5.4. The obtained muting for shallow, medium and deep events are displayed in Fig. 5.9.

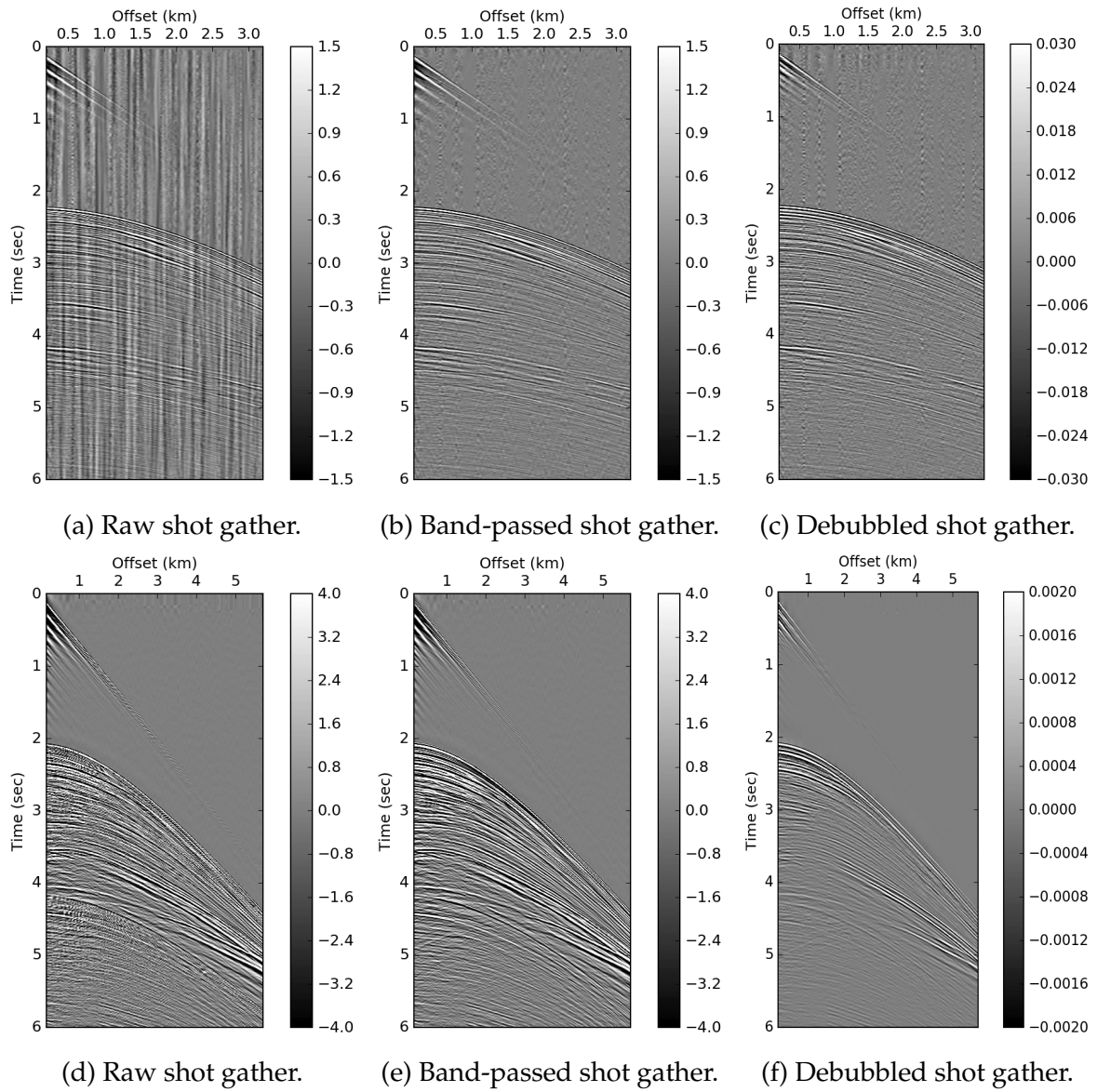


Figure 5.8: Shot gather of shallow depth events from the baseline (a-c) and monitor surveys (d-f). The debubbled shot gather is also despiked.

$$W(t, x) = \begin{cases} 0 & \text{for } t - t_0 < \frac{1}{v_0}(x - x_0) \\ 1 & \text{for } t - t_0 > \Delta t + \frac{1}{v_0}(x - x_0) \end{cases} \quad (5.1)$$

Table 5.4: Parameters for upper mute using Eq.5.1.

(a) Parameters for baseline mute.			(b) Parameter for monitor mute.		
Data parts	t_0	v_0	Data parts	t_0	v_0
Part 1: 0 - 1000	1.80	2700	Part 1: 0 - 1000	1.35	2700
Part 2: 1000 - 2000	2.5	3700	Part 2: 1000 - 2000	2.5	3700
Part 3: 2000 - 3000	4.0	4800	Part 3: 2000 - 3000	4.0	4800
Part 4: 3000 - 5494	5.4	5000	Part 4: 3000 - 4201	5.4	4800

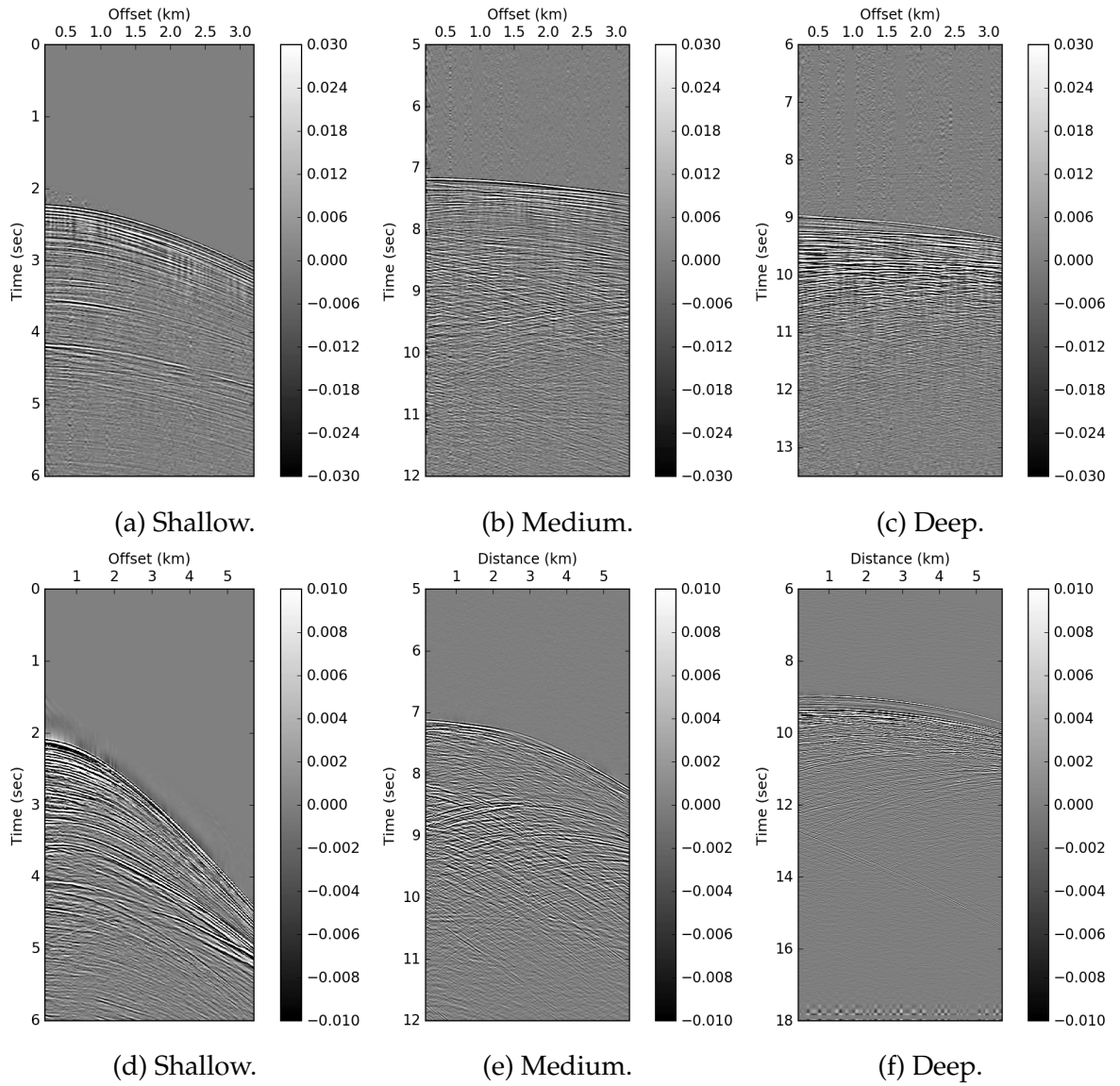


Figure 5.9: Shot gather of shallow, medium, and deep depth events from the baseline (a-c) and monitor surveys (d-f) after applying top mute.

5.6 CMP sorting

The data were transformed from shot gathers to CMP gathers using *sfshot2cmp*, which transformed the data's 3D cube into a new 3D cube with time, offset, and CMP. The output of this program gave 22095 CMPs with a spacing of 12.5 m between the midpoints for the baseline survey and 34051 CMPs with 6.25 m spacing for the monitor survey (Table 5.5). The number of traces per CMP, *fold*, was calculated using Eq. 3.6 and was 30 and 55.5 for the baseline and monitor survey, respectively (Eqs. 5.1 and 5.2).

Table 5.5: 3D geometry for the CMP converted surveys.

(a) Baseline survey.

Window size	Sampling dimension	axis origin	Label and unit
n1 = 3375	d1 = 0.004	o1 = 0	Time (s)
n2 = 30	d2 = 100	o2 = 200	Offset (m)
n3 = 22095	d3 = 12.5	o3 = 100	Midpoint (m)

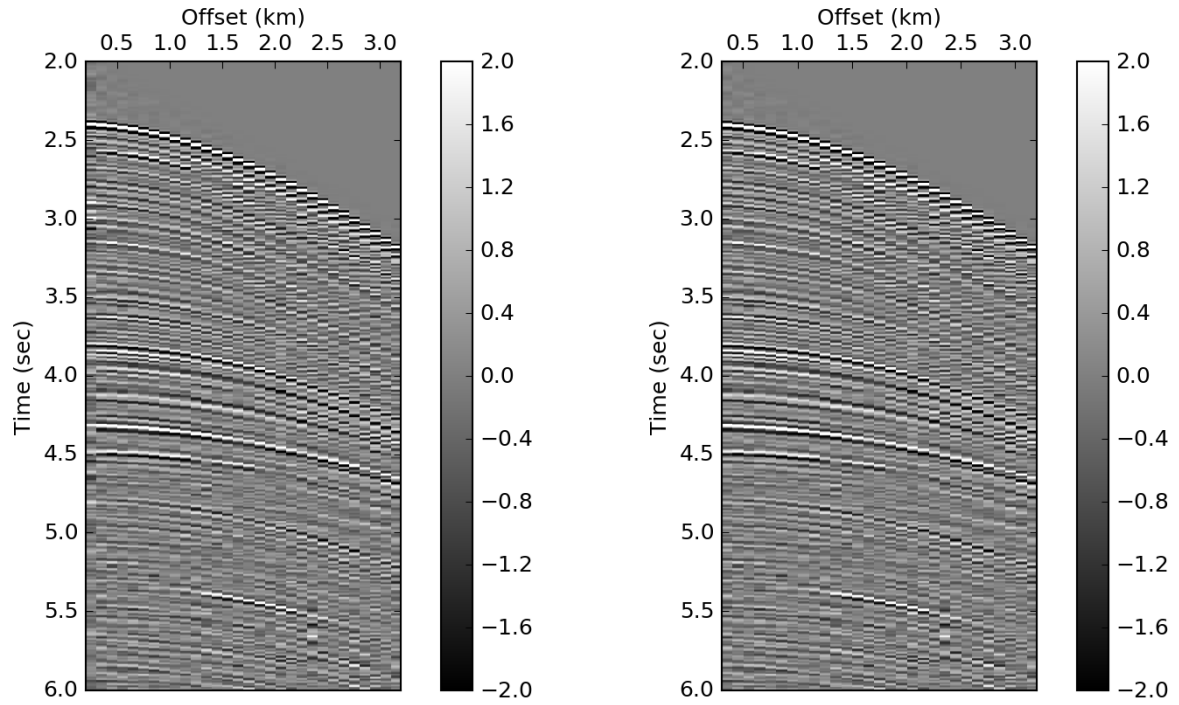
(b) Monitor survey.

Window size	Sampling dimension	axis origin	Label and unit
n1 = 4501	d1 = 0.004	o1 = 0	Time (s)
n2 = 55.5	d2 = 100	o2 = 159.24	Offset (m)
n3 = 34051	d3 = 6.25	o3 = 79.62	Midpoint (m)

$$fold_{baseline} = \frac{120 \cdot 12.5}{50} = 30 \quad (5.1)$$

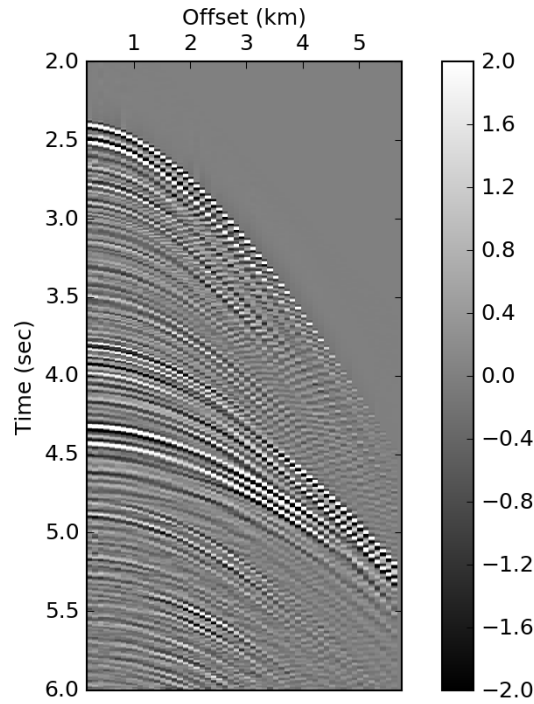
$$fold_{monitor} = \frac{444 \cdot 6.25}{50} = 55.5 \quad (5.2)$$

The baseline survey still contained bad traces on the nearest offset part of the CMP gather after despiking (Fig. 5.10a). This trace was hence removed and gave only 29 traces (folds) per CMP gather for further processing of this survey (Fig. 5.10b). The CMP traces in the monitor survey did not contain any visual bad traces and all CMPs were processed further for the velocity analysis (Fig. 5.10c).



(a) Baseline: CMP gather at a selected Location 1 (L1).

(b) Baseline: CMP gather at Location 1 (L1) after trace removal.



(c) Monitor: CMP gather at similar location, Location 1 (L1).

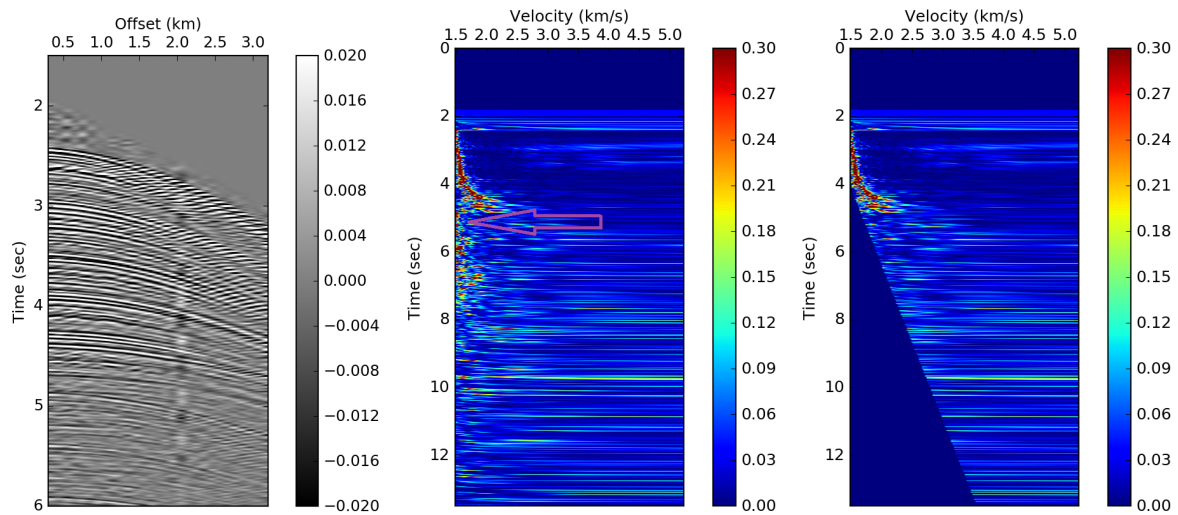
Figure 5.10: CMP gather from the baseline survey before and after CMP trace removal (a-b) and a CMP gather of the monitor survey (c) at Location 1 (L1). Their locations are set to be approximately the same. The amplitudes are multiplied by 100 and 1000, respectively for display. The resolution is poor due to the CMP spacing, which was 25 m in the baseline survey and 6.25 m in the monitor survey.

5.7 Velocity analysis, NMO correction and stacking

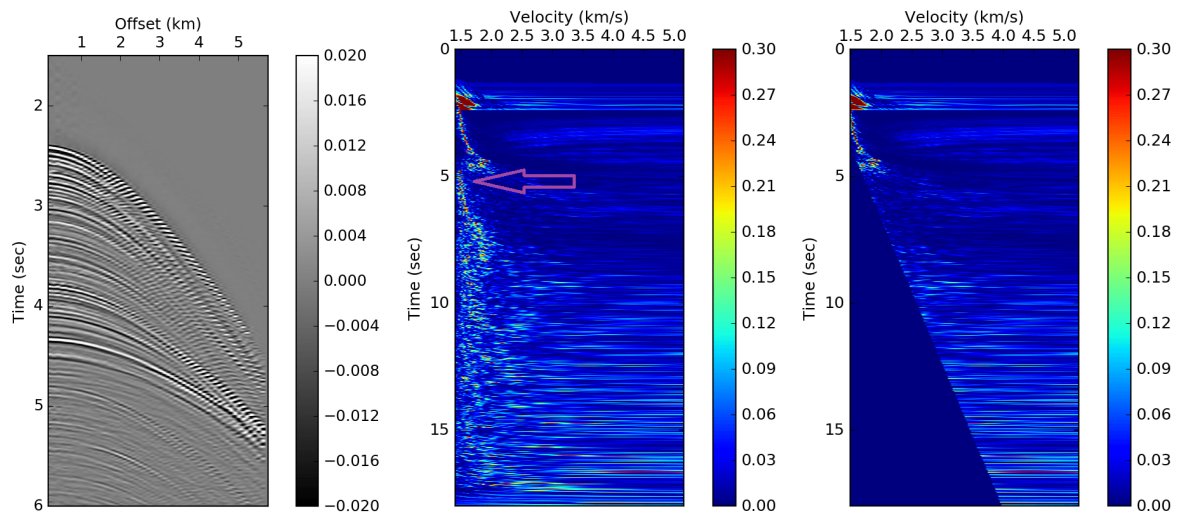
The velocity analysis was performed with *sfvscan*, which is based on the semblance function (Eq. 3.7) together with parameters for first scanned velocity v_0 , number of velocities to be scanned nv , and the interval velocity steps dv . These were selected to be 1480 m/s and 150, respectively, and with an interval velocity steps of 25 m/s, and corresponds to a maximum scanned velocity of 5230 m/s.

Three CMP locations are displayed in Fig. 5.11 together with their corresponding velocity semblances. The semblances showed a pattern of increasing high amplitude responses and sudden drop/decrease (marked by arrow), where the drop are believed to be multiples present. The velocity picking was performed using the automatic program, *sfpick*, which picked the highest responses of the semblances beginning at $vel0 = 1480$ m/s. To prevent picking of multiples, a combination of various muting parameters were performed using *sfmutter* on the semblance responses (see Appendix A.4 for parameters). The muting was done to provide a guidance for the automatic picker to pick the velocities in an increasing manner (theoretically assuming that there is an increase of velocities with depth).

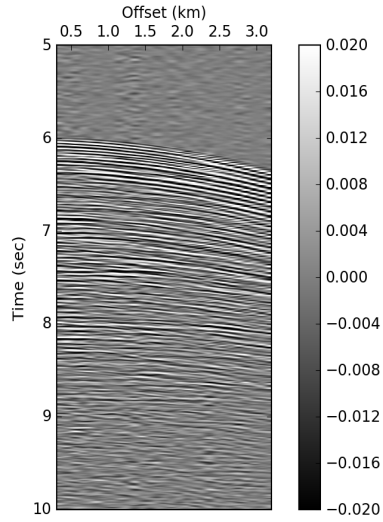
However, also due to unwanted anomalies such as picking higher velocities than 1480 m/s above the seabed, the data were split into three parts prior to both the velocity scan, muting and automatic picking. The velocity model was then smoothed using *sfsmooth* with the controlling parameters *rect#* for smoothing radius. The parameters *rect1* and *rect2* were selected to be 100 and 150, respectively, and with a low-cut of 1480 m/s using *sfclip2*. The low-cut parameter prevented lower velocities than the value set to be presented in the model after the smoothing.



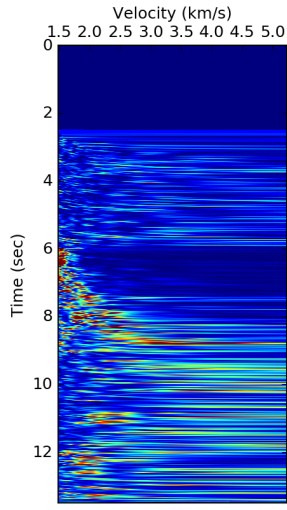
(a) Baseline: CMP gather at L1. (b) Velocity semblance at L1. (c) Muted velocity semblance at L1.



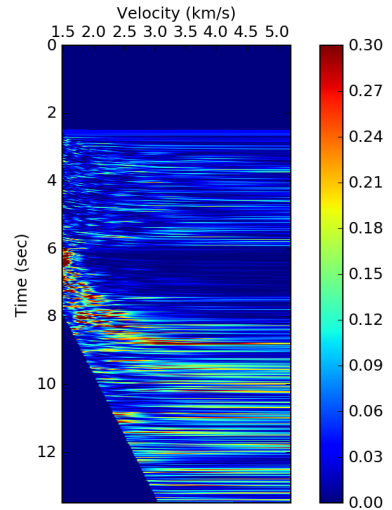
(d) Monitor: CMP gather at L1. (e) Velocity semblance at L1. (f) Muted velocity semblance at L1.



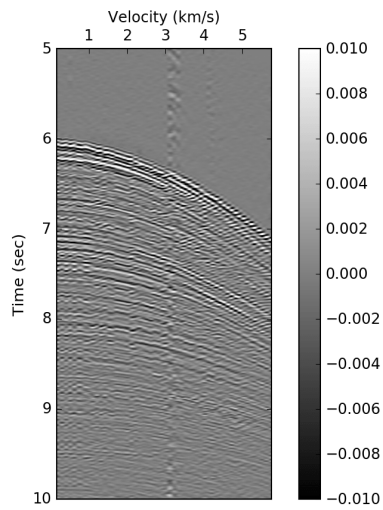
(g) Baseline: CMP gather at L2.



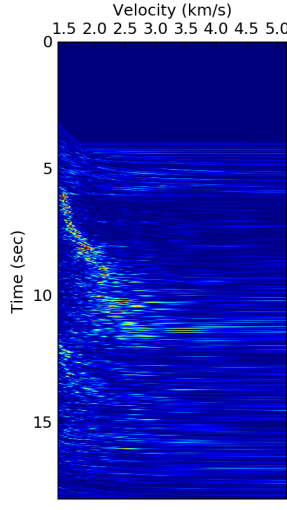
(h) Velocity semblance at L2.



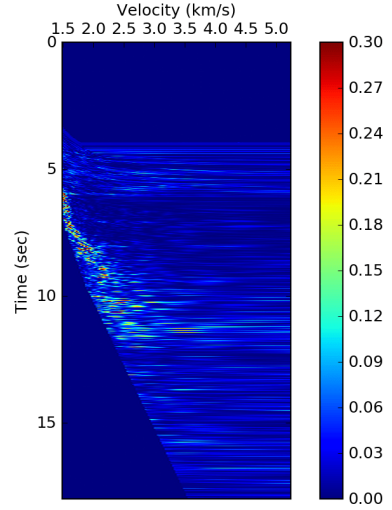
(i) Muted velocity semblance at L2.



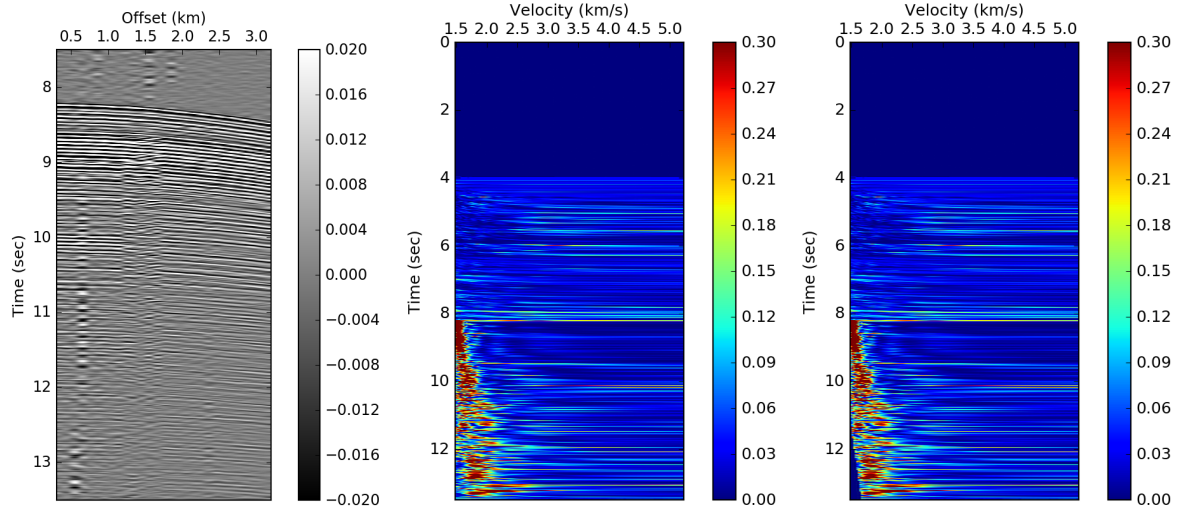
(j) Monitor: CMP gather at L2.



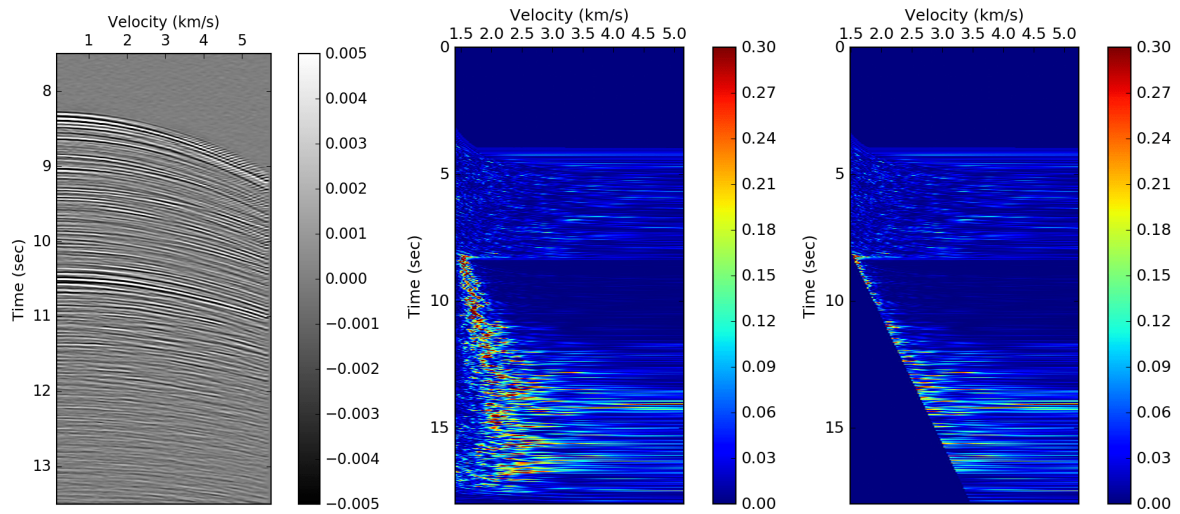
(k) Velocity semblance at L2.



(l) Muted velocity semblance at L3.



(m) Baseline: CMP gather at L3. (n) Velocity semblance at L3. (o) Muted velocity semblance at L3.



(p) Monitor: CMP gather at L3. (q) Velocity semblance at L3. (r) Muted velocity semblance at L3.

Figure 5.11: CMP gather at three locations (L1, L2, L3) with their corresponding velocity semblances before and after inner mute. The locations are approximated to be at the same location in both surveys for comparison. The TWT (y-axis) of the CMP gathers are shortened to illustrate the NMO curvatures at the various depths/locations. The CMP gathers were also interpolated to create a smoother display.

The CMP gathers were then processed through a NMO correction using *sfnmo* with the smoothed velocity models. The NMO corrected gathers in the monitor survey were shortened to 40 folds due to over-correction of events (possible refractions), which will be more explained in Chapter 6. The gathers were stacked together using *sfstack* where the parameter *axis* was set to be 2, which is the dimensions to stack. By stacking the data, the 3D geometry of the surveys changed over to a stacking image with dimensions $n3=1$ and $n2=Total\ CMP$ (Table 5.6).

Table 5.6: 3D geometry for the stacked surveys.

(a) Baseline survey.

Window size	Sampling dimension	axis origin	Label and unit
$n1 = 3375$	$d1 = 0.004$	$o1 = 0$	Time (s)
$n2 = 22095$	$d2 = 12.5$	$o2 = 100$	Midpoint (m)
$n3 = 1$	$d3 = 12.5$	$o3 = 100$	Midpoint (m)

(b) Monitor survey.

Window size	Sampling dimension	axis origin	Label and unit
$n1 = 4501$	$d1 = 0.004$	$o1 = 0$	Time (s)
$n2 = 34051$	$d2 = 6.25$	$o2 = 79.62$	Midpoint (m)
$n3 = 1$	$d3 = 6.25$	$o3 = 79.62$	Midpoint (m)

An amplitude recovery was also performed to the final stacks by using *sfshapeagc*, which controls the amplitude gain by a shaping regularization. This was applied instead of the typical *sfpow* that uses the exponential gain function (Eq. 3.5). The only parameter selected in *sfshapeagc* was *rect#*, which controls the smoothing of the shaping in #-axis. This was set to be 1000 in the first axis (*rect1=1000*) for both surveys with all other parameters being standard. The reason for this selection will be further discussed in Chapter 7. The amplitude recovery procedures was also performed after the time and depth migration.

5.8 Pre-stack migration

One of the final processing steps done to these data was a migration to move the reflectors to their true positions, collapse, focus diffractions, and to increase the resolution for better imaging. The data was time migrated using Pre-stack Kirchhoff migration and a experimental depth migration was performed using acoustic wave migration. These methods will hence be explained below.

5.8.1 Kirchhoff migration

Kirchhoff migration builds on a model where any subsurface point scatter energy along the computation of travel time from any given source to any given receiver. A coherent reflection is produced by arrangement of these scatterpoints where the objectives of this particular migration are to collect all the scatter energy and relocate it to the scatterpoint position. This method assumes an output scatterpoint (a location) and sums appropriate energy from all input traces and repeats for every output sample. The Kirchhoff time migration assumes straight raypaths from source to receiver as displayed in Fig. 5.12. The total travel time t is calculated by an addition of the source to scatter point time t_s and the scatterpoint to receiver time t_r (Eq. 5.1) (Bancroft et al., 1998).

The total traveltime is then solved by using the model displayed in Fig. 5.12 where x is the horizontal distance between scatterpoint (located at $x = 0$) and CMP and h if half the source-receiver distance (Eq. 5.2). Assuming a constant velocity for the moment gives a relationship between depth and velocity as z_0/v which are equivalent to $t_0/2$. Modifying the expression shown in Eq. 5.2 gives the following expression in Eq. 5.3 where v is the migration velocity and the RMS approximation evaluated at $t_0 = t(x = 0, h = 0)$. This is hence equivalent to the expression shown in Eq. 5.4 (Bancroft et al., 1998).

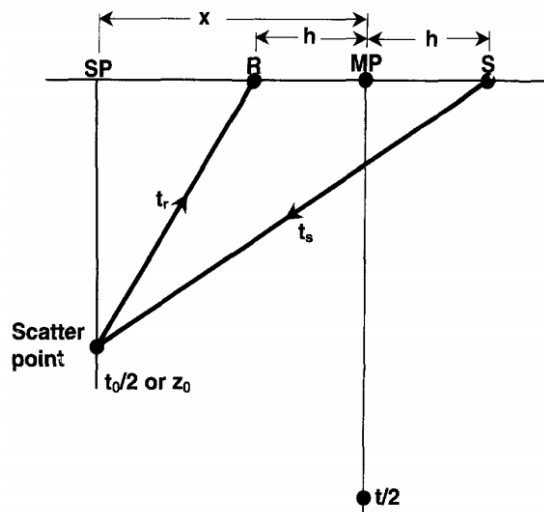


Figure 5.12: Subsurface model of the Kirchhoff pre-stack time migration. Figure from Bancroft et al. (1998).

$$t = t_s + t_r \quad (5.1)$$

$$t = \sqrt{\frac{z_0^2 + (x + h)^2}{v^2}} + \sqrt{\frac{z_0^2 + (x - h)^2}{v^2}} \quad (5.2)$$

$$t = \sqrt{\left(\frac{t_0}{2}\right)^2 + \frac{(x + h)^2}{v^2}} + \sqrt{\left(\frac{t_0}{2}\right)^2 + \frac{(x - h)^2}{v^2}} \quad (5.3)$$

$$t_0 = \frac{2z_0}{V_{average}} \quad (5.4)$$

5.8.1.1 Procedure in Madagascar

The Kirchhoff pre-stack time migration in Madagascar was performed using *sfmig2*. The input data are required to be in a 3D cube with time, midpoint and offset axis, so the CMP data were hence transposed using *sftransp* with parameter *plane=23*. The numbers represent the axes to switch between, which are the offset (2) and CMP (3) axes (Table 5.7). The parameters for controlling the migration is the integral aperture, *apt*, which is the area where the migration sums and the aperture angle *angl*, which is the maximal angle for migration area. These were selected to be 40 and 90, respectively, for both surveys. The aperture angle 90 was a standard value set in the migration program.

Table 5.7: Transposed 3D geometry for the Kirchhoff pre-stack time migration.

(a) Baseline survey.

Window size	Sampling dimension	axis origin	Label and unit
n1 = 3376	d1 = 0.004	o1 = 0	Time (s)
n2 = 22095	d2 = 12.5	o2 = 100	Midpoint (m)
n3 = 30	d3 = 100	o3 = 200	offset (m)

(b) Monitor survey.

Window size	Sampling dimension	axis origin	Label and unit
n1 = 4501	d1 = 0.004	o1 = 0	Time (s)
n2 = 34051	d2 = 6.25	o2 = 79.62	Midpoint (m)
n3 = 55.5	d3 = 100	o3 = 159.24	offset (m)

The *sfmig2* program provides two output files; one with the migrated stack and one file with the NMO corrected common-offset image gathers (hereby abbreviated as COI gathers). The whole folds for both surveys were used during the migration, but only 40 folds was used for the migrated stack of the monitor survey due to the same reasons described for unmigrated stacking of this survey. To perform the similar procedure of stacking of the COI gathers on the monitor survey, the axes of the COI gathers had to be transposed back to the same geometry as the CMP gathers and then stacked together.

5.8.2 Full acoustic wave migration

The full two-way acoustic wave equation migration, also referred as the reverse-time depth migration, propagates the recorded wavefield from its boundary (recorded surface) into the earth using full wave equation with time reversing backwards (Fig. 5.13). For the full wave equation, it requires that it compute snapshots of the entire wavefield at all locations inside the earth at all times from latest to time zero. Concerning pre-stack migration, the recorded wavefield is still propagated back in time, but also where the source wavefield is created by propagating forwards in time. Hence explaining why this migration could be called forward and reverse migration. Considering seismic waves to be acoustic, the propagation engine in the two-way acoustic wave equation can be directly solved under following equation shown in Eq. 5.5 (Karazincir et al., 2008; Etgen et al., 2009).

$$\left(\frac{1}{V^2} \frac{\partial^2}{\partial t^2} - \frac{\partial^2}{\partial x^2} - \frac{\partial^2}{\partial y^2} - \frac{\partial^2}{\partial z^2} \right) p(x; t) = 0 \quad (5.5)$$

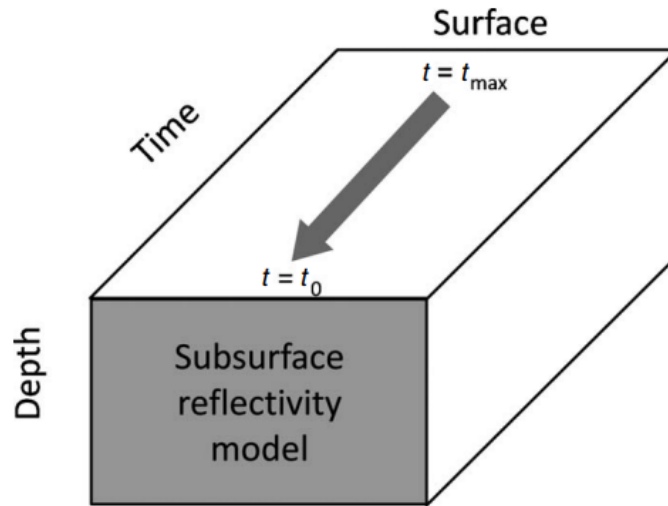


Figure 5.13: Schematically illustration of the reserve migration in two-space dimension. The wavefield is injected from the recorded maximum surface t_{max} into the subsurface, and then propagated backward until time zero. The migration for full wave acoustic propagates energy downwards and upwards with the computational volume. A vertical slice through the cube shows a snapshot of the wavefield at each time step, which is then crosscorrelated with the source wavelet that has propagated forward in time (Etgen et al., 2009). Figure from Etgen et al. (2009)

Consequently, a forward extrapolation of the source wavefield in time is performed and then a receiver wavefield is backward propagated in time as mentioned. The imaging condition is hence applied after each backward propagation time step, and the results are summed to form a partial image volume. The migration is applied to the shot gathers and their image volumes are partially summed to produce the final pre-stack depth image (Karazincir et al., 2008).

5.8.2.1 Procedure in Madagascar

The procedures performed for the pre-stack depth migration were as following:

- **Source wavelet**

A ricker wavelet was created for both surveys using *sfwavelet* with peak frequency at 20 Hz (Fig. 5.14), center of velocity at $t_0 = 0.1$ s, and length corresponding to total TWT length. Here, both TWT lengths of the wavelets were set to be 13.5 s. The wavelets were then transformed along the first axis using the Fast Fourier transform *ffft1*, and used in calculating the downgoing wavefield.

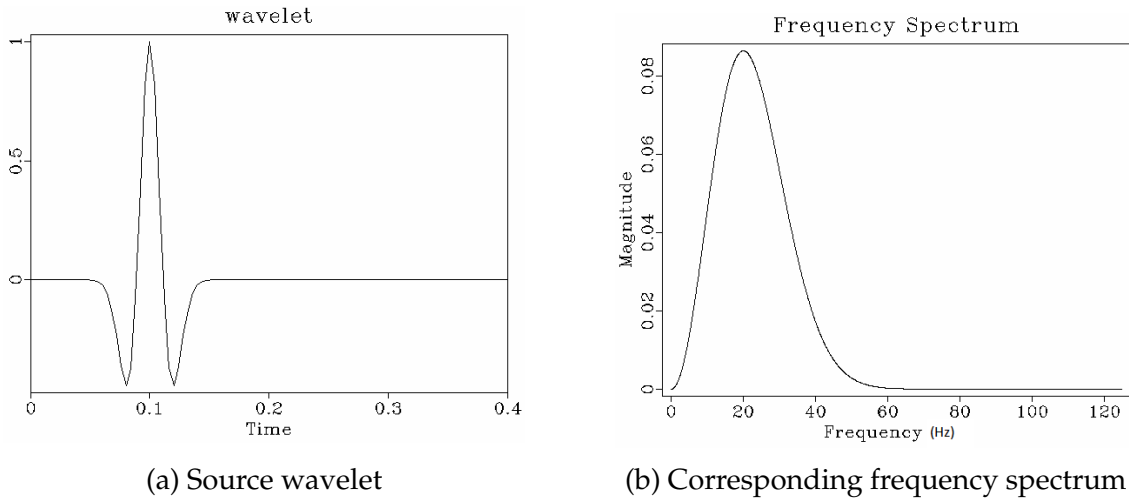


Figure 5.14: Source wavelet and corresponding frequency spectrum used for both surveys.

- **Geometry and header regulator**

A header file containing the acquisition parameter for shot gathers was created using *sfmakehdr3d* for the two surveys. The headers were then sorted into shots and a map to connect the shots and data created under the migration. The migration required an unstructured collection of trace as input and *n2* was set to be the total traces of 659280 and 1865244 for the baseline and monitor surveys, respectively, while *n3* was set to be one for both surveys.

- **Velocity model**

The velocity field in these surveys caused problems when considering the depth migration. The smoothed velocity model where transformed from RMS (picked velocities) to interval velocities using *sfdix*, and where the monitor velocity model was reduced to same TWT as the baseline survey. The velocities were also smoothed with *rect1=50* and *rect2=200* and low-cut of of 1480 ms/s. The dix conversion follows the formula shown in Eq. 3.11. The velocities were also shifted from time to depth using *sftime2depth* controlled by the parameter *dz*, which is the depth sampling and *nz*, which is the total number of depth samples. These were hence selected to be 2.5 and 4800, respectively, for both surveys. The depth converted velocity models were then smoothed once more with *rect1=250* and *rect2=750*.

The pre-stack depth migration was performed using *sfnpicwem*, which computes the downgoing and upgoing wavefields, cross-correlate them and gives a large volume of partial depth migrated images. The migration was controlled by many minor parameter, which are not explained any further here, but to be found in the Appendix A.6. The modelling aperture *apert2* controls the aperture length in x-direction. A thumb-rule was that this should be between one to two times the maximum offset and was set to be 4000 for both surveys. The partial depth migrated images was then summed into one file using *sfnpistackcip2d*. The depth migrated stacks were then converted back to time using *sfdepthtotime* with the same depth velocity model and used as a quality control.

5.9 Conversion from RSF to SEG-Y

The migrated stacks were converted from RSF to SEG-Y format using *sfseggywrite*. This program requires a header file, which was created using *sfmakehdr3d*. The parameter set in this header file is the number of CMPs *nsx*, CMP spacing *dsx*, total time samples *nt*, time sampling interval *dt*, and CMP spacing *snx*. For the depth migration header files, *nt* corresponds to total number of depth sampling *nz* and *dt* corresponds to depth sampling *dz*. The origin of *sy* and *sx* coordinates were also defined in the header file where the baseline survey's *sx* coordinate was set to be 18250 m and zero for the monitor survey. The *sy* coordinate was set to be zero for both surveys. This is the navigational shift done to the surveys, which was described in Chapter 4.2 and done to perform the time-lapse interpretation using the seismic interpretation software, Petrel.

6 | Results

6.1 Processing results

The processing began with regularization and geometric correction where the surveys were interpolated to a pre-defined datum plane using the modified Shepard's method and a velocity input function. After this step, the data were processed through a band-pass, despiking and a debubble filter. Without the debubble filter, the bubble reflector was observed as a strong continuous amplitude (Figs. 6.1a and 6.1d). The results of the debubble filter is displayed in Figs. 6.1b and 6.1e, and the gain corrected stack of the same section displayed in Figs. 6.1c and 6.1f.

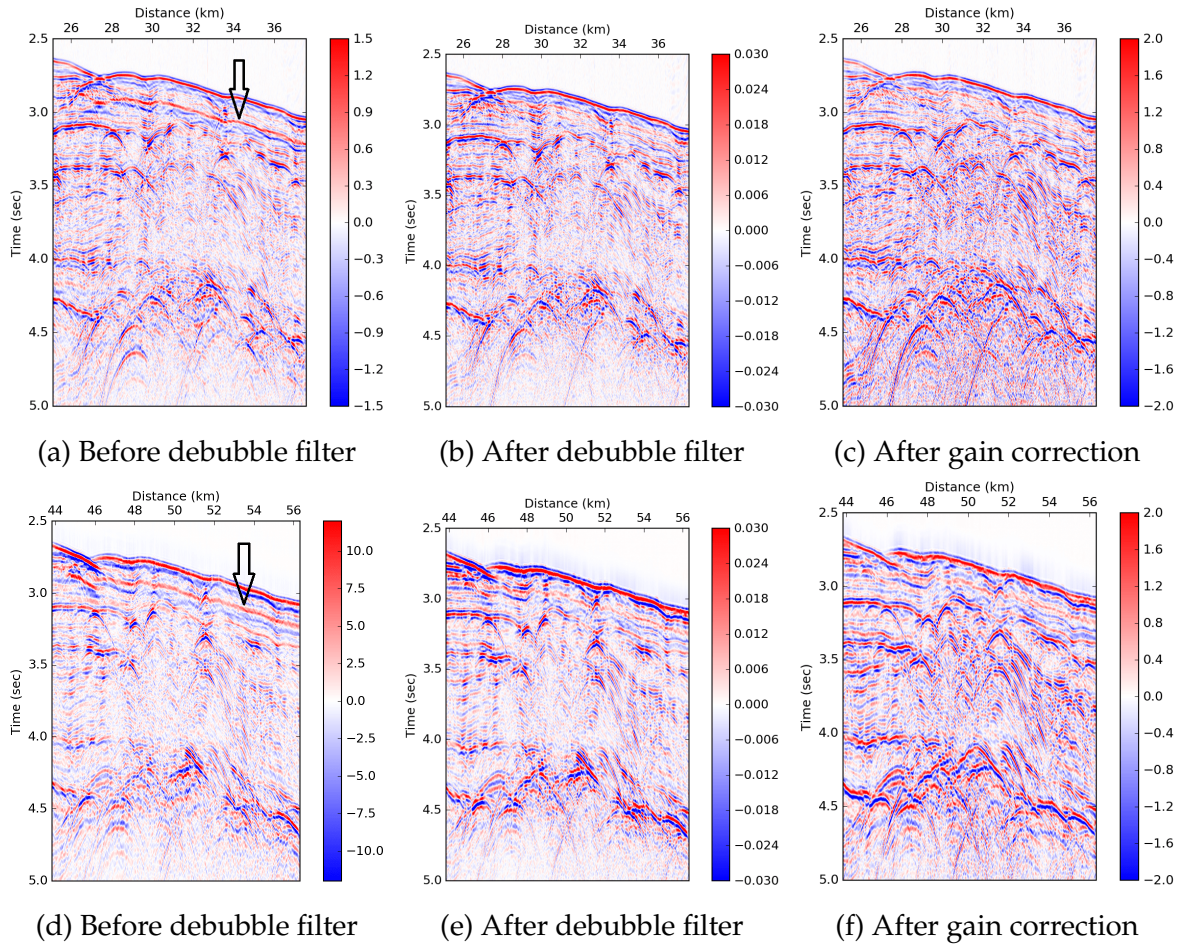
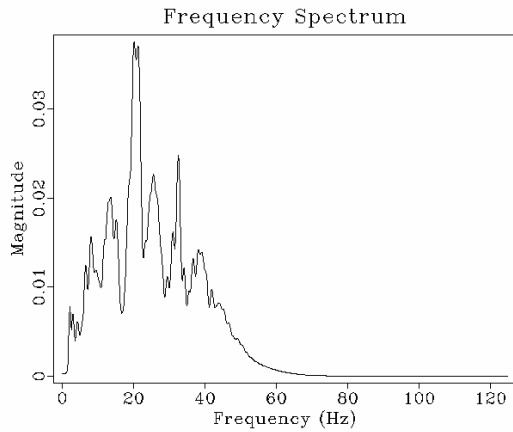
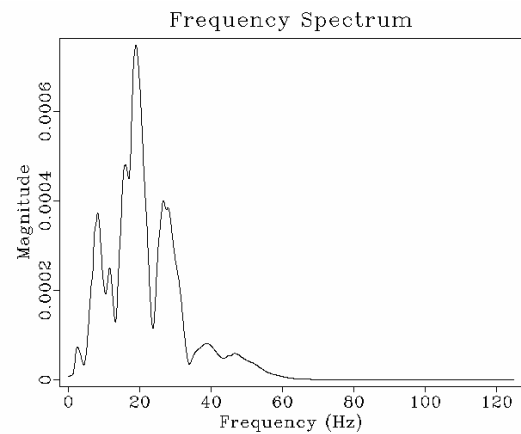


Figure 6.1: Comparison of shallow unmigrated stack before and after debubbling filter and gain correction on the baseline (a-c) and monitor (d-f) surveys. The bubble was observed as a strong continuous reflection. For location, see B1 and M1 in Fig. 6.8.

The frequency spectrum in the surveys underwent changes as a result of the debubble filter with drastic loss of magnitudes and a peak amplitude observed at approximately 20 Hz (Fig. 6.2). The debubble filter and band-pass filters also changed the PB-ratio for both surveys at small offset, which were found using Eq. 3.2. A PB-ratio increase from initial 2.14 to 5.5 was roughly calculated based on the amplitudes in Figs. 6.3a and 6.3c from the baseline survey. A PB-ratio decrease from initial 4 to 3.37 was roughly calculated based on the amplitudes in Figs. 6.3b and 6.3d from the baseline survey (Eqs. 6.1, 6.2, 6.3 and 6.4).

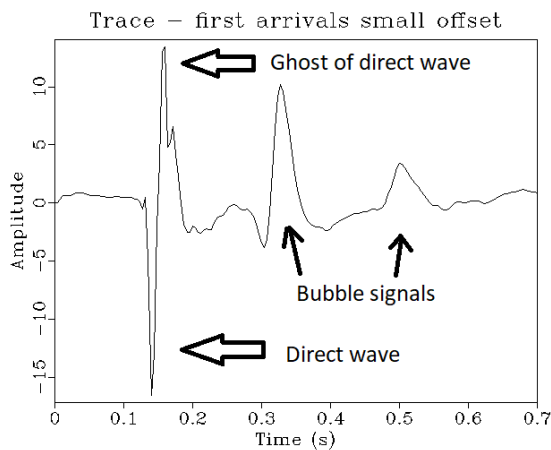


(a) Baseline debubbled frequency spectrum.

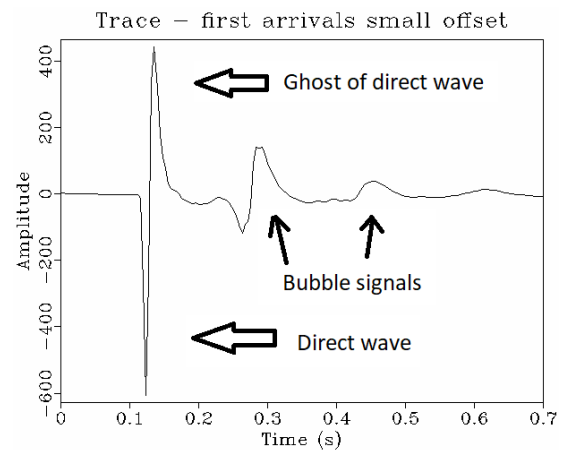


(b) Monitor debubbled frequency spectrum.

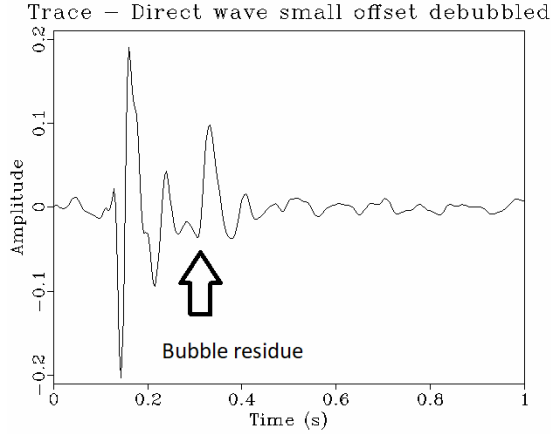
Figure 6.2: Frequency spectrum of the debubbled baseline and monitor surveys. The low amplitude decays are observed as the destructive primary-ghost interference.



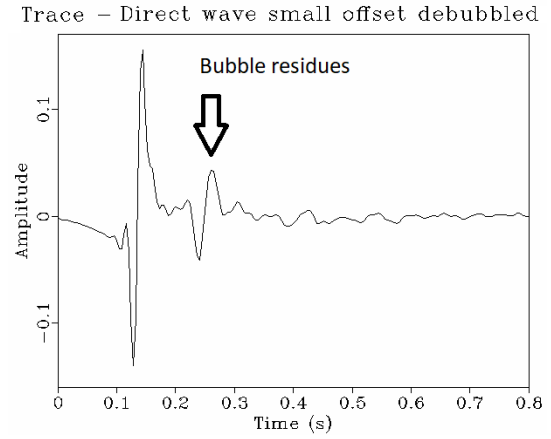
(a) Baseline: Direct wave small offset without any filter.



(b) Monitor: Direct wave small offset without any filter



(c) Baseline: Direct wave at small offset after debubble filter.



(d) Monitor: Direct wave at small offset after debubble filter.

Figure 6.3: The direct wave response from small offset from the baseline (a) and monitor (b) surveys before and after applying the debubble filter (and band-pass filter). Bubble residue are present after the filter.

$$\frac{P}{B} = \frac{30}{14} = 2.14 \text{ PB-ratio for baseline survey before applying debubble flt.} \quad (6.1)$$

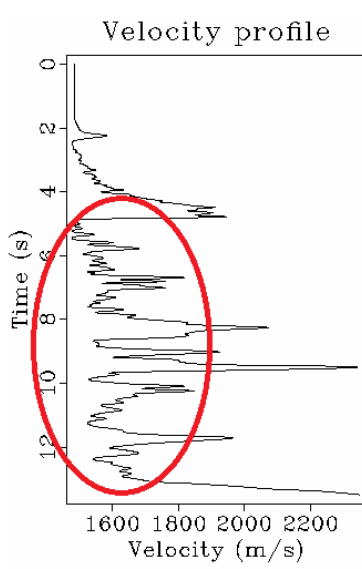
$$\frac{P}{B} = \frac{0.55}{0.1} = 5.5 \text{ PB-ratio for baseline survey after applying debubble flt.} \quad (6.2)$$

$$\frac{P}{B} = \frac{1040}{260} = 4 \text{ PB-ratio for monitor survey before applying debubble flt.} \quad (6.3)$$

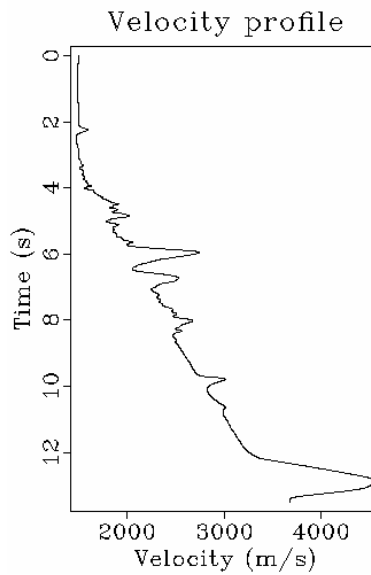
$$\frac{P}{B} = \frac{0.29}{0.086} = 3.37 \text{ PB-ratio for monitor survey after applying debubble flt.} \quad (6.4)$$

The top mute algorithm applied on the data revealed that noises above the reflectors were not removed due to the drastic increasing depths for each separated muting part. This contributed to anomalies in the velocity analysis and picking where semblance responses in the sea water (where the noise was not removed) had high amplitude responses over 1480 m/s.

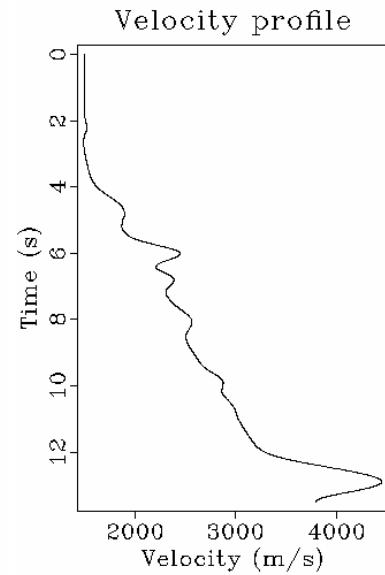
The velocity semblances obtained from both surveys generally showed a various pattern with high amplitude semblance responses stretched in horizontal direction at greater depths (Fig. 6.4). As multiples were picked (see Fig. 6.4) when using the automatic picking algorithm, the semblances were hence successfully muted to guide the picker to pick higher semblance values (amplitudes). The results of the automatic picked and smoothed velocity profiles at the three CMP locations are displayed in Fig. 6.4 where something the picked velocities removed uneven picked velocities and created a relatively smooth and increasing velocity trend.



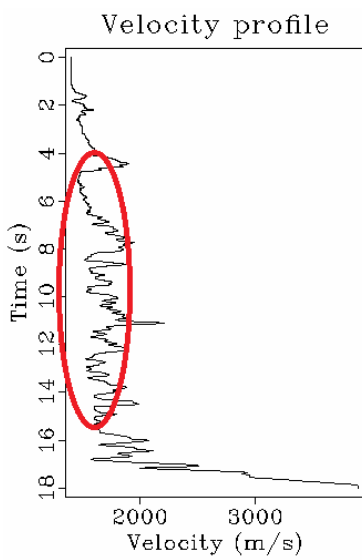
(a) Baseline: Vel. profile at L1 before semblance mute.



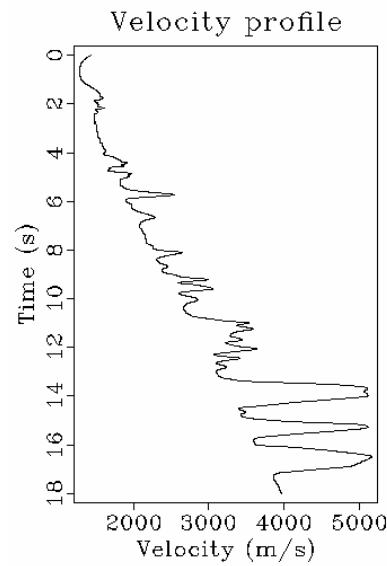
(b) Baseline: Vel. profile at L1 after semblance mute.



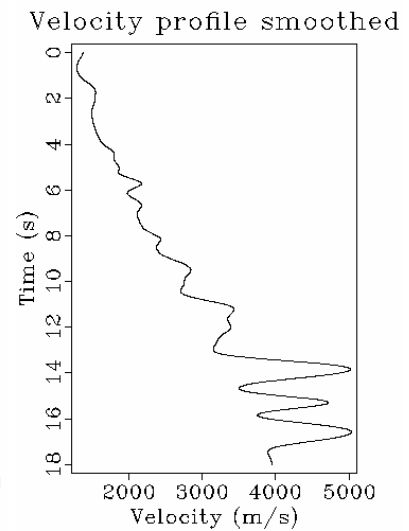
(c) Baseline: Smoothed vel. profile at L1.



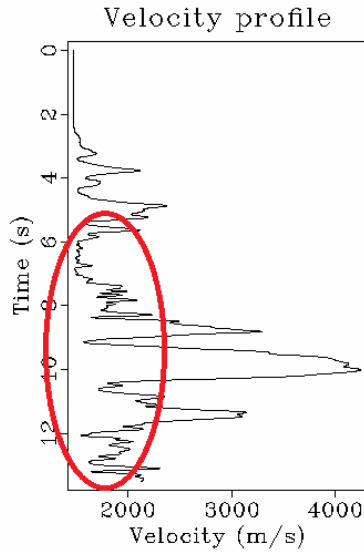
(d) Monitor: Vel. profile at L1 before semblance mute.



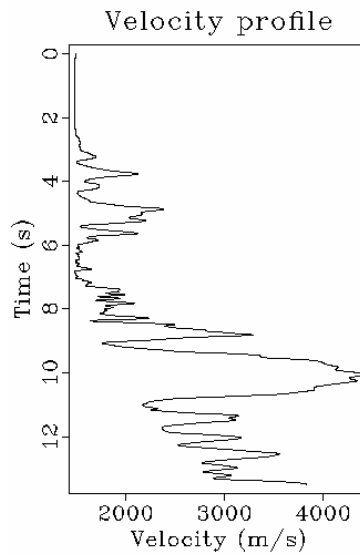
(e) Monitor: Vel. profile at L1 after semblance mute.



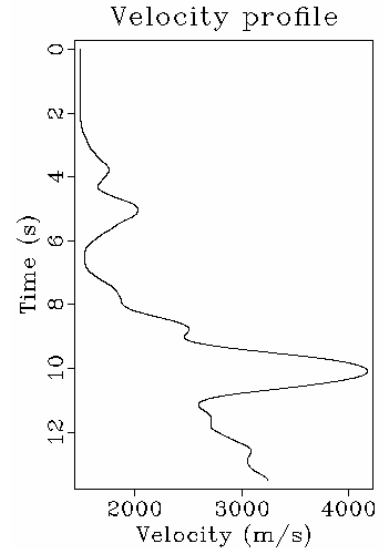
(f) Monitor: Smoothed vel. profile at L1.



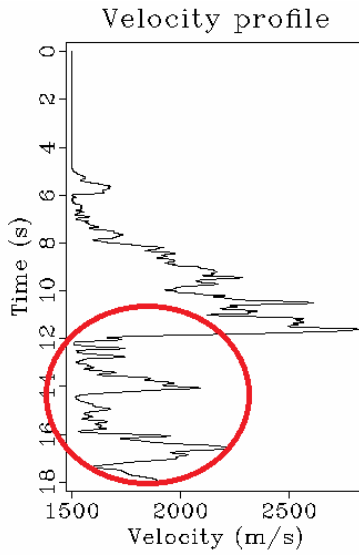
(g) Baseline: Vel. profile at L2 before semblance mute.



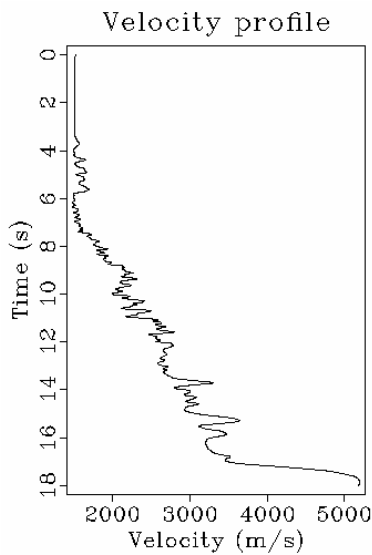
(h) Baseline: Vel. profile at L2 after semblance mute.



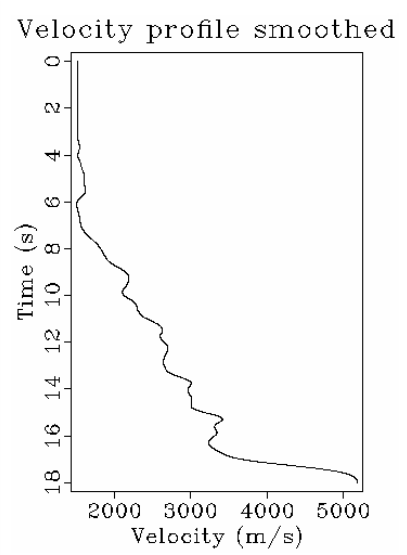
(i) Baseline: Smoothed vel. profile at L2.



(j) Monitor: Vel. profile at L2 before semblance mute.



(k) Monitor: Vel. profile at L2 after semblance mute.



(l) Monitor: Smoothed vel. profile at L2.

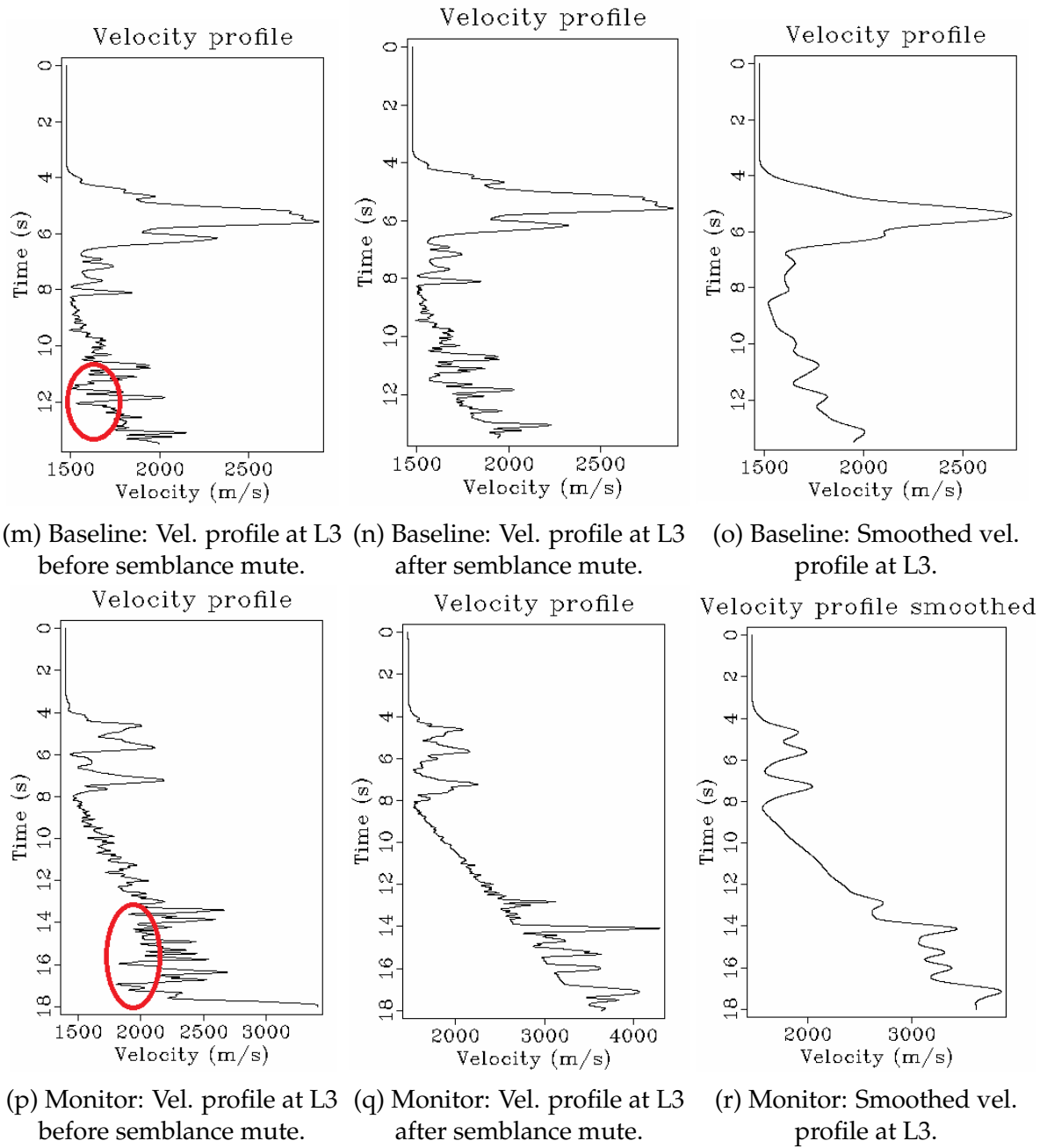


Figure 6.4: Comparison of velocity profiles at the three CMP locations (L1,L2,L3) before and after semblance mute, and after smoothing. The red circles mark the areas that indicated picked velocities of multiple reflections. However, there are also some multiples picked outside these circles. See Fig. 5.11 for their corresponding CMP gather and semblance scans.

Without dividing the data prior to the velocity analysis and picking, a scenario of high velocity anomalies in the sea water would be present as displayed in Fig. 6.5 only for the baseline survey. The new velocity models for both surveys were successfully obtained with minimal anomalies in the sea water and are displayed in Fig. 6.6 together with the velocity models obtained without semblance mute and after smoothing.

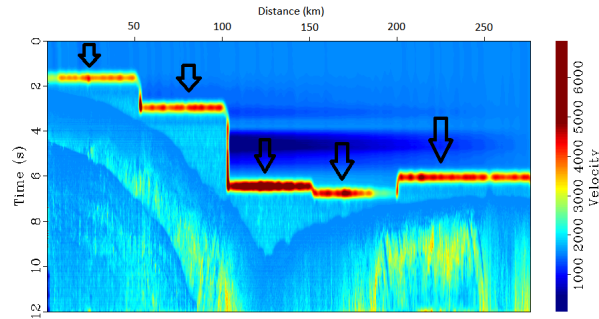
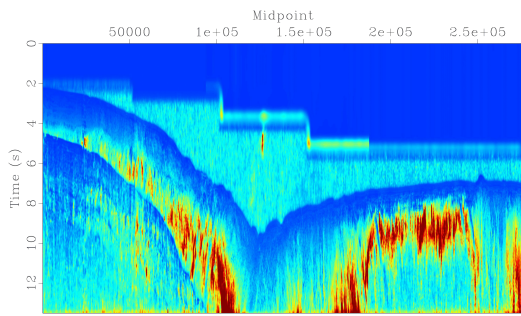
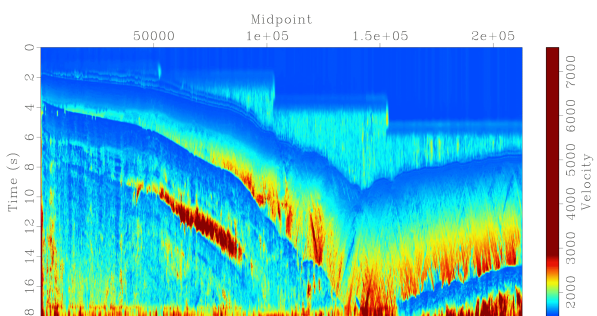


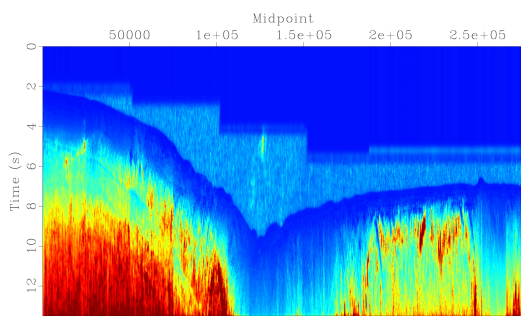
Figure 6.5: Velocity model obtained from performing the velocity analysis and automatic picking for the baseline survey without dividing the CMP data prior to the velocity analysis. The anomalies are marked with the arrows where velocities higher than 1480 m/s have been picked.



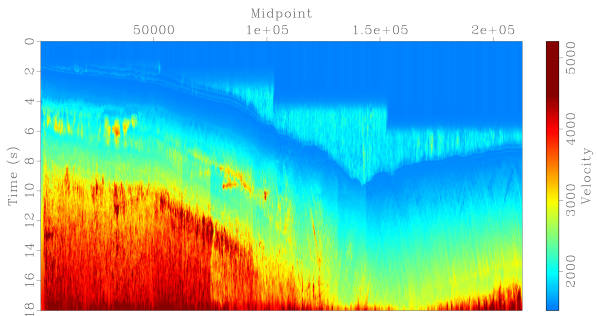
(a) Baseline velocity model obtained before semblance mute.



(b) Monitor velocity model obtained before semblance mute.



(c) Baseline velocity model obtained after semblance mute.



(d) Monitor velocity model obtained after semblance mute.

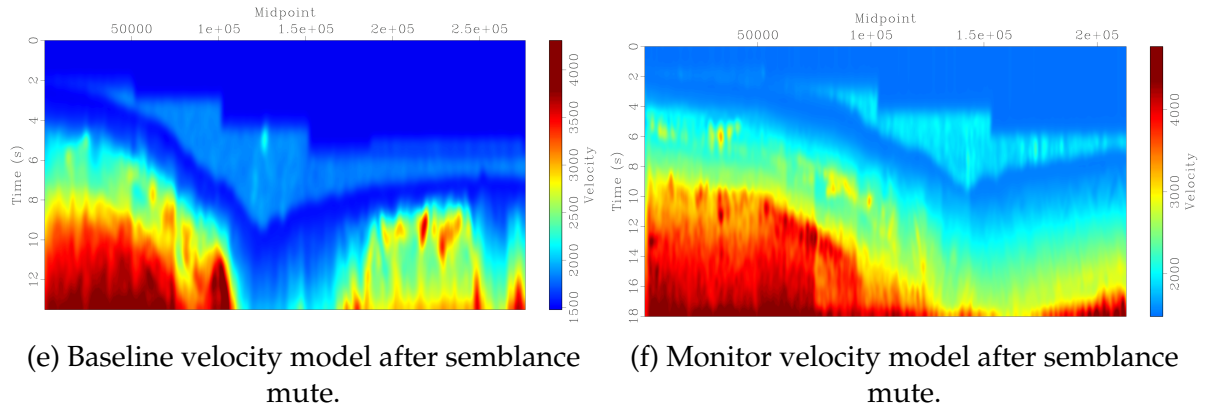
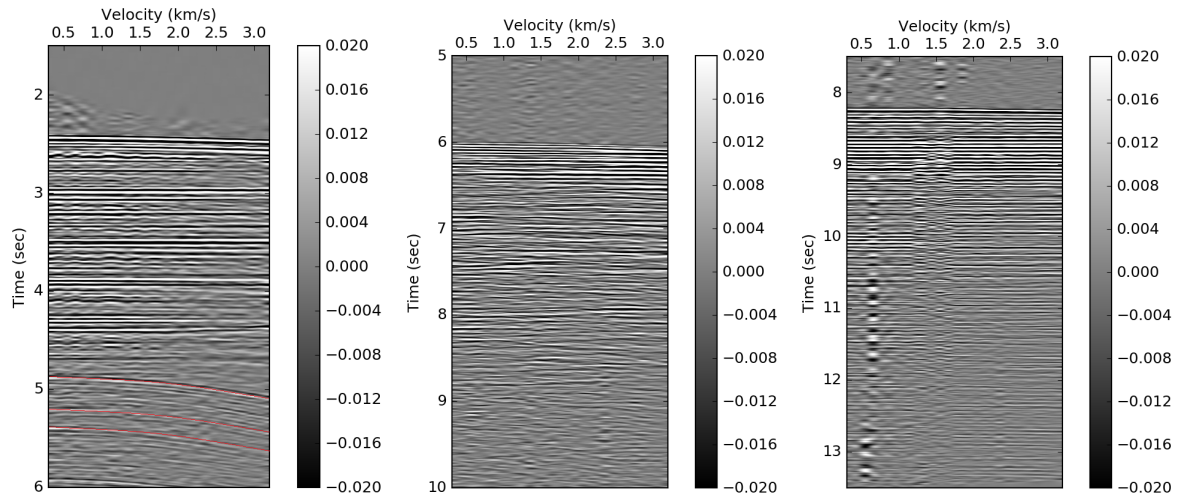


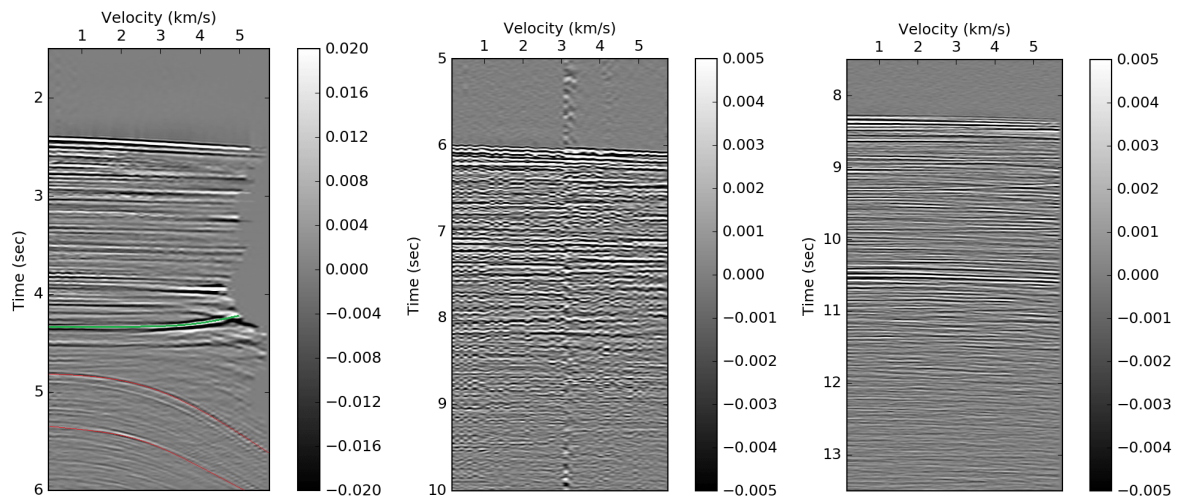
Figure 6.6: Velocity models for the surveys obtained before and after semblance mute, and after smoothing of the semblance muted velocity models.

The NMO corrected CMP gathers from the baseline and monitor surveys were acceptable to a certain degree as horizontal layered reflectors with no visible over- or under corrections of the reflections (Fig. 6.7). However, the multiples are under-corrected as a result of higher velocities being present in the velocity model. The NMO corrected CMP gathers from the monitor survey had a very small, yet noticeable under-correction of the seabed NMO corrected reflector (Fig. 6.7d). This was although acceptable as horizon as mentioned and only occurred on a few gathers at shallow depths. There were also indications of refractive events being overcorrected at large offsets, which gave destructive contribution to very large offset NMO corrected reflections in the monitor survey. Hence, the gathers from the monitor survey were shorted to 40 folds to avoid these events to be stacked over areas with horizontal reflectors (Figs. 6.7g to 6.7i).

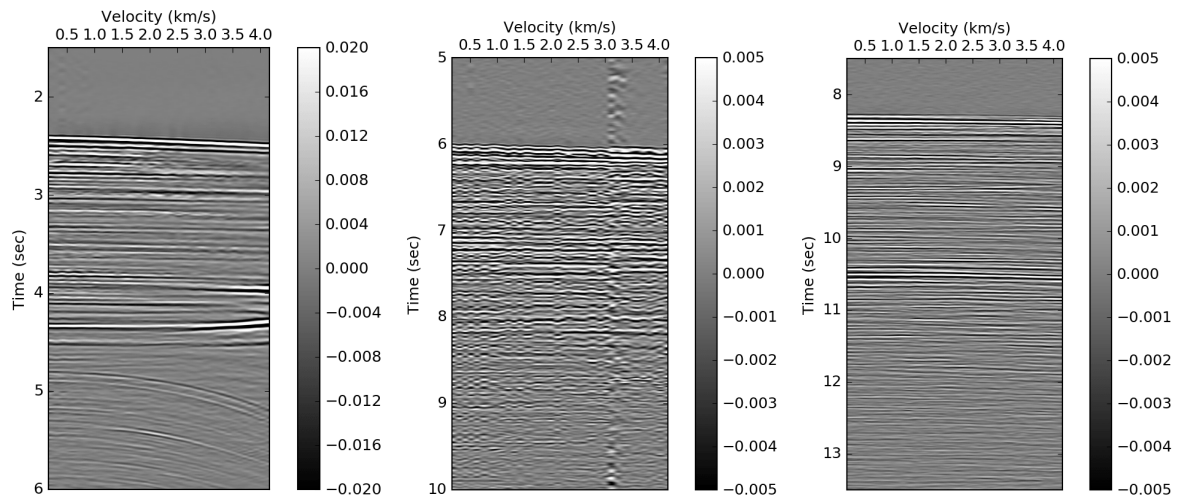
The brute stacks (first attempt) obtained from the surveys are displayed in Fig. 6.8 where it is revealed that there are a large number of diffractions observed at shallow and deep parts of the data. The amplitudes between the oceanic and continental plates made it difficult to observe the amplitudes of the layers. Hence, an amplitude recovery (*sfshapeagc*) was used to normalize the amplitudes and displayed in Fig. 6.9 where the multiples were clearly observed in the data. When performing the NMO correction and stacking using the semblance muted velocity models, stacks with suppressed multiples were observed (Fig. 6.10). The obtained stacks illustrate the first indication of the subduction zone where the Japan Trench is clearly observed. The stack from the monitor survey is also shorter in survey length than the baseline survey as described earlier, and with more data towards the west and with a greater TWT down to 18 s.



(a) Baseline: NMO corr. at L1. (b) Baseline: NMO corr. at L2. (c) Baseline: NMO corr. at L3.

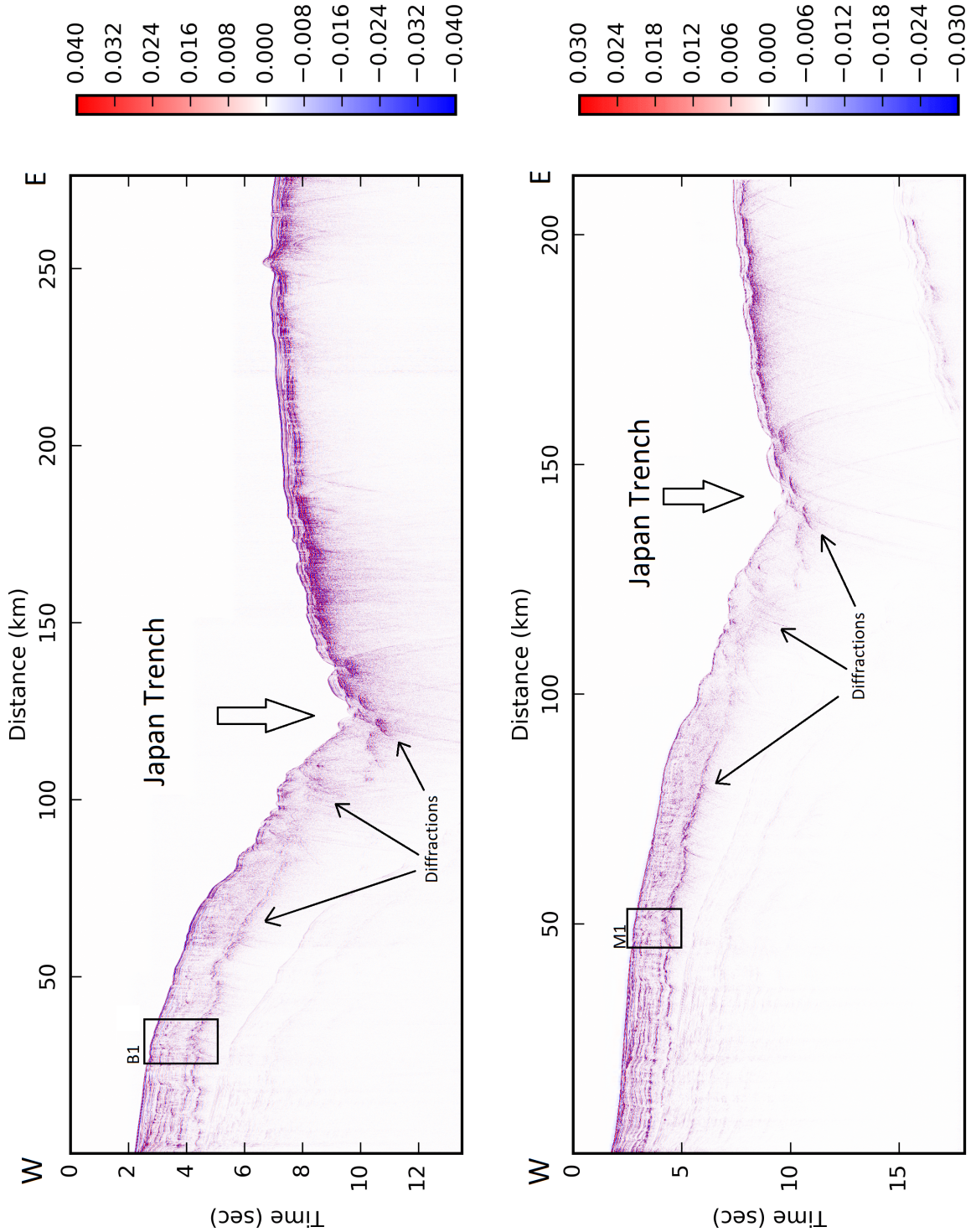


(d) Monitor: NMO corr. at L1. (e) Monitor: NMO corr. at L2. (f) Monitor: NMO corr. at L3.



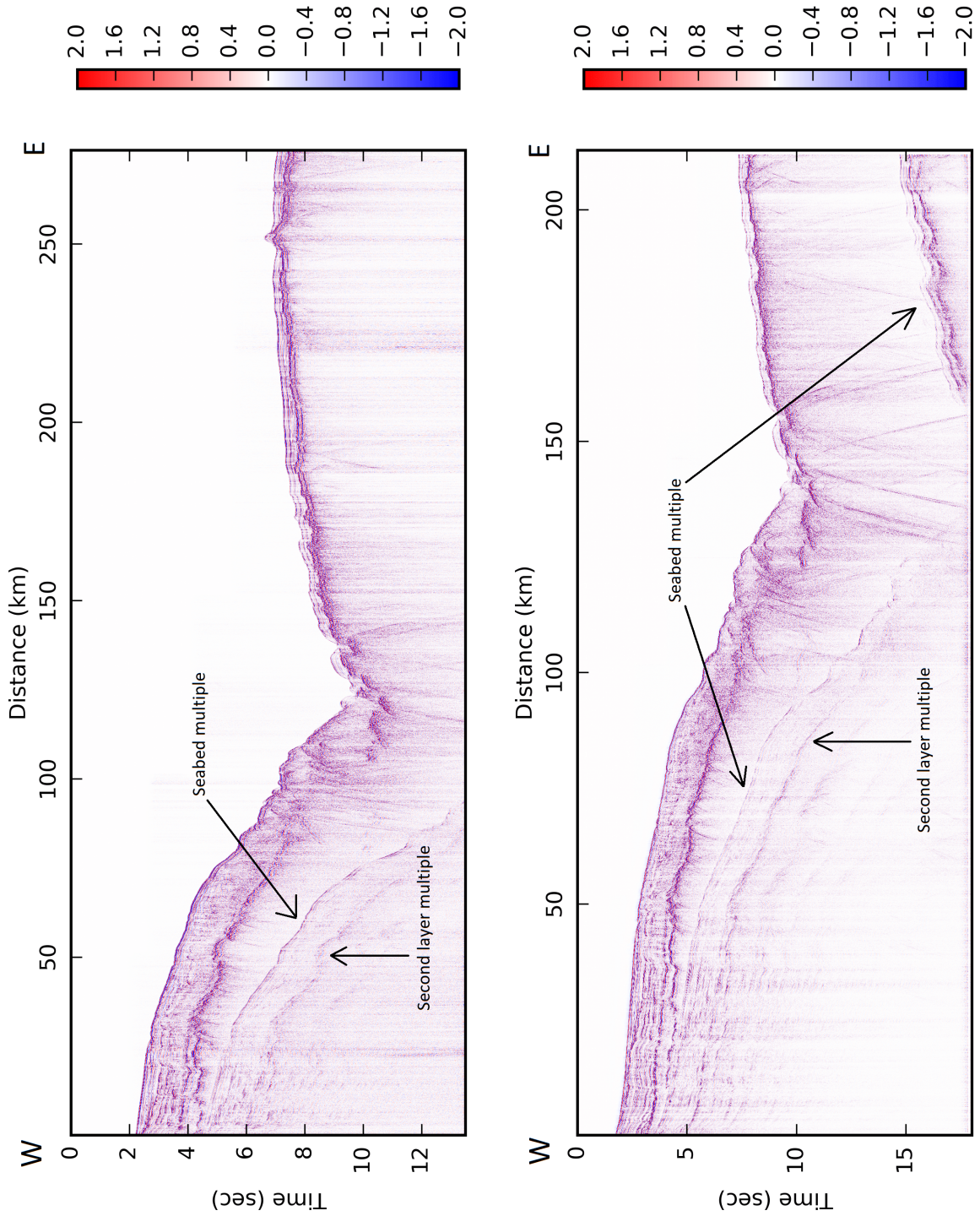
(g) Monitor: Fold reduced NMO corrected gather at L1. (h) Monitor: Fold reduced NMO corrected gather at L2. (i) Monitor: Fold reduced NMO corrected gather at L3.

Figure 6.7: NMO corrected CMP gathers at the three locations. The total TWT has been limited for comparison. The folds from the monitor survey were reduced to 40 as displayed in Figs. 6.7g to 6.7i. The undercorrected reflections (red) are believed to be the multiples in the data while overcorrected event (green) is believed to be a refractive event.



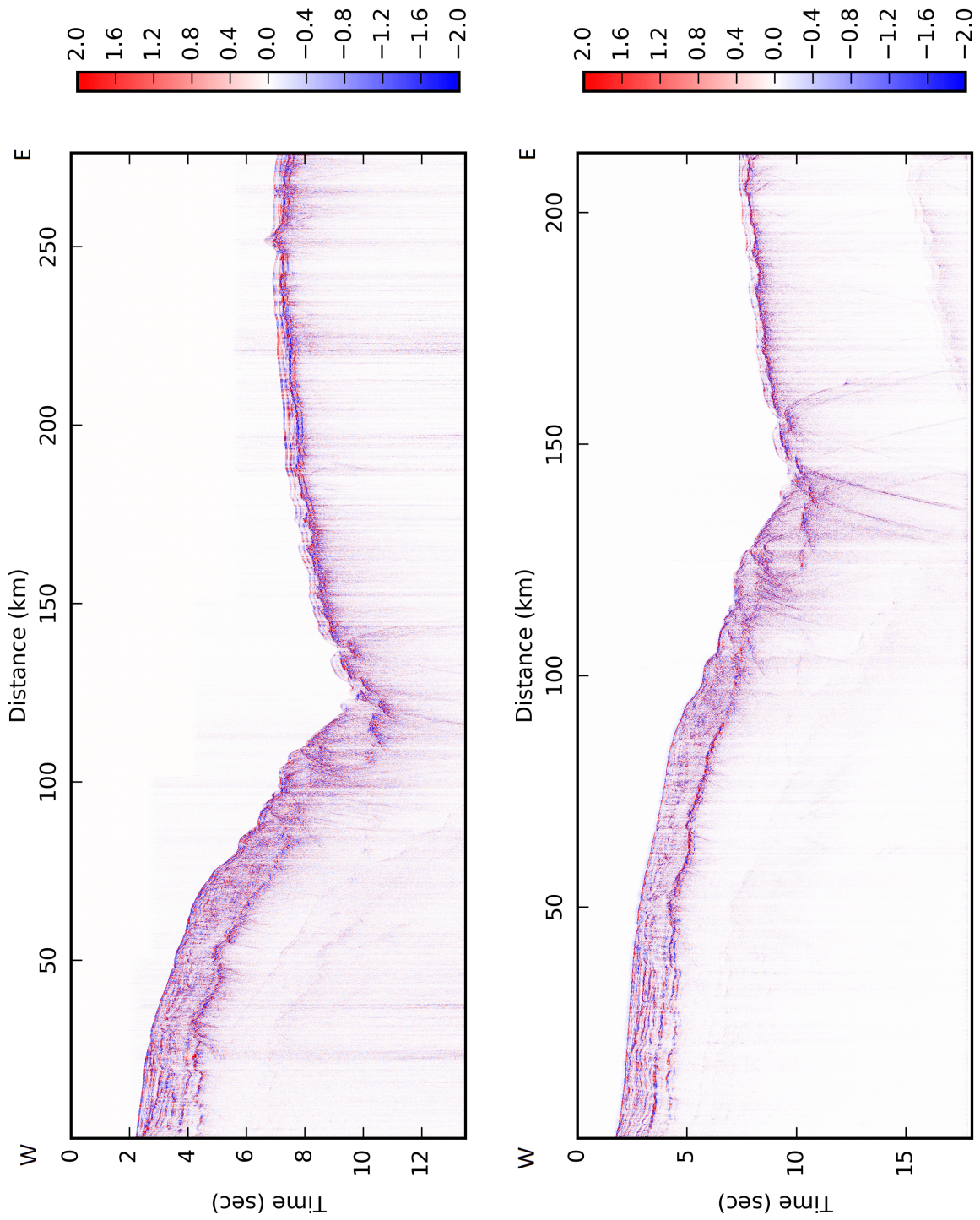
(a) Unmigrated stack of the baseline survey. (b) Unmigrated stack of the monitor survey.

Figure 6.8: Unmigrated stack (brute stack) of the surveys indicating large diffractions and the first observation of the subduction zone and the Japan trench. It can also be observed that the monitor survey is shorter than the baseline survey as expected and with more data acquired towards the West and a TWT up to 18 seconds. The brute stacks are obtained using the unmuted velocity semblance, which gave the velocity models displayed in Figs. 6.6a and 6.6b. Location 1 from the baseline survey (B1) and corresponding monitor survey (M1) are displayed in Fig. 6.1.



(a) Unmigrated stack of the baseline survey. (b) Unmigrated stack of the monitor survey.

Figure 6.9: Unmigrated brute stack with amplitude recovery where the seabed and second layer strong reflection multiples are observed and marked. It can also be observed that there is a continuation of these multiples until the energy is lost at very large depths.



(a) Unmigrated stack of the baseline survey. (b) Unmigrated stack of the monitor survey.

Figure 6.10: Unmigrated stack of the surveys after applying the semblance muted velocity model. The multiples are suppressed, but still visible.

6.2 Pre-stack time migration

The NMO corrected COI gathers were used as a quality control of the migration by observing if the reflectors were horizontally aligned (Fig. 6.11). The COI gathers obtained from the baseline survey had some unusual small overcorrected reflectors observed at shallow depths as displayed in Fig. 6.11a and no over- or undercorrected reflectors at deeper depths of the data (Figs. 6.11b and 6.11c). Considering that this overcorrection did not occur on the majority of the gathers and reflectors at deeper depths, this meant that the migration went as planned with promising results from the quality control. The multiples were still under-corrected as observed for the NMO corrected CMP gathers.

The NMO corrected COI gathers obtained from the monitor survey had some refractional events being over-corrected and similar to the ones obtained from the NMO corrected CMP gathers. This occurred also especially at the shallow depths (Fig. 6.11d). The NMO correction at the other locations were observed as horizontal, and the results of the same obtained procedure of reducing folds and stacking are displayed in Fig. 6.12.

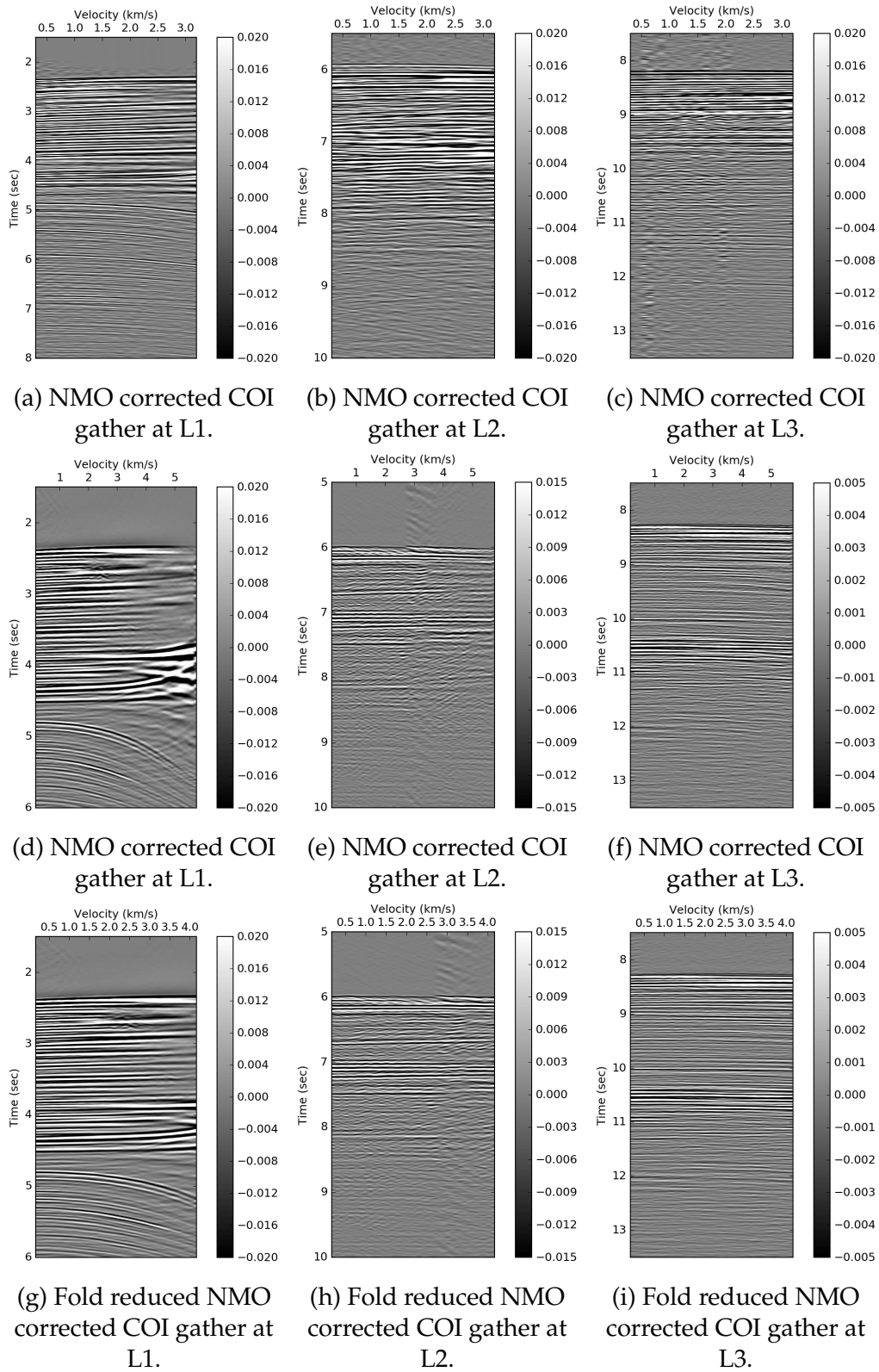
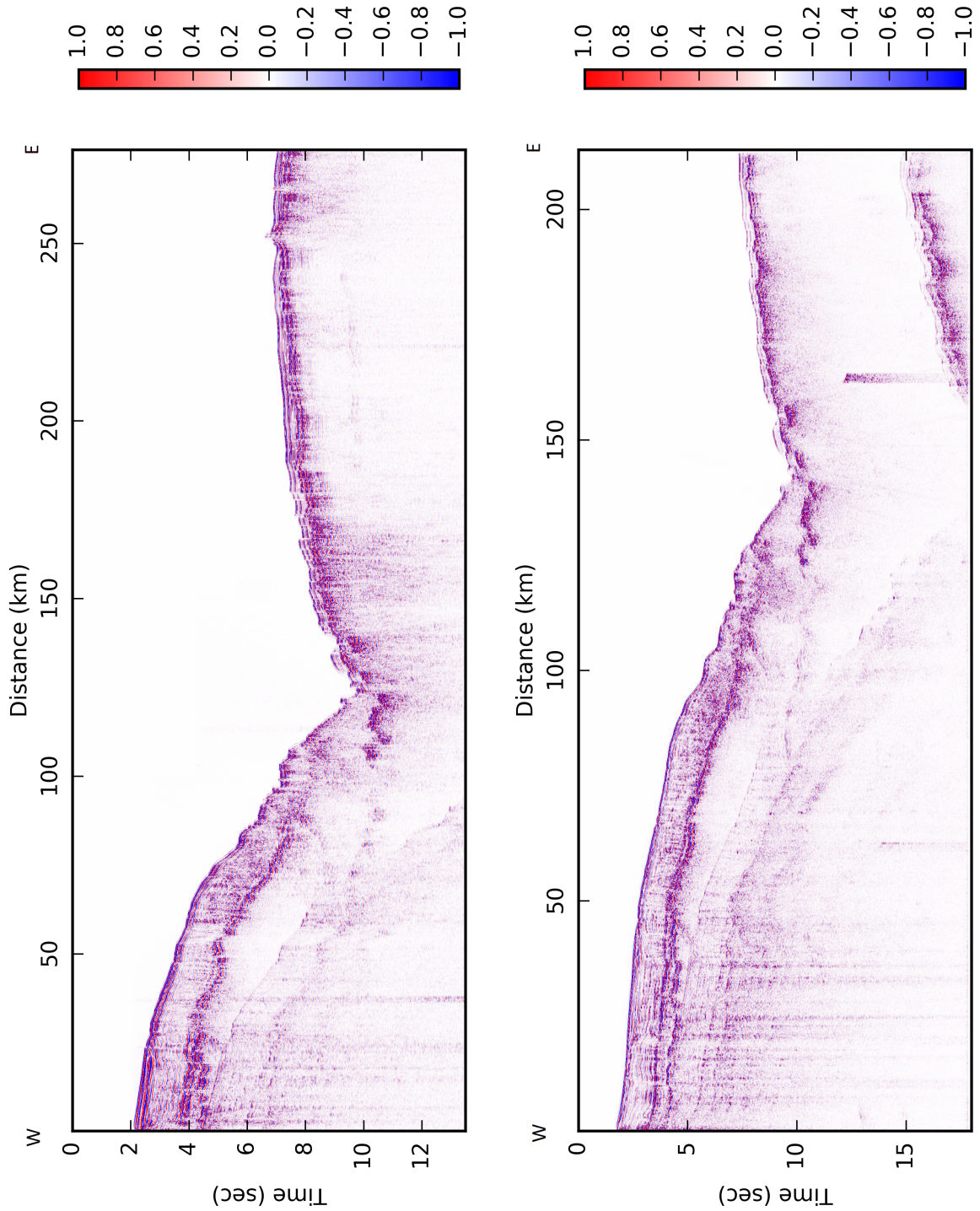


Figure 6.11: NMO corrected COI gathers obtained from the Kirchhoff Pre-stack time migrations. Small overcorrections are observed at shallow depths while refractions are corrected as well for both surveys. These events are also destructive for large offset reflections in the monitor survey, and hence why the folds are reduced. The undercorrected reflections are the multiples in the data.



(a) Time migrated stack of the baseline survey. (b) Time migrated stack of the monitor survey.

Figure 6.12: Time migrated stacks obtained using the semblance muted velocity models. The diffractions are collapsed, and the reflectors moved to their true positions. The migration method assumed only one ray path. Multiples are still weakly present in both surveys.

6.3 Seismic interpretation and observation

Before beginning the seismic interpretation, it was important to observe what kind of polarity the data had. The polarity was unknown, but recognized from the direct wave and the first reflection of the seabed. Both surveys were observed to have a normal polarity as illustrated in Fig. 6.13, which is always important for the interpreter to know (Fig. 6.3). The data were believed to be using SEG polarity, which means that a positive amplitude (peak) denotes the acoustic impedance increase when using a ricker wavelet.

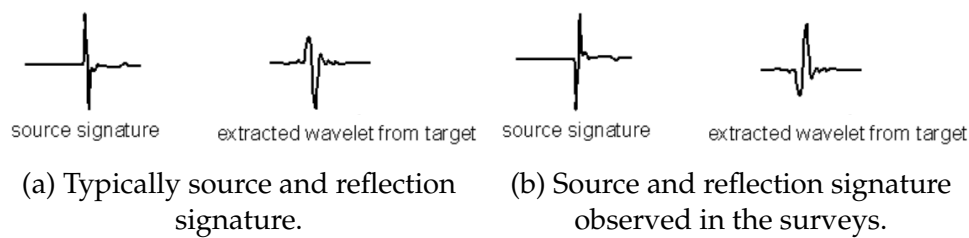


Figure 6.13: Polarity of the seismic wavelet.

Interpreting horizons on a stack may be insufficient due to non-collapsed diffractions and possible scenarios of faults present. Hence, all interpretation was done on the migrated stacks. Before interpreting the monitor survey, the tectonic structures and layers were interpreted and characterized on the baseline survey. Many strong and continues reflections were observed at the Pacific Plate close to the seabed, and where horst and graben structures were developed along with normal faulting (Fig. 6.14). The topmost layers of the Pacific Plate were most likely soft recent marine sediments, which were loosely attached to the plate and scraped when reaching the trench. Close to the trench, possible contourite with contourite channels on the right side of the East on the Pacific Plate was indicated in Fig. 6.14.

The stratified layers on the continental plate were visible on the landward side, and where the strongest reflector was the seabed. As the layers came closer to the trench, the amplitudes were observed as unclear and contained a chaotic pattern, which was most likely due to the strong deformation. A horst structure was also interpreted on the Okhotsk Plate where the erosional unconformity marked the top of Cretaceous in (Fig. 6.14). Certain reflection pattern on this plate close to the trench indicated fold planes and thrust complex, which are typically events often observed in a subduction zone.

A pattern of short and weak amplitudes were observed below Oceanic layer 3 and believed to be the Moho discontinuity, which is the boundary between the oceanic crust and upper mantle. This reflector disappeared as it approached the trench. Another interesting observation was below the deformation zone where a pattern of weak reflectors were located. It could be discussed whether these belonged to the pacific plate subducting below the Okhotsk Plate, which it was most likely, but however with a unusual dip upward, and hard to observe.

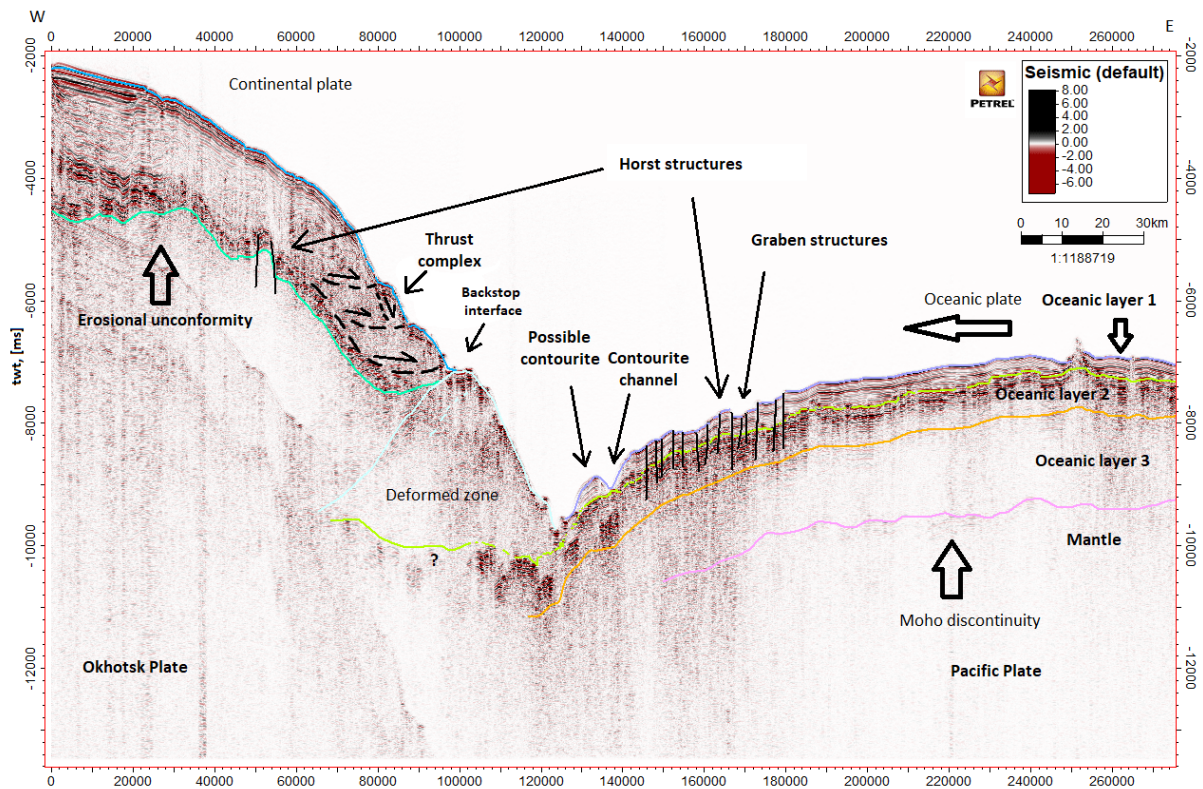


Figure 6.14: Seismic interpretation of various layers and faults on the time migrated baseline survey. The stack is ten time vertically exaggerated. Strong continuous reflections was observed at the Pacific Plate with horst and graben structures along a series of normal faulting. Contourite and contourite channels were also interpreted close to the trench where the uppermost oceanic marine sediments were believed to be scraped as it closes the trench. The Pacific Plate was observed to subduct beneath the Okhotsk Plate with possible interaction with the Okhotsk Plate in an up-dip manner (marked by light green polygon and the question mark). The Japan Trench is observed at approximately 9.8-10 s.

6.3.1 Time-lapse interpretation

Concerning the changes observed on the monitor survey, using Petrel as an interpretation software was a great advantage for allowing the same observation be compared to the monitor survey. By performing the shift explained in Chapter 5.9, the time migrated stacks were compared on similar locations and matched with the survey lengths. Matched time migrated stacks of the surveys are hence displayed in Fig. 6.15 where the irrelevant parts not covering both surveys were removed. A direct scale was difficult to observe and smaller sections were marked in the figures to observe the differences. However, it could be said that the most distinguishable differences observed were the change from continuous reflectors to a more chaotic pattern through some of the different layers when approaching the trench.

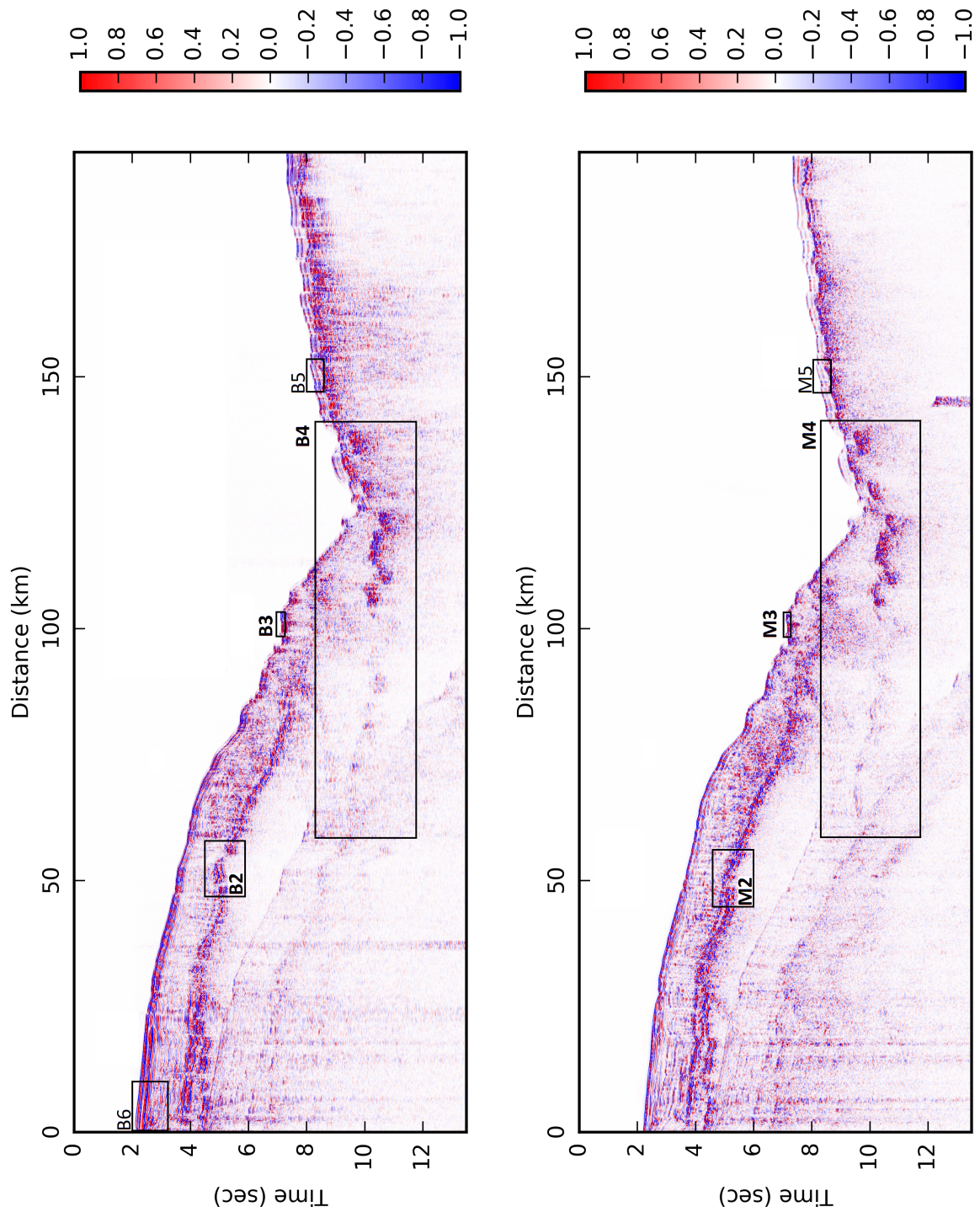
One of the biggest observation was located at the continental shelf where the horst structure was previously interpreted (Fig. 6.16). This horst structure was almost completely changed on the monitor survey where two new faults were believed to be present and marked by the red polygons in Fig. 6.16 together with the new unconformity-pattern. The reflectors changed to a certain degree where it was hardly possible to observe where the unconformity continued on the west side of the structure.

A closer look and more detailed comparison on a smaller scale was interpreted near the trench above the deformation zone. Here at the backstop interface, an uplift of approximately 16 ms (TWT) was revealed (Fig. 6.17). Considering an average water velocity of 1480 m/s, which was used during the processing, this corresponded to an uplift of 11.84 m caused by the earthquake.

An observation made regarding the upward trend of the subduction zone below the continental plate was supported by a better and more distinguish reflector-pattern on the monitor survey (Fig. 6.17). By recalling the interpretation from previous sub-chapter, it was observed that the top of the oceanic crust was imaged with more visible reflectors in the monitor survey. However, it was difficult to detect changes and the most observable changes were the chaotic change of amplitudes as mentioned earlier.

The location marked on the east of the trench in Fig. 6.15 and displayed in in Fig. 6.19 compares the subsidence that were observed between the surveys. Approximately 8ms subsidence was found, which corresponded to 5.92 m. The fault lines in the figures are not compared, but it could be observed that a horizontal displacement could also be present and possibly caused by the earthquake. However, the horizontal displacement was not measured to due to the significant errors that could be caused by the navigational shift made.

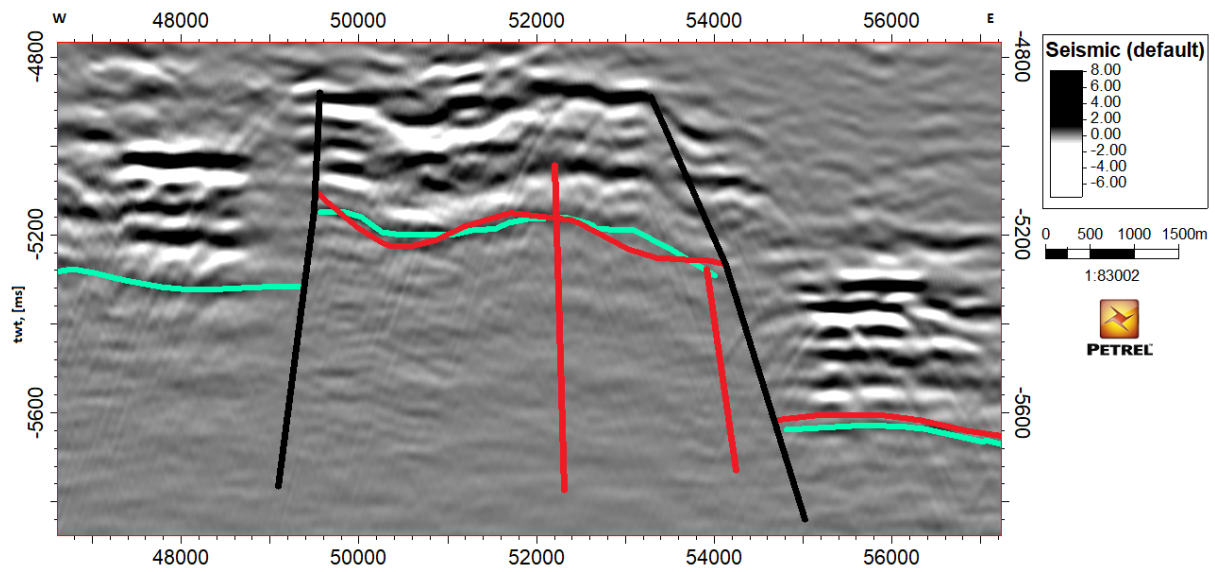
The obtained velocity models were also shorted and compared in Fig. 6.20 where significant differences were observed. The trend was a velocity reduction after the earthquake, especially close to the trench from west (deformation zone) and also towards the east parts. The changes in velocities might have also caused the Moho discontinuity reflectors to no longer be visible on the monitor survey.



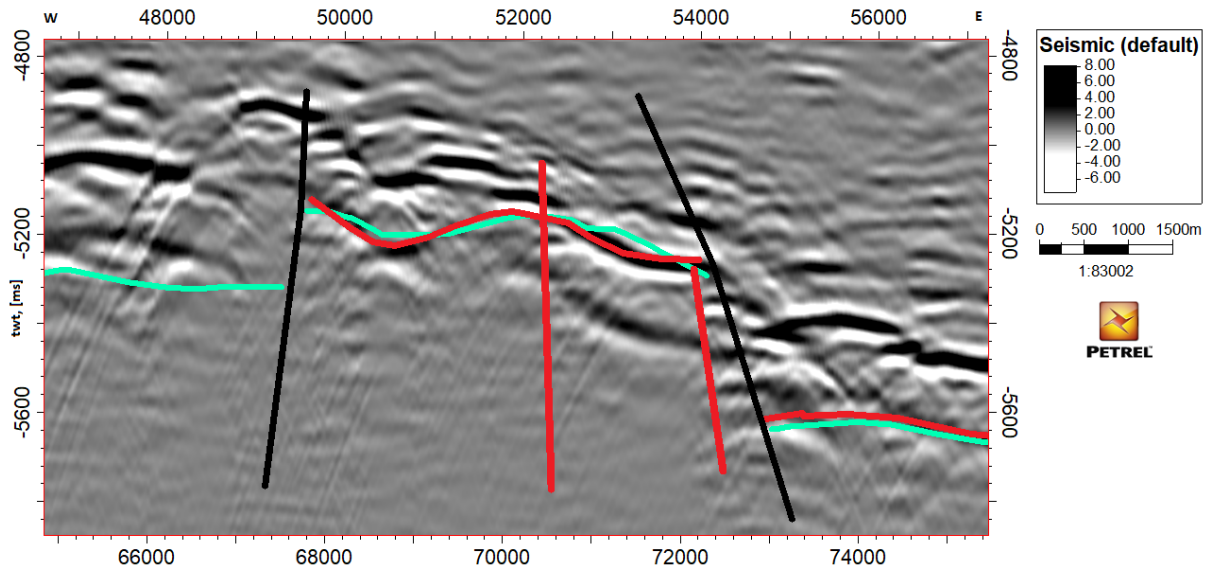
(a) Reduced time migrated stack of the baseline survey.

(b) Reduced time migrated stack of the monitor survey.

Figure 6.15: Reduced time migrated stack of the baseline and monitor survey. Irrelevant parts of both surveys are removed to make them comparable.

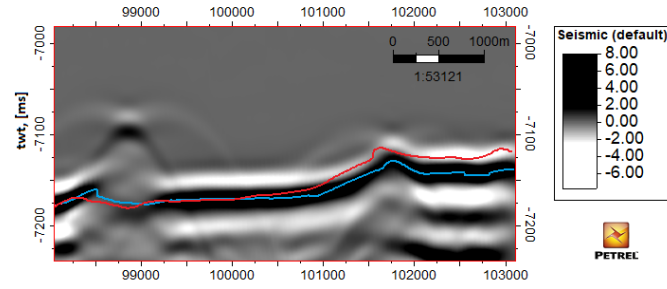


(a) Horst structure observed on the baseline survey.

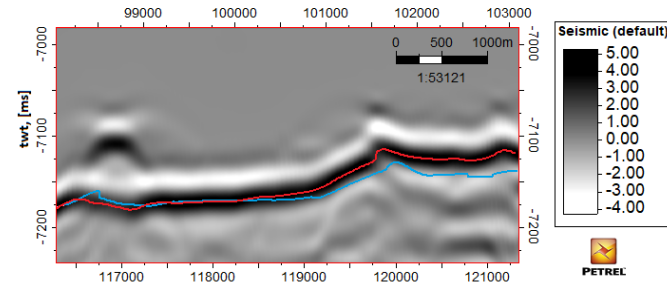


(b) Horst structure observed on the monitor survey.

Figure 6.16: Time-lapse observation of the horst structure. The red polygons illustrate the interpreted horizon and faults on the monitor survey while the green polygons are from the baseline survey. The changes in amplitudes on the monitor survey made it difficult to observe the continuation of the reflector on the left side of the horst structure. As drawn, two new faults were observed to be present in the monitor survey. For location, see B2 and M2 in Fig. 6.15.

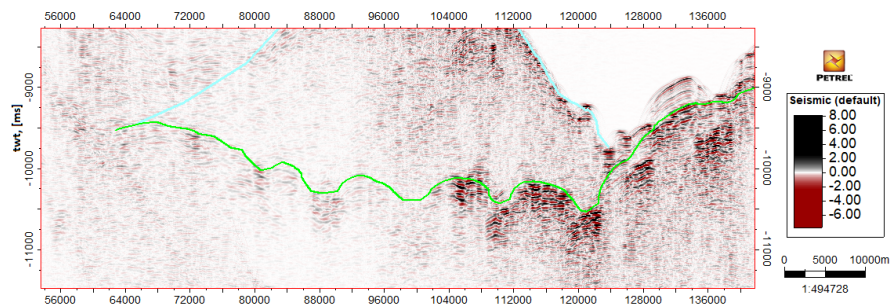


(a) Seabed of the baseline survey.

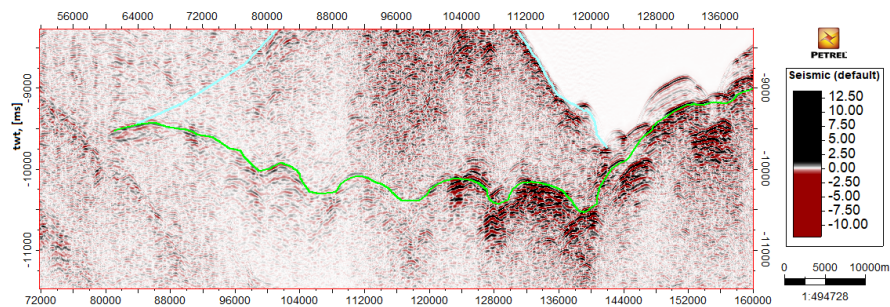


(b) seabed of the monitor survey.

Figure 6.17: Time-lapse comparison of the seabed changes on the backstop interface. An uplift of 16ms was observed at highest. For location, see B3 and M3 in Fig. 6.15.

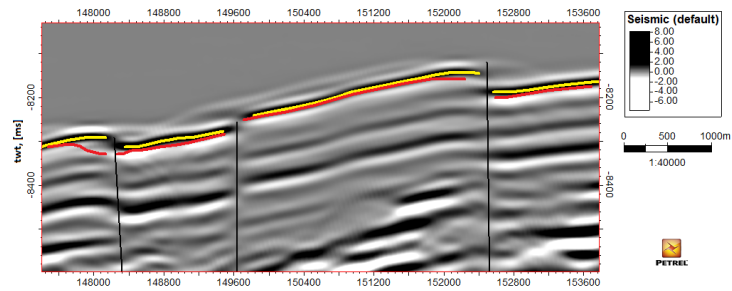


(a) Seabed of the baseline survey.

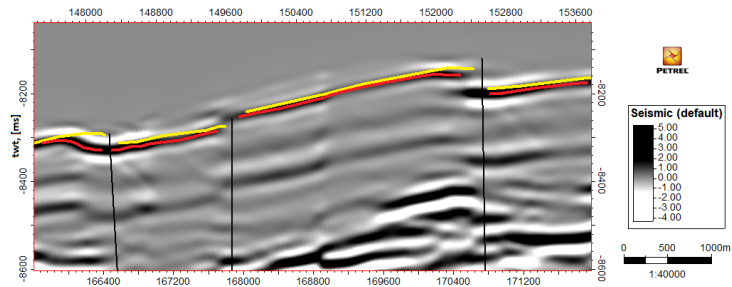


(b) seabed of the monitor survey.

Figure 6.18: Time-lapse comparison of the subduction zone near the trench. Only polygons interpreted at the monitor survey are displayed on the baseline survey, since differences were difficult to observe. The top of the Oceanic plate was be observed by some continuous reflectors subducting below the Okhotsk Plate. For location, see B4 and M4 in Fig. 6.15.

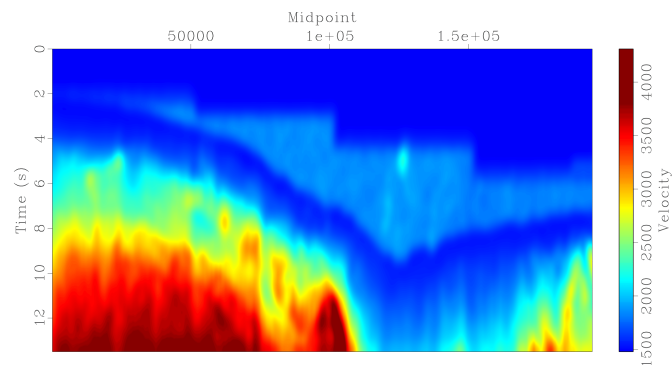


(a) Seabed of the baseline survey.

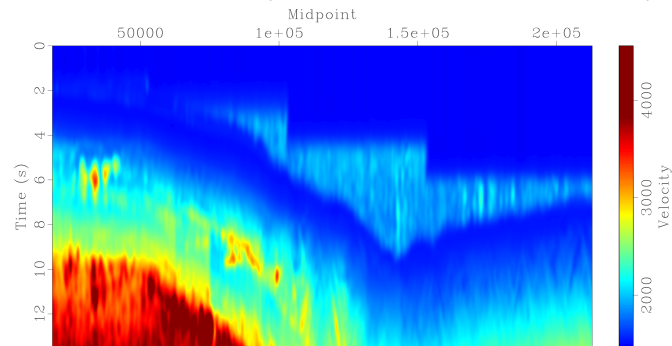


(b) seabed of the monitor survey.

Figure 6.19: Time-lapse comparison of the seabed changes on the Oceanic Plate close to the trench. A subsidence of approximately average of 8ms was observed. For location, see B5 and M5 in Fig. 6.15.



(a) Reduced velocity model of the baseline survey.



(b) Reduced stack of the monitor survey.

Figure 6.20: Reduced velocity model for comparing. Large velocity changes are observed where velocity reduction is observed near the trench and across the Oceanic Moho interface.

6.4 Pre-stack depth migration

The results from the depth migration were highly dependent on a proper and correct picked velocity model. The Dix velocity models displayed in Fig. 6.21 were obtained by smoothing the velocities to avoid wrong velocity variations to be present, which were initially caused by the automatic picked velocities. The depth velocity models displayed in Fig. 6.22 were also smoothed to remove some of the similar problems. Hence, the final depth velocity models obtained for the depth migration are displayed in Fig. 6.23. The velocities were only converted to a depth of 12 km, which was found to be an underestimation considering the actual acquired length of the survey in z-axis. This resulted in some limited information provided from the migration as well.

It was clearly observed that the interval velocities increased to approximately 6000 - 8000 m/s at large depths. However, the velocities dropped down to 2000 m/s on the deepest parts of the oceanic plate on the baseline velocity model. This was most likely wrong and caused by wrong velocities in the initial velocity model to be present these depths. The monitor survey did not contain the similar velocity drop at the same place, but observed on the continental plate. Hence, this marked the velocity models for the migration as very unstable, which gave significant differences and *errors* in the migration.

The obtained depth migrated stacks are displayed in Fig. 6.24 where the vertical depth variations were observed through the various layers. Here, the seabed was detected as trough, which meant that the polarity was SEG reverse. The Japan Trench was located at approximately 8600 meters below sea level in these depth migrated stacks. There were however limited options to check whether the experimental depth migration went as planned and one method was profound to be used. These migrated stacks were converted back to time and compared to the time migrated stacks to observe differences across the layers (Fig. 6.25). Hence, these were independently studied to reveal the differences in the migration and not compared.

Beside the obvious cause of an unstable depth migration, the stacks were observed to resolve some issues related to the Kirchhoff time migration. By comparing shallow depths between the time migrated, depth migrated and the time converted stack obtained from converting the depth migration stack (hereby called the Time Quality Control stack (TQC)), the resolution was observed to increase on the stacks (Figs. 6.26 and 6.27). The depth and TQC migrated sections displayed in these figures showed a clear boundary between the onlap layers towards the boundary sequence. This was however difficult to observe on the Kirchhoff time migrated section. The seabed was mapped on the time migrated section and displayed on the TQC section to illustrate the errors in the migration, independently on the baseline and monitor survey.

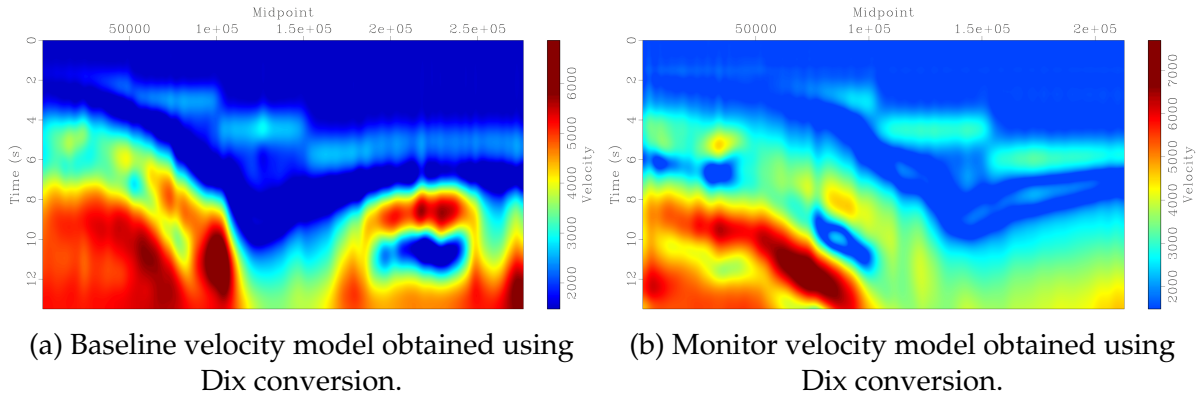


Figure 6.21: Velocity models obtained from Dix conversion. The Dix conversion converted the velocities to interval velocities where it can be clearly observed that there are some low velocities present in between layer where it should theoretically increase, and an overestimation of high velocities near the trench observed in layers on the continental plate near close to the trench.

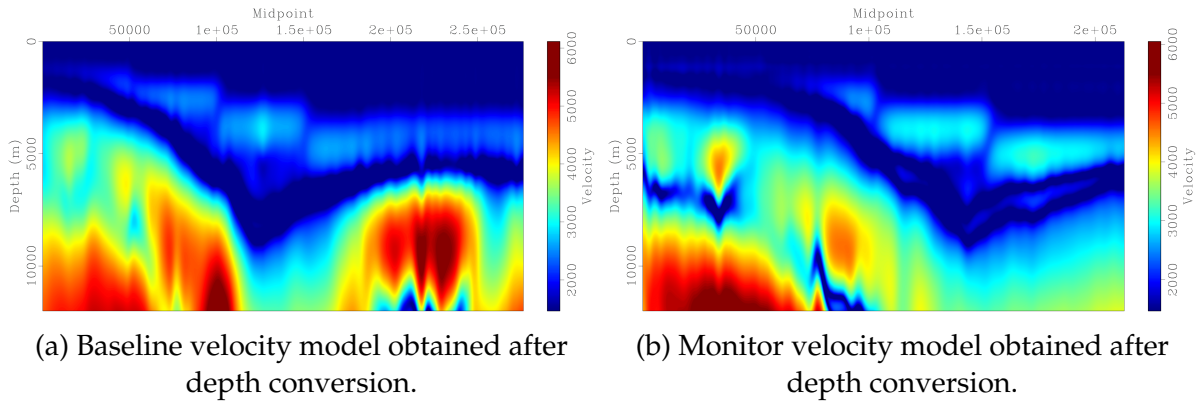


Figure 6.22: Velocity models obtained from the depth conversion. These have also been smoothed to avoid the low velocities at high depths. Low velocities at deep depths are still visible in the baseline and not the monitor velocity depth model.

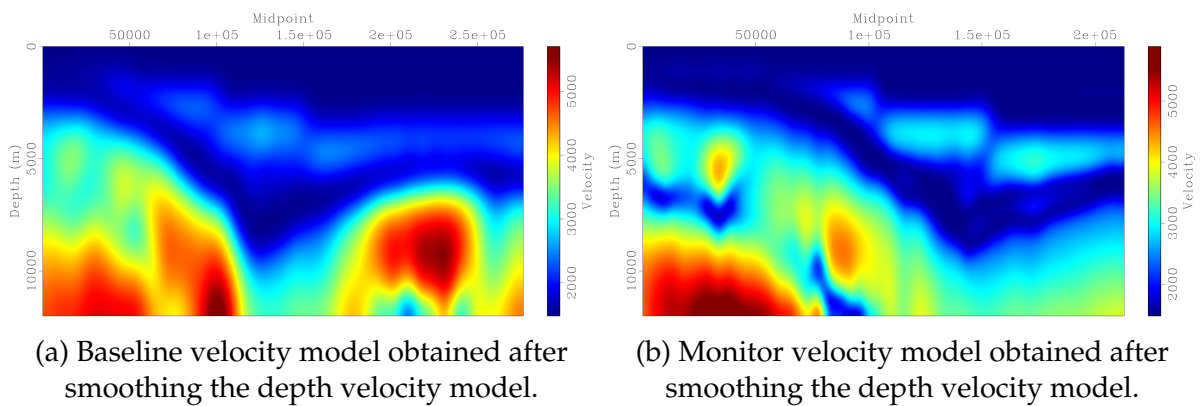


Figure 6.23: Smoothed velocity model obtained from the depth conversion. These are also smoothed to eliminate low velocities at large depth, but these are however still present in the model.

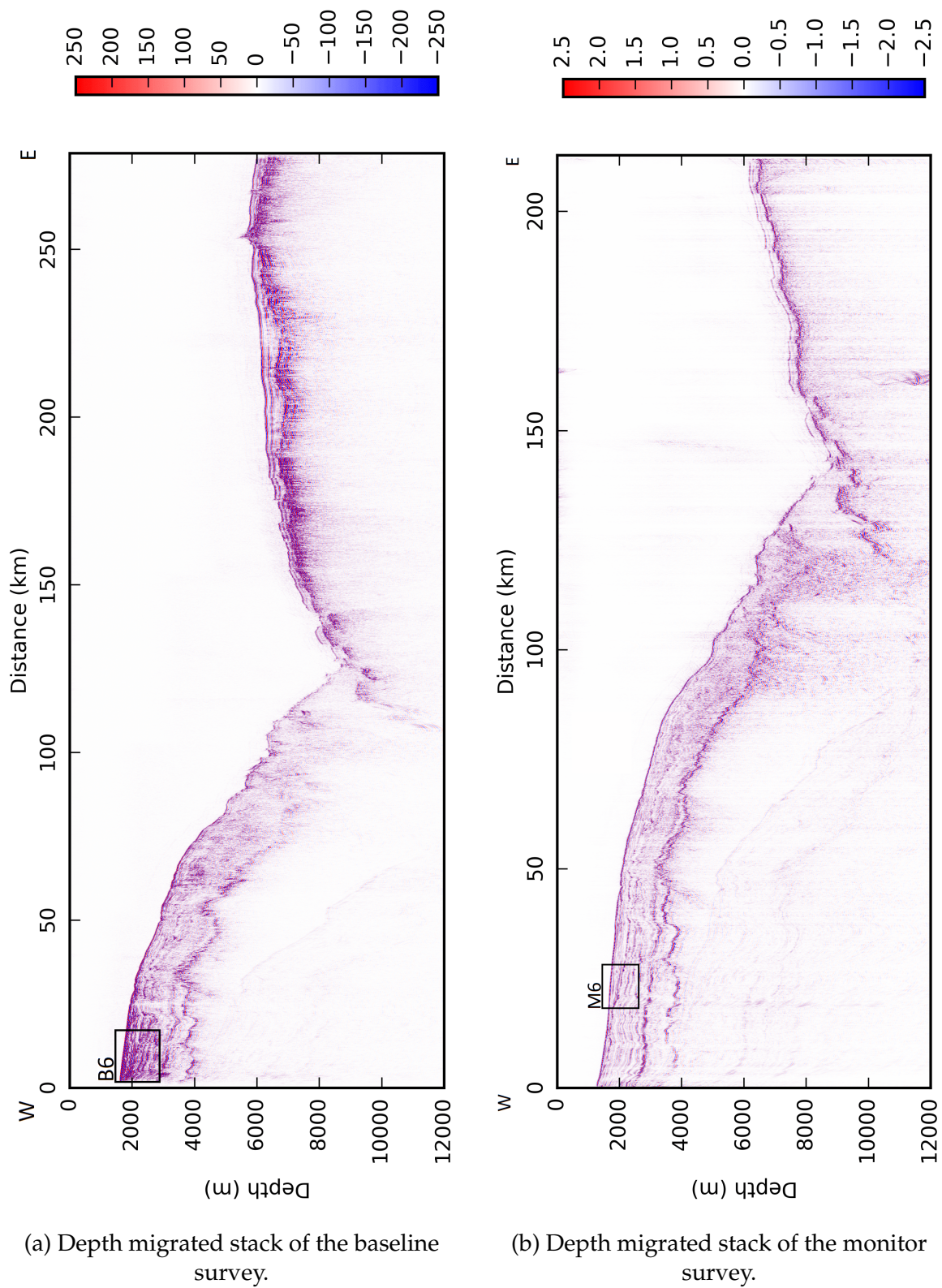
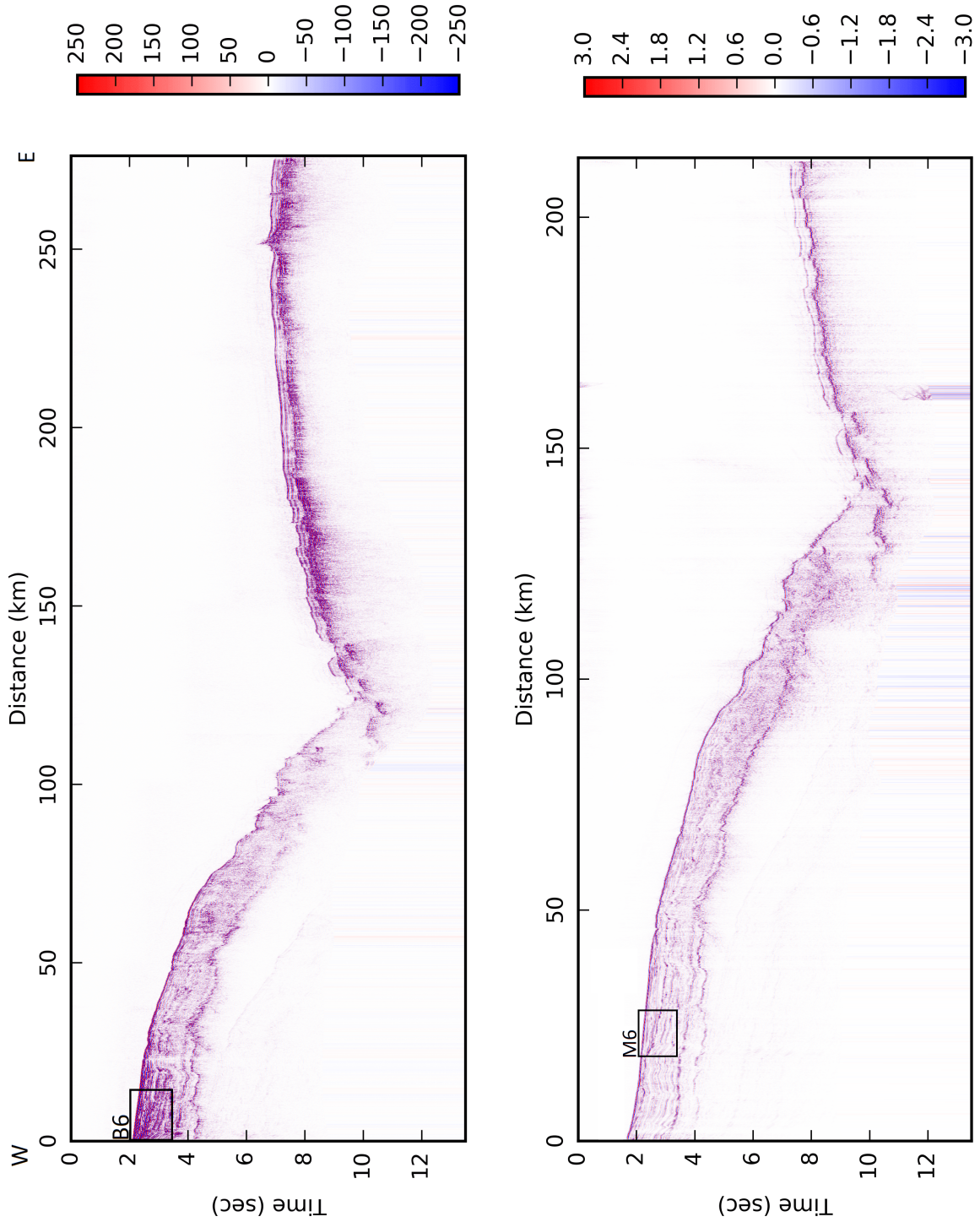


Figure 6.24: Depth migrated stacks obtained by using the smoothed depth velocity models. The migration is very sensitive to the velocity changed, especially observed on the Oceanic Plate in the monitor survey, and which gave the unstable migration. The seabed in both surveys revealed to be SEG reverse polarities.



(a) TQC stack from the baseline depth migration.

(b) TQC stack from the monitor depth migration.

Figure 6.25: TQC stacks obtained from converting the depth migrated stack to time using the smoothed depth velocity model. The program *sfdepth2time* gave artificial noise at large depths that eliminates the reflectors, and assumed to be due to underestimation of the depths. The polarity in the data were revealed to be SEG negative.

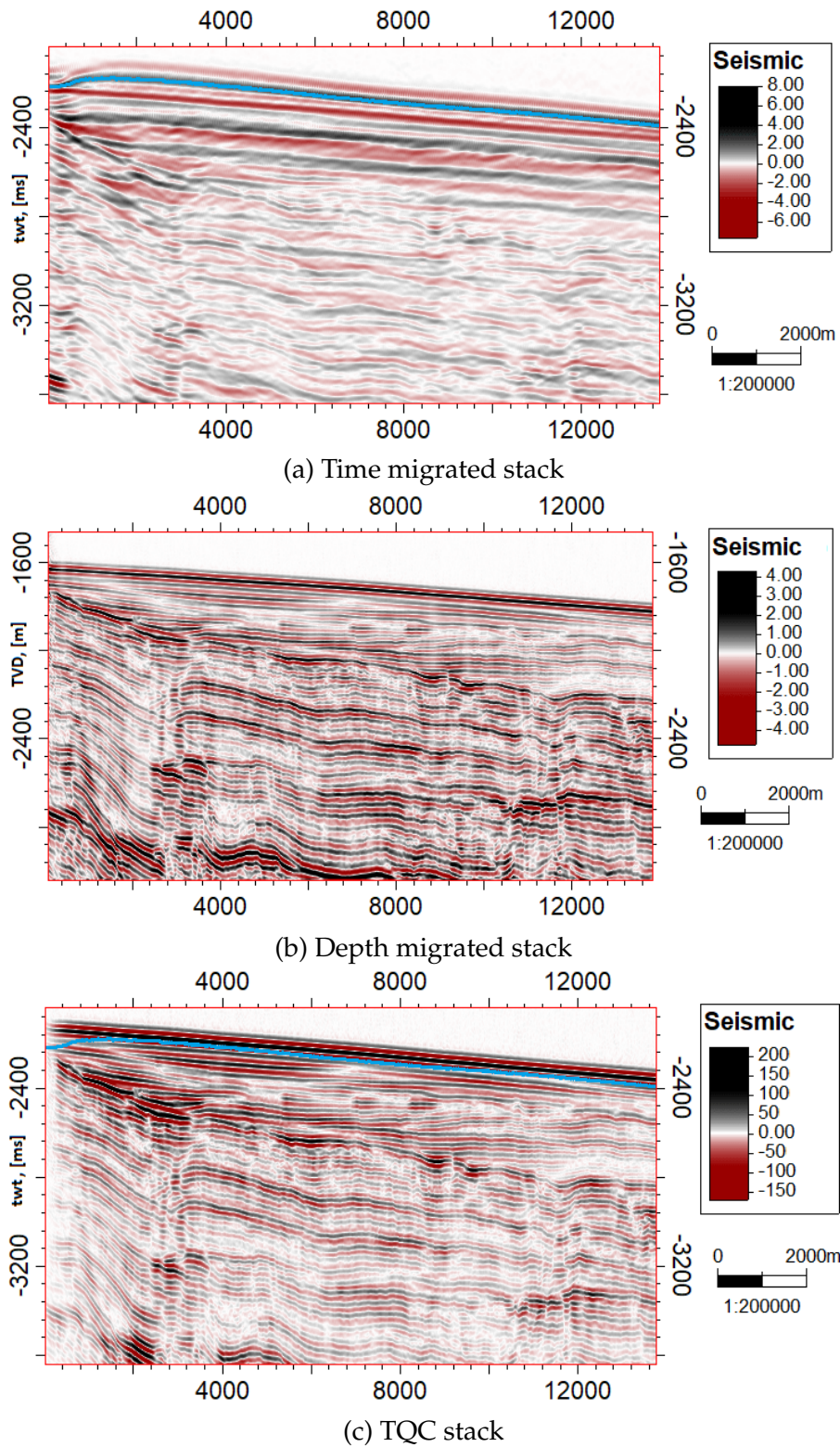


Figure 6.26: Comparison of shallow sections from the baseline time migrated, depth migrated and TQC stacks. The seabed (blue polygon) was mapped on the time migrated stack and displayed on the TQC stack to observe the differences and errors in the migration. However, it could be clearly observed that both depth and TQC stacks were beneficial to image the shallow depths where onlap reflectors are observed toward the sequence boundary. Beware that SEG positive polarity is used in Fig. 6.26a while SEG negative is used in Figs. 6.26b and 6.26c. For location, see B6 on Figs. 6.24 and 6.25.

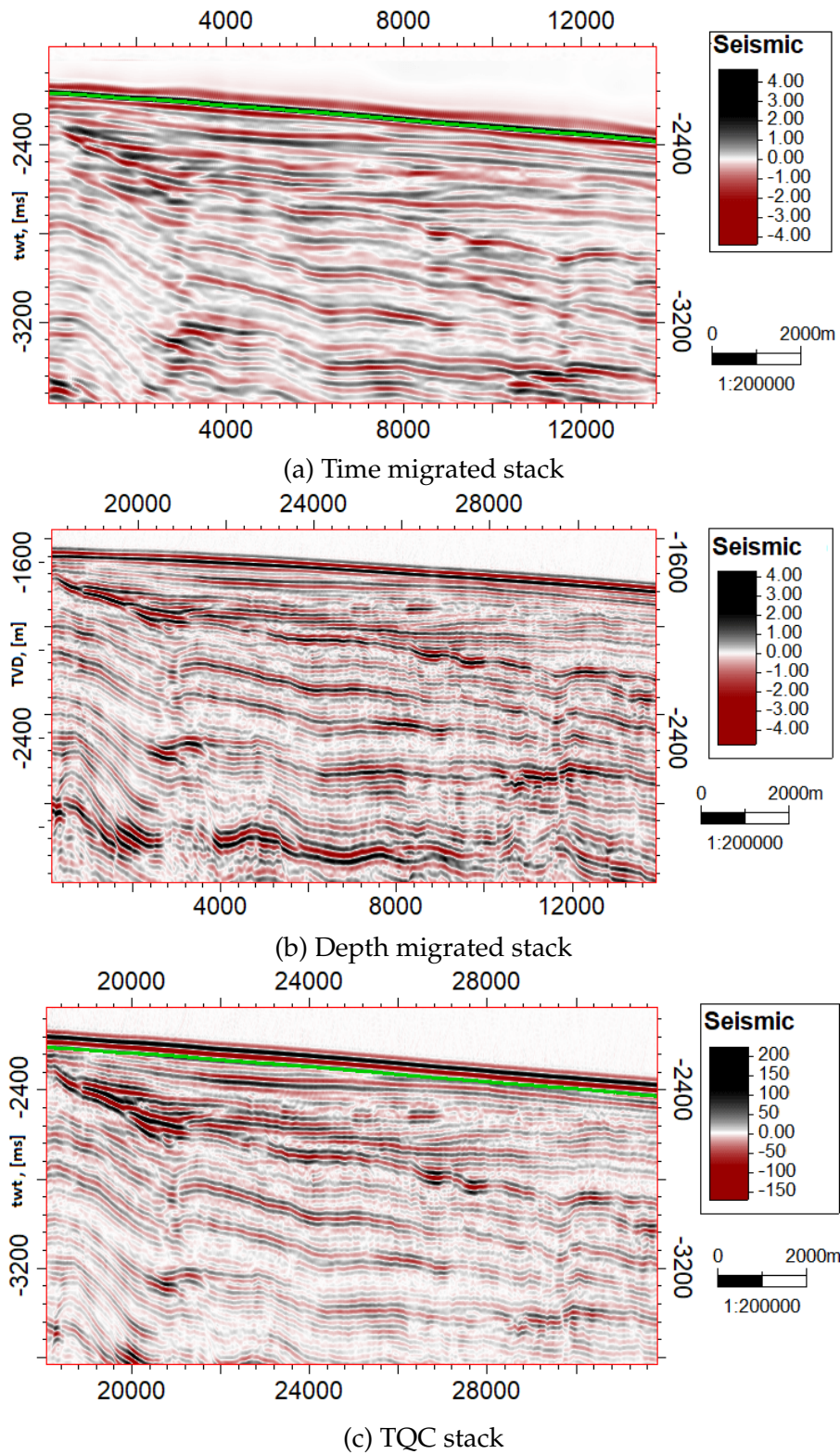


Figure 6.27: Comparison of shallow sections obtained from the monitor time migrated, depth migrated and TQC stack. The seabed (green polygon) was mapped on the time migrated stack and displayed on the TQC stack to observe the differences and errors in the migration. However, it could be clearly observed that both depth and TQC stacks were also beneficial to image the shallow depths where onlap reflectors are observed toward the sequence boundary. Beware that SEG positive polarity is used in Fig. 6.27a while SEG negative is used in Figs. 6.27b and 6.27c. For location, see M6 on Figs. 6.24 and 6.25.

7 | Discussion

The baseline survey was unexpectedly provided with wrong nominal coordinates prior to the processing while the monitor survey (Figs. 5.1 and 5.2) had the actual recorded source and receiver coordinates. Here, it was clearly observed that the monitor survey must have experienced a cable curvature during the acquisition, which is a real life problem during seismic acquisition in general. The monitor survey was observed to have a maximum offset deviation up to 1.5 km of the receiver coordinates (Fig. 5.2b). This might indicate that there must have been a strong water current/tide during the acquisition, since it was spread out in both directions (negative and positive y-axis).

The modified Shepards method combined with the differential NMO function were believed to fix the major issue concerning the 2D survey geometry. This method of interpolating the coordinates to a pre-defined datum plan was successfully obtained where the surveys were also transformed over to a 3D geometry. The only limitation observed was that the interpolation was performed from coordinates (0,0) to (0,X), and why the survey coordinates were required to be shifted prior to the interpolation.

As the surveys were resampled to 2 ms, they were also band-pass filtered and despiked in the shot domain. These three processing steps were crucial steps that drastically increased the SN-ratio. However, concerning the band-pass filter created, this was performed with a very high cut-off value of 50 Hz compared to the fact that the monitor survey had a receiver notch at 33.71 Hz. Lowering the high cut-off values below 50 Hz would theoretically result in loss of information provided at shallow depths in the baseline survey, which was not desirable. The band-pass filter still performed as expected where low and high frequency anomalies were removed in both surveys (Fig. 6.2).

The ghost reflector in both surveys appeared as typical effect with opposite amplitudes observed at the direct waves, which is explained by negative reflection coefficient at water-air interface (Fig. 5.5). The direct wave observed at small offsets was hence used to create the debubble filter, which gave an increased PB-ratio of $\approx 157\%$ in the baseline survey and unfortunately an PB-ratio decrease of $\approx 15.8\%$ in the monitor survey. However, these calculations did not represent all traces and only defined ratios for one singular trace at small offset. To find the survey PB-ratio, an average calculation of all traces would be needed. The debubble filter showed also to increase amplitudes at large offset and deep depth reflectors for both surveys (Fig. 5.7), which was believed to be beneficial to image deeper reflections in the surveys.

In papers presented by Tsuru et al. (2000, 2002), the authors described that bubble oscillation still appeared at the baseline stack even after applying deconvolution. The debubble filter presented in with Madagascar hence showed the significant improvement and great advantage of this filter in Madagascar where the bubble oscillations were removed. There was unfortunately no information provided in paper by Boston et al. (2014) and Kodaira et al. (2017), but observation from Kwok et al. (2017) showed that the bubble oscillation is removed (Appendix B, Fig. B.1). However, the first two mentioned papers did state that they also performed a wavelet conversion and predictive deconvolution.

The muting algorithm used in this processing sequence was not sufficient as noises still were present in both surveys. This was considered a time vs. benefit process and not of great importance, and done with a step-wise method. However, a direct consequence of this was that the automatic picking algorithm picked *artificial* velocities in the water layer. Even though this was partially fixed by separating the data prior to the velocity analysis, the noises were picked and present in the velocity model. The velocities in the water layer should not theoretically effect the stacking and migration, However, converting the velocities using *sfdix* was consequently disrupted by these velocities, and contributed negatively towards the depth velocity model. This was possibly due to *dix* velocities at given depth n was consequently based on the previous velocity at depth $n-1$ in the calculation (Eq. 3.11).

The velocity semblances did not generally reveal great differences between velocities in water at the first layer. This might be due to underestimation of velocities, but provided sufficient NMO correction when using the smoothed velocity models (Fig. 6.6). However, it was observed a strong semblance amplitude spread around 2.2 s (see Fig. 5.11e) where the amplitudes are spread and could explain the reason for small undercorrection at shallow depths as displayed in Fig. 6.7d. This could mean that the first picked velocity should be lower than 1480 m/s to make the seabed reflector horizontal according to theory about NMO correction (Fig. 3.11). It can be discussed how much lower this would be, but a major uncertainty in 4D processing is the velocity variations in the water column. This undercorrection could also be caused by the smoothing of the velocity model as the velocity-picked anomalies are just above the seabed reflector.

Obtaining a satisfying and correct velocity model was difficult for both surveys when Madagascar only provided an automatic picking method. The semblance muting was done to meet some demands for the velocity model, i.e. velocities should increase with depth, and in order to suppress the multiples. This particular method was found useful from tutorials by Madagascar Development Team (2018) and adequately adapted here. The velocity model was far from a realistic model to obtain for these surveys, and only realistic and presentable for the reflectors from seabed down to top of basement reflector. The velocity semblance scan calculated velocities up to 5230 m/s where it could be observed that velocities up to 7-8000 m/s was present. Comparing the trend of the velocity increase with depth, the velocity model should have velocities increasing in similar manner schematically displayed in Fig. 7.1 with velocities up to 8000 m/s. The realistic model from Jamstec (2015) illustrates the (interval) velocity increase across different layers in both Okhotsk and Oceanic plates.

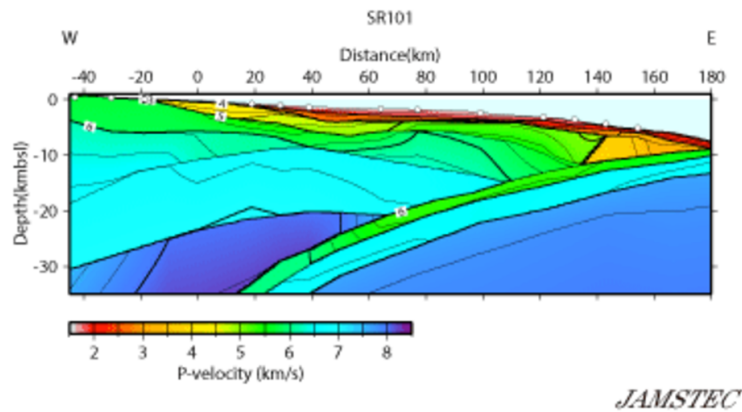


Figure 7.1: A schematic illustration of the depth velocity model in the baseline survey. Figure from Jamstec (2015).

The NMO corrections at deep depths were very small and smoothing the velocities too much would theoretically be noticeable on large offset traces, and result in lower stacking amplitudes of each event. Since stacking was done with full offsets (except for the monitor survey), it was believed that this had minimal effects on the stacking. Removing far offset traces on the monitor survey after NMO correction was found to be the only solution to overcome the overcorrected refractions disturbing reflectors at shallow event. This was also done to avoid a drastic decrease in amplitudes and blurry images. The reduction of folds in this survey could also be the reason for less visible reflectors at large depths (for example the Moho discontinuity) as the removed traces could have contributed positively to the stacking amplitude.

The only method chosen to perform multiple suppression/attenuation was through the muting of velocity semblances to undercorrect the multiples. Performing filters such as F-K and radon-filters were possible for multiple suppression, but required the correct parameters, which were difficult for these surveys and therefore not used. Hence, the aim of these filters are not to remove the primaries. They *might* also be difficult to perform without the proper velocity models.

The CMP gathers contained a number of bad traces (spikes) which were not suppressed by the despiking algorithm. The despiking algorithm worked simply by comparing the trace to despike with neighbouring traces and minimize the differences. This would mean that applying a large value *wide2* would disrupt the reflector, especially in the gathers with no NMO correction. Despiking in NMO corrected gather could possibly be more beneficial for increasing the SN ratio for stacking. Bad traces would in this scenario of stacking contribute with less destruction of other traces, if the traces are despiked in NMO corrected gathers. However, this is not a common way to despiking the data.

The benefit of Kirchhoff pre-stack time migration in Madagascar was first of all the COI gathers. This method allowed the user to compare the outcome of the migration by observing the COI gathers to check whether they are horizontal or not. It was revealed that both surveys contained small overcorrection at the shallow depths that

could be possibly caused by smoothing the velocities too much. The final time migrated stacks were also initially assumed to have collapsed all diffractions, but by observing Fig. 6.16 in black-white color scheme revealed that some diffractions were still present. This could mean that the selected aperture length were too small compared to what is required to collapse these. However, the faults presented in Fig. 6.19 revealed that the diffractions were collapsed at very large depths.

The geological observations in the baseline survey are similar with the research done by Tsuru et al. (2000, 2002) in addition to the small possible horst structure present on the west parts of the subduction zone (Fig. 6.19). The time-lapse changes observed on this structure are too significant to be realistic, and could be caused by errors in the processing. To verify the changes on the horst structure, one would need to run the migration with the baseline velocity model and detect changes as well.

The findings of uplift movements on the Okhotsk Plate of approximately 11.84 m matched research done in nearby areas by Fujii et al. (2011) and Sun et al. (2017) along with subsidence of 5.92 m on the Oceanic Plate. However, the numbers presented were very varying and affected by the navigational shift. Concerning the effect of the earthquake, the forces acted from this event could have caused a reopening of faults caused by the tension forces and depression of the Oceanic Plate. The Japan Trench observed at approximately 9.8 - 10 s matched very well with the findings by the mentioned papers, which also meant that the migration was successfully performed at large depths.

A depth migration is a very high demand where the final processing step should contain as less errors as possible. Running a *smooth* depth migration was difficult as they were large factors that need to be in control to obtain satisfactory results. The experimental full wave acoustic pre-stack depth migration in Madagascar revealed that large velocity variations in the model affected the migration as theoretically expected. Pre-stack depth migrations are generally sensitive to migration, and hence showed how the depth migration performed with unstable velocity models (Fig. 6.23) where the depth migration follows the theory of ray-tracing, which the Kirchhoff time migration does not. It could be said that the TQC stacks compensated for what Kirchhoff migration was lacking, which is the ray-tracing theory. However, the TQC stacks are not considered as time migrated stacks as they are only converted to time using the depth velocity models, which are laterally varying.

The depth migration was also beneficial to display reflectors at the shallow depths, which the Kirchhoff migration did not image properly. However, due to the instabilities, the increasing depths are actually wrong and not presentable for the actual depths observed in the surveys. The trench measured at Fig. 6.24 is approximately at 8.6 km depth, which was not realistic compared to the surveys processed by Tsuru et al. (2000) and Kodaira et al. (2017). The depth of the trench is actually approximately 7.3 km, which marked an error of 1.3 km (Appendix B, Fig. B.1). The errors were also present in the TQC stacks as displayed in Figs. 6.26 and 6.27, which meant that these stacks could not be used for realistic time-lapse measurements either.

8 | Conclusion and recommendation

The objectives of this thesis were to investigate various processing steps by using the open-source software Madagascar. Through this software, methods such as band-pass and debubble filters gave satisfactory results while despiking had its limitations concerning spike removal of many traces together in a data set. However, all the three mentioned processing steps hence gave a significant improvement from the raw data in both surveys.

Muting and velocity analysis were together the most crucial processing steps that revealed to be most disruptive towards the velocity model and hence towards the time and depth migration. Semblance mute was used as a compensation/guidance for the automatic picking algorithm to not pick multiples in the semblances. The obtained velocity models were still observed to be different from a realistic model, but accurate enough to flatten the primary reflectors and suppress multiples to a certain degree. It can be concluded that the most disadvantage with Madagascar was the automatic picker where the user theoretically did not have any control. However, picking a large number of velocities over a very large number of semblances is a highly time consuming process. Hence, it also showed the benefits of using Madagascar. To improve this, the user could either create a script for interactive picking of velocities, or try to combine different software such as picking velocities in Promax and converting them to Madagascar format afterwards. It can also be recommended to create a code including the angle parameter in *sfpick* to determine the velocity increase during automatic picking.

The only multiple attenuation performed was done through semblance muting where it could be recommended to do filtering methods such as Tau-P and radon to remove them. These do require correct parameters where many trial and failure attempts are expected, which in return could significantly improve the automatic picking algorithms and give a more realistic velocity model in Madagascar. Multiple suppression is hence also an important step to eliminate interpretations errors along with imaging deep depth reflectors. Hence, low-frequency studies can be beneficial on these surveys to observe whether there are visible deep depths reflectors, which can differentiate the crust layers even more in details.

The Kirchhoff time migration gave promising results in both surveys although some diffractions were still visible on shallow depths. Small anomalies were also observed at the shallow depths of the COI gathers and only affecting a small percentage. A higher aperture length in *sfmig2* could be performed to check if the remaining diffractions are collapsed, and to observe if tectonic features at large depths are imaged more clearly.

The migrated stacks were comparable in Petrel to reveal significant differences between the surveys as a possible consequence of the earthquake. The uplift and subsidence measurements were found to be comparable with nearby surveys and research, but might be not presentable for this particular area (2D line) due to the errors in the navigational shift. Only correct navigation can reveal the true measurements.

The Acoustic wave depth migration was unstable due to the velocity model caused by initial picked velocities, and began from the noise in the seawater. If motioned methods above does not suffice, an attempt on a detail mute in shot domain can be done before performing the velocity analysis, especially for the depth migration. This is however as mentioned, a time versus benefit process. The depth migration revealed structures at shallow depth in even more details, but not comparable with each other due to the instabilities.

Madagascar showed to be a beneficial software in processing where the user had more control over the data for each processing step. As the geometry of a survey is generally defined by a 3D cube, the user also knows where each trace is, which makes it easy to detect and remove. Hence, processing seismic data in Madagascar have proven to be beneficial through various steps such as band-pass, debubble and despiking steps, but restrictive on the top muting and velocity analysis to far.

References

- Amidror, I. (2002). Scattered data interpolation methods for electronic imaging systems: A survey. *Journal of Electronic Imaging*, 11(2):157–176.
- Bancroft, J. C., Geiger, H. D., and Margrave, G. F. (1998). The equivalent offset method of prestack time migration. *Geophysics*, 63(6):2042–2053.
- Barnes, G. L. (2003). Origins of the Japanese Islands: The New "Big Picture". *Japan review: journal of the International Research Center for Japanese Studies*, 15(15):3–50.
- Boston, B., Moore, G. F., Nakamura, Y., and Kodaira, S. (2014). Outer-rise normal fault development and influence on near-trench décollement propagation along the Japan Trench, off Tohoku. *Earth, Planets and Space*, 66(1):135.
- Etgen, J., Gray, S. H., and Zhang, Y. (2009). An overview of depth imaging in exploration geophysics. *Geophysics*, 74:WCA5.
- Fujii, Y., Satake, K., Sakai, S., Shinohara, M., and Kanazawa, T. (2011). Tsunami source of the 2011 off the Pacific coast of Tohoku Earthquake. *Earth, Planets and Space*, 63(7):55.
- Gadallah, M. R. and Fisher, L. (2005). *Applied seismology: a comprehensive guide to seismic theory and application*. PennWell.
- Gelius, L.-J. (2007). Introduction to seismic processing and imaging. Lecture notes in INF-GEO3310. University of Oslo.
- Hardy, R. (1999). Basic Seismic Processing For Interpreters. Retrieved on Nov 12th 2017 from <http://www.xsgeo.com/course/contents.htm>.
- Huene, V. R., Klaeschen, D., Cropp, B., and Miller, J. (1994). Tectonic structure across the accretionary and erosional parts of the Japan Trench margin. *Journal of Geophysical Research: Solid Earth*, 99(B11):22349–22361.
- IAGC (2002). Marine Seismic Operations. An overview. Retrieved on Nov 12th 2017 from https://www.cagc.ca/resources/marine_seismic/marine_seismic_operations_overview.pdf.
- Jamstec (2015). KR97-07 Velocity Structural Model. Retrieved on April 13th 2018 from https://www.jamstec.go.jp/jamstec-e/IFREE_center/data-e/cruise_data-e/KR97-07vmodel-e.html.

- Karazincir, M. H., Gerrard, C. M., Long, A., and Comeaux, L. B. (2008). Utilizing the two-way wave equation: Reverse time pre-stack depth migration. In *Proceedings, Indonesian Petroleum Association*. IPA.
- Kodaira, S., Nakamura, Y., Yamamoto, Y., Obana, K., Fujie, G., No, T., Kaiho, Y., Sato, T., and Miura, S. (2017). Depth-varying structural characters in the rupture zone of the 2011 tohoku-oki earthquake. *Geosphere*, 13(5):1408–1424.
- Kristensen, E. (2017). Time-lapse Seismic Analysis of the Tohoku Earthquake. Master's thesis, NTNU.
- Kwok, Y. T., E Bell, R., and Mochizuki, K. (2017). Characterizing the japan trench subduction margin in the vicinity of the 2011 tohoku earthquake using seismic reflection data. In *Earthquake Research Institute*.
- Landrø, M. (2011). *Seismic Data Acquisition and Imaging*. Trondheim: NTNU.
- Landrø, M. and Amundsen, L. (2018). *An Introduction to Exploration Geophysics with Recent Advances*. Trondheim: Bivrost.
- Lay, T. and Kanamori, H. (2011). Insights from the great 2011 Japan earthquake. *PHYSICS TODAY*, 64(12):33–39.
- Li, L. (2013). Technology management models for marine seismic acquisition projects. Master thesis, University of Stavanger, Norway.
- Madagascar Development Team (2018). *Madagascar Software, Version 2.0*. <http://www.ahay.org/>.
- McGuire, D. and Miller, B. (1989). The utility of single-point seismic data. *Bulletin*, 226:1–8.
- Nakamura, Y., Kodaira, S., Miura, S., Regalla, C., and Takahashi, N. (2013). High-resolution seismic imaging in the Japan Trench axis area off Miyagi, northeastern Japan. *Geophysical Research Letters*, 40(9):1713–1718.
- Onajite, E. (2013). *Seismic Data Analysis Techniques in Hydrocarbon Exploration*. Elsevier.
- Oren, C. and Nowack, R. L. (2018). An overview of reproducible 3d seismic data processing and imaging using madagascar. *GEOPHYSICS*, 83(2):F9–F20.
- Ozawa, S., Nishimura, T., Suito, H., Kobayashi, T., Tobita, M., and Imakiire, T. (2011). Coseismic and postseismic slip of the 2011 magnitude-9 Tohoku-Oki earthquake. *Nature*, 475(7356):373–6.
- Rigzone (2017). How Does Marine Seismic Work. Retrieved on Nov 12th 2017 from http://www.rigzone.com/training/insight.asp?i_id=303.
- Schulte, B. (2012). Overview on the Fundamentals of Imaging. *CSEG Recorder*, 37(10):40–48.
- Simm, R. and White, R. (2002). Phase, polarity and the interpreter's wavelet. *First Break*, 20:277 – 281.

- Simons, M., Minson, S. E., Staden, A., Ortega, F., Jiang, J., Owen, S. E., Meng, L., Ampuero, J.-P., Wei, S., Chu, R., Helmberger, D. V., Kanamori, H., Hetland, E., Moore, A. W., and Webb, F. H. (2011). The 2011 magnitude 9.0 Tohoku-Oki earthquake: mosaicking the megathrust from seconds to centuries. *Science*, 332(6036).
- Steinsbø, K.-G. (2013). Forward Seismic Forward Modeling of an Outcrop Model from Kvalvågen on Spitsbergen: Investigating Thin Layers and Complex Geological Structures. Master's thesis, Norwegian University of Science and Technology.
- Sun, T., Wang, K., Fujiwara, T., Kodaira, S., and He, J. (2017). Large fault slip peaking at trench in the 2011 tohoku-oki earthquake. *Nature Communications*, 8.
- Taira, A. (2001). Tectonic Evolution of the Japanese Island Arc System. *Annual Review of Earth and Planetary Sciences*, 29(1):109–134.
- Takahashi, N., Kodaira, S., Tsuru, T., Park, J., Kaneda, Y., Kinoshita, H., Abe, S., Nishino, M., and Hino, R. (2000). Detailed plate boundary structure off northeast Japan coast. *Geophysical Research Letters*, 27(13):1977–1980.
- Takahashi, N., Kodaira, S., Tsuru, T., Park, J.-O., Kaneda, Y., Suyehiro, K., Kinoshita, H., Abe, S., Nishino, M., and Hino, R. (2004). Seismic structure and seismogenesis off Sanriku region, northeastern Japan. *Geophysical Journal International*, 159(1):129–145.
- Tsuru, T., Park, J.-O., Miura, S., Kodaira, S., Kido, Y., and Hayashi, T. (2002). Along-arc structural variation of the plate boundary at the Japan Trench margin: Implication of interplate coupling. *Journal of Geophysical Research B: Solid Earth*, 107(B12):ESE 11–1–ESE 11–15.
- Tsuru, T., Park, J.-O., Takahashi, N., Kodaira, S., Kido, Y., Kaneda, Y., and Kono, Y. (2000). Tectonic features of the Japan Trench convergent margin off Sanriku, northeastern Japan, revealed by multichannel seismic reflection data. *Journal of Geophysical Research: Solid Earth*, 105(B7):16403–16413.
- Weibull, W. W. (2017). Sfdatarg3d (version 1.7) [program].
- Yang, C. (2012). Time-lapse Analysis of Borehole and Surface Seismic Data, and Reservoir Characterization of the Ketzin CO₂ Storage Site, Germany. Digital Comprehensive Summaries of Uppsala Dissertations from the Faculty of Science and Technology, 2012.

Appendices

A Madagascar processing workflow

A.1 Data regulation and geometry correction

```
from rsf.proj import *

#Convert datafiles to RSF

#old Read segy and convert
Flow(['sr_data', 'sr_hdr', 'sr_info.txt'], '../data_sgy/raw/sr101_shot_wotn.sgy', 'segread
→  tape=${SOURCES[0]} tfile=${TARGETS[1]} hfile=${TARGETS[2]}')

#new Readseggy and convert

#part 1
Flow(['D19_data_1', 'D19_hdr_1', 'D19_info_1.txt'],
→  '../data_sgy/raw/D19_shot_wotn_1-4.5k.sgy', 'segread tape=${SOURCES[0]}
→  tfile=${TARGETS[1]} hfile=${TARGETS[2]} ')

#part 2
Flow(['D19_data_2', 'D19_hdr_2', 'D19_info_2.txt'],
→  '../data_sgy/raw/D19_shot_wotn_sp4.5k-end.sgy', 'segread tape=${SOURCES[0]}
→  tfile=${TARGETS[1]} hfile=${TARGETS[2]} ')

#merge D19 data
Flow('D19_data_merged.rsf', ['D19_data_1', 'D19_data_2'], 'sfcat axis=2')
Flow('D19_hdr_merged.rsf', ['D19_hdr_1', 'D19_hdr_2'], 'sfcat axis=2')

#header rotation
Flow('sr_hdr_fix', 'sr_hdr', 'sfheaderrot theta=0.0 xshift=-3.5e8 yshift=-3.5e9 factor=0.01
→  out=stdout')
Flow('D19_hdr_fix', 'D19_hdr_merged.rsf', 'sfheaderrot theta=0 xshift=-3.5209e8 yshift=-3.5013e9
→  factor=0.01 out=stdout')

Flow('sr_hdr_rot', 'sr_hdr_fix', 'sfheaderrot theta=-9.73 yshift=39362808.00 xshift=4157085.0
→  out=stdout')
Flow('D19_hdr_rot', 'D19_hdr_fix.rsf', 'sfheaderrot theta=-6.585 yshift=39362650 xshift=4157971
→  out=stdout')

# Create headerfile - 2D predatum plane
Flow('sr_2d_hdr', None, 'sfmakehdr2d az=90.0 dg=25 ds=50 minoff=200 ng=120 ns=5494 scalco=1 sx0=0
→  sy0=0 verb=1 out=stdout')
Flow('D19_2d_hdr', None, 'sfmakehdr2d az=90.0 dg=12.5 ds=50 minoff=159.24 ng=444 ns=4201 scalco=1
→  sx0=0 sy0=0 verb=1 out=stdout')

#Using interpolate method with modified shepads method
Flow(['sr_2d_data'], 'sr_data sr_hdr_rot sr_2d_hdr', 'datareg3d R=400.0 wo=2.0 wx=1.0 wy=1.0
→  wa=0.0 head=${SOURCES[1]} head_i=${SOURCES[2]} verb=1 DMO=1 out=stdout')
Flow(['D19_2d_data'], 'D19_data_merged D19_hdr_rot D19_2d_hdr', 'datareg3d R=2000.0 wo=2.0 wx=1.0
→  wy=1.0 wa=0.0 head=${SOURCES[1]} head_i=${SOURCES[2]} verb=1 DMO=1')

#Put parameters, min offs, interval etc.
Flow(['sr1_data_base'], ['sr_2d_data'], 'put d2=25 n2=120 o2=200 o3=0.0 d3=50 n3=5494')
Flow(['D1_data_rbase'], ['D19_2d_data'], 'put d2=12.5 n2=444 o2=159.24 o3=0.0 d3=50 n3=4201
→  |sfwindow d1=0.004 out=stdout')
```

A.2 Frequency filter, despiking and debubble filter

```
#!/bin/sh

#Bandpass filter
sfbandpass < sr1_data_base.rsrf flo=2 fhi=50 phase=n nplo=8 nphi=8 > sr2_data_flt.rsrf
sfbandpass < D1_data_despike.rsrf flo=2 fhi=50 phase=n nplo=8 nphi=8 > D2_data_flt.rsrf

#Despiking
sfdespike2 < sr2_data_flt.rsrf wide2=3 > sr3_data_flt_despiked.rsrf
sfdespike2 < D2_data_flt.rsrf wide2=3 > D3_data_flt_despiked.rsrf

# Debubble filter

#Spike with survey geometry
sfspike mag=15 nsp=2 n1=3501 n3=5494 n2=1 k1=31 dt=0.004 o1=0.04 o2=0 > sr_spike.rsrf
sfspike mag=15 nsp=2 n1=4501 n3=4201 n2=1 k1=26 dt=0.004 o1=0 o2=0 out=stdout > d_spike.rsrf

#Ricker wavelets
sfricker1 < sr_spike.rsrf frequency=20 out=stdout > sr_rckr.rsrf
sfricker1 < d_spike.rsrf frequency=20 out=stdout > d_rckr.rsrf

#create shaping data

sfshape < sr3_data_flt_despiked.rsrf shapeout=.sr_dout.rsrf showshaper=1 pnoise=0.1 nshape=200
→ dfile=sr_rckr.rsrf wfile=sr3_data_flt_despiked.rsrf out=stdout > sr_shape.rsrf
sfshape < D3_data_flt_despiked.rsrf shapeout=d_dout.rsrf showshaper=1 pnoise=5 nshape=200
→ dfile=d_rckr.rsrf wfile=D3_data_flt_despiked.rsrf out=stdout > d_shape.rsrf

#convolve using sfshape2
sfshape2 < sr3_data_flt_despiked.rsrf shaper=sr_dout.rsrf out=stdout >
→ sr4_data_flt_despiked_debl.rsrf
sfshape2 < D3_data_flt_despiked.rsrf shaper=d_dout.rsrf out=stdout >
→ D4_data_flt_despiked_debl.rsrf
```

A.3 Top mute

```
#!/bin/sh

#Separating data into smaller parts

#SR
sfwindow < sr4_data_flt_despiked_debl.rsrf f3=0 n3=1000 |sfput o3=0 out=stdout > p1.rsrf
sfwindow < sr4_data_flt_despiked_debl.rsrf f3=1000 n3=1000 |sfput o3=0 out=stdout > p2.rsrf
sfwindow < sr4_data_flt_despiked_debl.rsrf f3=2000 n3=1000 |sfput o3=0 out=stdout > p3.rsrf
sfwindow < sr4_data_flt_despiked_debl.rsrf f3=3000 n3=2494 |sfput o3=0 out=stdout > p4.rsrf

#D19
sfwindow < D4_data_flt_despike_debl.rsrf f3=0 n3=1000 |sfput o3=0 out=stdout > n1.rsrf
sfwindow < D4_data_flt_despike_debl.rsrf f3=1000 n3=1000 |sfput o3=0 out=stdout > n2.rsrf
sfwindow < D4_data_flt_despike_debl.rsrf f3=2000 n3=1000 |sfput o3=0 out=stdout > n3.rsrf
sfwindow < D4_data_flt_despike_debl.rsrf f3=3000 n3=1201 |sfput o3=0 out=stdout > n4.rsrf

#mute and merge
sfmutter <p1.rsrf half=n t0=1.80 v0=2700 out=stdout > p1_m.rsrf
sfmutter <p2.rsrf half=n t0=2.5 v0=3700 out=stdout > p2_m.rsrf
sfmutter <p3.rsrf half=n t0=4.0 v0=4800 out=stdout > p3_m.rsrf
sfmutter <p4.rsrf half=n t0=5.4 v0=5000 out=stdout > p4_m.rsrf

sfcat < p1_m.rsrf p2_m.rsrf p3_m.rsrf p4_m.rsrf axis=3 d2=25 |sfwindow f1=0 n1=3375 >
→ sr5_data_FDD_muted.rsrf

sfmutter <n1.rsrf half=n t0=1.35 v0=2700 out=stdout >n1_m.rsrf
sfmutter <n2.rsrf half=n t0=2.5 v0=3700 out=stdout >n2_m.rsrf
sfmutter <n3.rsrf half=n t0=4.0 v0=4800 out=stdout >n3_m.rsrf
sfmutter <n4.rsrf half=n t0=5.4 v0=4800 out=stdout >n4_m.rsrf

sfcat < n1_m.rsrf n2_m.rsrf n3_m.rsrf n4_m.rsrf axis=3 d2=12.5 out=stdout > D5_data_FDD_muted.rsrf
```

A.4 CMP sorting, velocity analysis, NMO correction and stacking

```
#!/bin/sh

# From shot gathers to CMP gathers.
sfshot2cmp < sr5_data_FDD_muted.rs f half=n out=stdout |sfwindow f2=1 n2=29 >
  → sr6_data_CMP_cut.rs f
sfshot2cmp < D5_data_FDD_muted.rs f half=n out=stdout > D6_data_FDD_CMP.rs f

# Separation of CMP data prior to velocity analysis
sfwindow < sr5_data_CMP_cut.rs f f3=0 n3=7500 |sfput o2=300 o3=100 > sr_CMP_part1.rs f
sfwindow < sr5_data_CMP_cut.rs f f3=7500 n3=7500 |sfput o2=300 o3=100 > sr_CMP_part2.rs f
sfwindow < sr5_data_CMP_cut.rs f f3=15000 n3=7095 |sfput o2=300 o3=100 > sr_CMP_part3.rs f

sfwindow < D5_data_FDD_CMP.rs f f3=0 n3=12000 |sfput o2=159.24 o3=79.62 > D_CMP_part1.rs f
sfwindow < D5_data_FDD_CMP.rs f f3=12000 n3=11000 |sfput o2=159.24 o3=79.62 > D_CMP_part2.rs f
sfwindow < D5_data_FDD_CMP.rs f f3=23000 n3=11051 |sfput o2=159.24 o3=79.62 > D_CMP_part3.rs f

#Velocity scan
sfvscan < sr_CMP_part1.rs f half=n v0=1480 nv=150 dv=25 semblance=y > sr_vels_p1n.rs f
sfvscan < sr_CMP_part2.rs f half=n v0=1480 nv=150 dv=25 semblance=y > sr_vels_p2n.rs f
sfvscan < sr_CMP_part3.rs f half=n v0=1480 nv=150 dv=25 semblance=y > sr_vels_p3n.rs f

sfvscan < D_CMP_part1.rs f half=n v0=1480 nv=150 dv=25 semblance=y > D19_vels_p1n.rs f
sfvscan < D_CMP_part2.rs f half=n v0=1480 nv=150 dv=25 semblance=y > D19_vels_p2n.rs f
sfvscan < D_CMP_part3.rs f half=n v0=1480 nv=150 dv=25 semblance=y > D19_vels_p3n.rs f

# Semblance muting and picking

#SR
#part 1
sfwindow < sr_vels_p1n.rs f f3=0 n3=2000 out=stdout > sp1.rs f
sfwindow < sr_vels_p1n.rs f f3=2000 n3=2000 out=stdout > sp2.rs f
sfwindow < sr_vels_p1n.rs f f3=4000 n3=2000 out=stdout > sp3.rs f
sfwindow < sr_vels_p1n.rs f f3=6000 n3=2500 out=stdout > sp4.rs f

sfmutter < sp1.rs f half=n t0=3 x0=1350 v0=140 inner=y |sfmutter half=n t0=4.0 x0=1450 v0=220
  → inner=y > sp1_m.rs f
sfmutter < sp2.rs f half=n t0=4.0 x0=1400 v0=150 inner=y |sfmutter half=n t0=5.0 x0=1500 v0=250
  → inner=y > sp2_m.rs f
sfmutter < sp3.rs f half=n t0=5.0 x0=1450 v0=160 inner=y |sfmutter half=n t0=6.5 x0=1500 v0=270
  → inner=y > sp3_m.rs f
sfmutter < sp4.rs f half=n t0=7.5 x0=1350 v0=170 inner=y |sfmutter half=n t0=8.0 x0=1500 v0=280
  → inner=y > sp4_m.rs f

sfcat < sp1_m.rs f sp2_m.rs f sp3_m.rs f sp4_m.rs f axis=3 d3=12.5 > sr_vels_p1_muted.rs f

sfpick < sr_vels_p1_muted.rs f vel0=1480 an=8 rect1=10 rect2=10 smooth=y > sr_velp_p1_muted.rs f

#part2
sfwindow < sr_vels_p2n.rs f f3=0 n3=1000 out=stdout > s2p1.rs f
sfwindow < sr_vels_p2n.rs f f3=1000 n3=1000 out=stdout > s2p2.rs f
sfwindow < sr_vels_p2n.rs f f3=2000 n3=2000 out=stdout > s2p3.rs f
sfwindow < sr_vels_p2n.rs f f3=4000 n3=2500 out=stdout > s2p4.rs f

sfmutter < s2p1.rs f half=n t0=7.5 x0=1350 v0=80 inner=y |sfmutter half=n t0=9.0 x0=1450 v0=100
  → inner=y > s2p1_m.rs f
sfmutter < s2p2.rs f half=n t0=9 x0=1400 v0=85 inner=y |sfmutter half=n t0=11.0 x0=1450 v0=120
  → inner=y > s2p2_m.rs f
sfmutter < s2p3.rs f half=n t0=10 x0=1400 v0=90 inner=y |sfmutter half=n t0=11 x0=1450 v0=160
  → inner=y > s2p3_m.rs f
sfmutter < s2p4.rs f half=n t0=9 x0=1350 v0=100 inner=y |sfmutter half=n t0=10 x0=1450 v0=200
  → inner=y > s2p4_m.rs f

sfcat < s2p1_m.rs f s2p2_m.rs f s2p3_m.rs f s2p4_m.rs f axis=3 d3=12.5 > sr_vels_p2_muted.rs f
sfpick < sr_vels_p2_muted.rs f vel0=1480 an=8 rect1=10 rect2=10 smooth=y > sr_velp_p2_muted.rs f

#part3
sfwindow < sr_vels_p3n.rs f f3=0 n3=1000 out=stdout > s3p1.rs f
sfwindow < sr_vels_p3n.rs f f3=1000 n3=2000 out=stdout > s3p2.rs f
sfwindow < sr_vels_p3n.rs f f3=3000 n3=2000 out=stdout > s3p3.rs f
sfwindow < sr_vels_p3n.rs f f3=5000 n3=2095 out=stdout > s3p4.rs f
```

```

sfmutter <s3p1.rsrf half=n t0=8.0 x0=1400 v0=25 inner=y |sfmutter half=n t0=9.0 x0=1450 v0=150
→ inner=y >s3p1_m.rsrf
sfmutter <s3p2.rsrf half=n t0=7.9 x0=1400 v0=30 inner=y |sfmutter half=n t0=8.6 x0=1450 v0=160
→ inner=y >s3p2_m.rsrf
sfmutter <s3p3.rsrf half=n t0=7.85 x0=1400 v0=35 inner=y |sfmutter half=n t0=8.4 x0=1450 v0=170
→ inner=y >s3p3_m.rsrf
sfmutter <s3p4.rsrf half=n t0=7.80 x0=1350 v0=40 inner=y |sfmutter half=n t0=8.3 x0=1450 v0=180
→ inner=y >s3p4_m.rsrf

sfcat < s3p1_m.rsrf s3p2_m.rsrf s3p3_m.rsrf s3p4_m.rsrf axis=3 d3=12.5 > sr_vels_p3_muted.rsrf
sfpick < sr_vels_p3_muted.rsrf vel0=1480 an=8 rect1=10 rect2=10 smooth=y > sr_velp_p3_muted.rsrf

#merge
sftransp <sr_velp_p1_muted.rsrf plane=23 memsize=10000 >sr_velp_p1_t.rsrf
sftransp <sr_velp_p2_muted.rsrf plane=23 memsize=10000 >sr_velp_p2_t.rsrf
sftransp <sr_velp_p3_muted.rsrf plane=23 memsize=10000 >sr_velp_p3_t.rsrf

sfcat < sr_velp_p1_t.rsrf sr_velp_p2_t.rsrf sr_velp_p3_t.rsrf axis=3 out=stdout >
→ sr_velprof_muted_t.rsrf
sftransp <sr_velprof_muted_t.rsrf plane=23 memsize=10000 > sr_velprof_muted.rsrf

#D19
sfwindow < D19_vels_p1n.rsrf f3=0 n3=4000 > dp1.rsrf
sfwindow < D19_vels_p1n.rsrf f3=4000 n3=4000 > dp2.rsrf
sfwindow < D19_vels_p1n.rsrf f3=8000 n3=2000 > dp3.rsrf
sfwindow < D19_vels_p1n.rsrf f3=10000 n3=2000 > dp4.rsrf

sfmutter <dp1.rsrf half=n t0=2.4 x0=1350 v0=130 inner=y |sfmutter half=n t0=3.3 x0=1450 v0=175
→ inner=y >dp1_m.rsrf
sfmutter <dp2.rsrf half=n t0=3.4 x0=1400 v0=150 inner=y |sfmutter half=n t0=4.0 x0=1500 v0=175
→ inner=y >dp2_m.rsrf
sfmutter <dp3.rsrf half=n t0=4.0 x0=1450 v0=150 inner=y |sfmutter half=n t0=4.4 x0=1500 v0=200
→ inner=y >dp3_m.rsrf
sfmutter <dp4.rsrf half=n t0=4.4 x0=1350 v0=150 inner=y |sfmutter half=n t0=5.4 x0=1500 v0=200
→ inner=y >dp4_m.rsrf

sfcat < dp1_m.rsrf dp2_m.rsrf dp3_m.rsrf dp4_m.rsrf axis=3 d3=12.5 > d_vels_p1_muted.rsrf
sfpick < d_vels_p1_muted.rsrf vel0=1480 an=8 rect1=10 rect2=10 smooth=y > d_velp_p1_muted.rsrf

sfwindow < D19_vels_p2n.rsrf f3=0 n3=3000 > d2p1.rsrf
sfwindow < D19_vels_p2n.rsrf f3=3000 n3=3000 > d2p2.rsrf
sfwindow < D19_vels_p2n.rsrf f3=6000 n3=3000 > d2p3.rsrf
sfwindow < D19_vels_p2n.rsrf f3=9000 n3=2000 > d2p4.rsrf

sfmutter <d2p1.rsrf half=n t0=4.75 x0=1400 v0=120 inner=y |sfmutter half=n t0=6.5 x0=1500 v0=160
→ inner=y >d2p1_m.rsrf
sfmutter <d2p2.rsrf half=n t0=6.6 x0=1400 v0=130 inner=y |sfmutter half=n t0=7.6 x0=1450 v0=180
→ inner=y >d2p2_m.rsrf
sfmutter <d2p3.rsrf half=n t0=7.5 x0=1400 v0=140 inner=y |sfmutter half=n t0=8.0 x0=1450 v0=290
→ inner=y >d2p3_m.rsrf
sfmutter <d2p4.rsrf half=n t0=8.0 x0=1350 v0=150 inner=y |sfmutter half=n t0=8.5 x0=1450 v0=200
→ inner=y >d2p4_m.rsrf

sfcat < d2p1_m.rsrf d2p2_m.rsrf d2p3_m.rsrf d2p4_m.rsrf axis=3 d3=12.5 > d_vels_p2_muted.rsrf
sfpick < d_vels_p2_muted.rsrf vel0=1480 an=8 rect1=10 rect2=10 smooth=y > d_velp_p2_muted.rsrf

sfwindow < D19_vels_p3n.rsrf f3=0 n3=3000 > d3p1.rsrf
sfwindow < D19_vels_p3n.rsrf f3=3000 n3=3000 > d3p2.rsrf
sfwindow < D19_vels_p3n.rsrf f3=6000 n3=3000 > d3p3.rsrf
sfwindow < D19_vels_p3n.rsrf f3=9000 n3=2051 > d3p4.rsrf

sfmutter <s3p1.rsrf half=n t0=8.0 x0=1400 v0=25 inner=y |sfmutter half=n t0=9.0 x0=1450 v0=150
→ inner=y >s3p1_m.rsrf
sfmutter <s3p2.rsrf half=n t0=7.9 x0=1400 v0=30 inner=y |sfmutter half=n t0=8.6 x0=1450 v0=160
→ inner=y >s3p2_m.rsrf
sfmutter <s3p3.rsrf half=n t0=7.85 x0=1400 v0=35 inner=y |sfmutter half=n t0=8.4 x0=1450 v0=170
→ inner=y >s3p3_m.rsrf
sfmutter <s3p4.rsrf half=n t0=7.80 x0=1350 v0=40 inner=y |sfmutter half=n t0=8.3 x0=1450 v0=180
→ inner=y >s3p4_m.rsrf

sfcat < d3p1_m.rsrf d3p2_m.rsrf d3p3_m.rsrf d3p4_m.rsrf axis=3 d3=12.5 > d_vels_p3_muted.rsrf
sfpick < d_vels_p3_muted.rsrf vel0=1480 an=8 rect1=10 rect2=10 smooth=y > d_velp_p3_muted.rsrf

#merge
sftransp <d_velp_p1_muted.rsrf plane=23 memsize=10000 >d_velp_p1_t.rsrf
sftransp <d_velp_p2_muted.rsrf plane=23 memsize=10000 >d_velp_p2_t.rsrf

```

```

sftransp <d_velp_p3_muted.rs f plane=23 memsize=10000 >d_velp_p3_t.rs f

sfcat < d_velp_p1_t.rs f d_velp_p2_t.rs f d_velp_p3_t.rs f axis=3 out=stdout >
→ d_velprof_muted_t.rs f
sftransp <d_velprof_muted_t.rs f plane=23 memsize=10000 > d_velprof_muted.rs f

sfsmooth <d_velprof_muted.rs f rect1=100 rect2=150 > d_velprof_smoothed_muted.rs f

#NMO correction and stacking

sfnm0 < sr5_data_CMP_cut.rs f velocity=./cmp/sr_velprof_muted_smooth.rs f half=n out=stdout >
→ sr6_NMO_crd.rs f
sfstack < sr6_NMO_crd.rs f axis=2 rms=n out=stdout > sr_stack.rs f

sfnm0 < D5_data_FDD_CMP.rs f velocity=d_velprof_smoothed_muted.rs f half=n out=stdout >
→ D6_NMO_crd.rs f
sfstack < D6_NMO_crd.rs f axis=2 rms=n out=stdout > D_stack.rs f

```

A.5 Kirchhoff Pre-stack time migration

```

#!/bin/sh

#transpose the data
sftransp < sr5_data_CMP_cut.rs f plane=23 memsize=10000 > sr5_data_CMP_t.rs f
sftransp < D5_data_FDD_CMP.rs f plane=23 memsize=1000000 > D5_data_CMP_t.rs f

sfmig2 < sr5_data_CMP_t.rs f verb=y half=n apt=40 vel=sr_velprof_muted_smooth.rs f
→ gather=sr_tgather_apt40.rs f out=stdout > sr_tmig_apt40.rs f
sfmig2 < D5_data_CMP_t.rs f verb=y half=n apt=40 vel=d_velprof_smoothed_muted.rs f
→ gather=d_tgather_apt40.rs f > d_tmig_apt40.rs f

```

A.6 Full acoustic wave pre-stack depth migration

```

#!/bin/bash

#Dix conversion and smoothing
sfdix < sr_velprof_muted_smooth.rs f rect1=50 rect2=200 |sfclip2 lower=1480 > sr_velprof_dix.rs f
sfdix < d_velprof_smoothed_muted.rs f rect1=50 rect2=500 |sfclip2 lower=1480 |sfwindow f1=0
→ n1=3375 > d_velprof_dix.rs f

#Depth conversion of velocity models
sftime2depth <sr_velprof_dix.rs f dz=2.5 nz=4800 velocity=sr_velprof_dix.rs f intime=y twoway=y
→ |sfput label1="Depth" unit1="m" title="V(z)" > sr_velprof_depth.rs f
sftime2depth <d_velprof_dix.rs f dz=2.5 nz=4800 velocity=d_velprof_dix.rs f intime=y twoway=y
→ |sfput label1="Depth" unit1="m" title="V(z)" > d_velprof_depth.rs f

#smoothing
sfsmooth < sr_velprof_depth.rs f rect1=250 rect2=750 |sfclip2 lower=1480 > sr_VP_final.rs f
sfsmooth < d_velprof_depth.rs f rect1=250 rect2=750 |sfclip2 lower=1480 > d_VP_final.rs f

#Pre-stack depth migration using Cluster

# For SR shot gathers

#
#SBATCH -J s_apt4 # Sensible name for the job
#SBATCH -p IPT # Partition IPT or EPT
#SBATCH -N 5 # Allocate 5 nodes for the job
#SBATCH -n 100 # 100 tasks total
#SBATCH --mem=110000 # Memory per node in MegaBytes
#SBATCH --exclusive # No other jobs on the nodes while job is running
#SBATCH -t 48:0:0 # Upper time limit of 12 hours for the job

##SBATCH -A <accountName> # the account this job will be submitted under
##SBATCH -p longq # Selected Q, if you want more then 2 hours use the "longq"

```



```

# Make a wavelet
sfwavelet f0=20 t0=0.1 dt=4.0e-03 tend=13.5 order=1 |sfft1 out=stdout > sr_wav.rs

sfmakehdr3d nsx=5494 ngx=120 dsx=50.0 dgx=25.0 sx0=0 gx0=200 scalco=-1 out=stdout > sr_hdr.rs

# Sort header and create a shotmap
sfheadersplit headin=sr_hdr.rs headout=sr_hdr_sorted.rs map=sr_shotmap.rs verb=1

# Create unstructured data file
#The migration needs an unstructured collection of traces as input. n2 must contain the number
→ of traces. The shotmap contain info about shots.
sfput n2=659280 n3=1 < sr5_data_FDD_muted.rs > sr_shots.rs

# Migrate data using MPI and sfmpicwem
mpirun -np 100 --bynode \${RSFROOT}/bin/sfmpicwem \
    Lpml=10 \
    verb=1 \
    Prec=sr_shots.rs \
    apert2=4000 \
    gx=gx.rs \
    sx=sx.rs \
    vp=sr_VP_final.rs \
    fw_P=fw.rs \
    bw_P=bw.rs \
    hdr=sr_hdr_sorted.rs \
    shotmap=sr_shotmap.rs \
    source=sr_wav.rs \
    image=migimage.rs \
    zsource=2 \
    zrec=3 \
    free_surface=0 \
    temppath="Tmp" \
    datapath="." \
    localpath="/scratch" \
    workpath="." \

#Prec is the data input file
#apert2 is the size of the local velocity model. This is a model with the source
#positioned in the middle and created for each shot during migration.
#gx,sx are output files not really used.
#fw and bw are the downgoing (fw) and upgoing wavefields created by the migration program.
#hdr is a sorted header
#shotmap is a map connecting shot gathers and input file.
#source is the source wavelet for the downgoing wavefield.
#image is the output from each migrated shot
#zsource is the depth of the source (gridpoints)
#zrec is the depth of the receiver array (gridpoints)
#temppath is a directory for temporary storage of migration output
#datapath is the path to the data input file
#workpath is a directory where the script is started

#Stack individual images listed in stacklist.txt into a stack
mpirun -np 100 sfmpistackcip2d clean=1 getpos=0 min_x=0 max_x=276190 listfile=stacklist.txt
→ stack=sr_dmig_final.rs verb=1 out=stdout

#Same configuration is done for D19 and hence not shown. The only difference for the monitor
→ survey is as following:

mpirun -np 100 sfmpistackcip2d clean=0 getpos=0 min_x=0 max_x=212818.75 listfile=stacklist.txt
→ stack=d_dmigstack_apt4000.sf verb=1

#Reverse quality control of depth migration through convection from depth to time
sfdepth2time < sr_dmig_final.rs velocity=sr_VP_final.rs slow=n t0=0 dt=0.004 nt=3375
→ out=stdout > sr_dmig_final_tQC.rs
sfdepth2time < d_dmig_final.rs velocity=d_VP_final.rs t0=0 dt=0.004 nt=3375 out=stdout >
→ d_dmig_final_tQC.rs

```

A.7 Amplitude correction and Conversion from RSF to SGY

```
#!/bin/sh

#Amplitude recovery/gain correction
sfshapeagc < sr_stack.rsf rect1=1000 > sr_stackG.rsf
sfshapeagc < sr_tmig.rsf rect1=1000 > sr_tmigG.rsf
sfshapeagc < sr_dmig_final.rsf rect1=1000 > sr_dmig_finalG.rsf
sfshapeagc < sr_dmig_final_tQC.rsf rect1=1000 > sr_dmig_final_tQCG.rsf

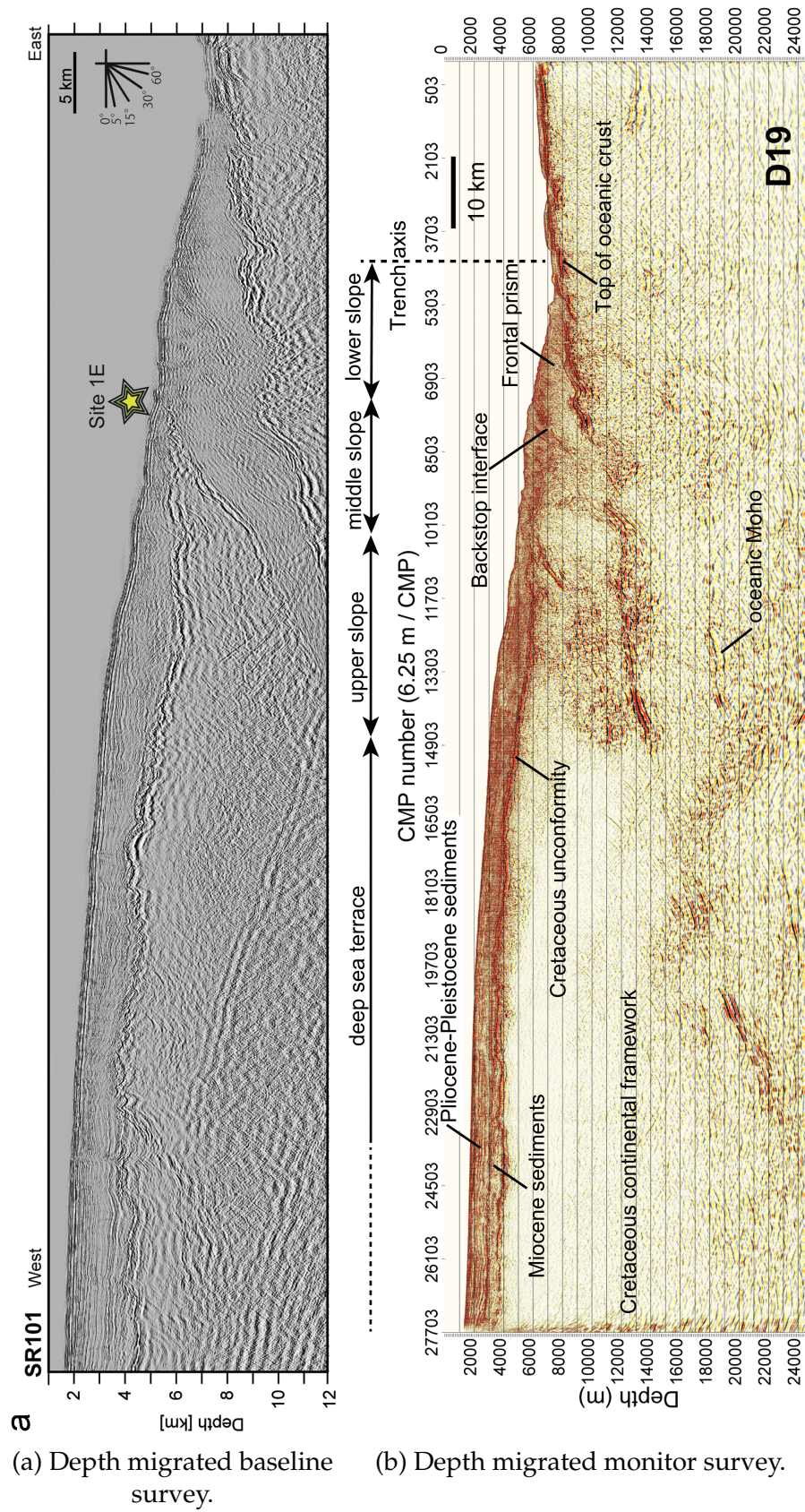
sfshapeagc < d_stack.rsf rect1=1000 > d_stackG.rsf
sfshapeagc < d_tmig.rsf rect1=1000 > d_tmigG.rsf
sfshapeagc < d_dmig_final.rsf rect1=1000 > d_dmig_finalG.rsf
sfshapeagc < d_dmig_final_tQC.rsf rect1=1000 > d_dmig_final_tQCG.rsf

#Headerfile for SGY with the shift 18250 m. to East.
sfmakehdr3d nsx=22095 dsx=12.5 nt=3375 dt=0.004 scalco=-100 sx0=18250 sy=0 out=stdout >
  → s_tfile_shifted.rsf
sfmakehdr3d nsx=17026 dsx=12.5 nt=4501 dt=0.004 scalco=-100 sx0=0 sy0=0 out=stdout > d_tfile.rsf

#Following migrated stacks were converted to SGY
sfsegywrite < sr_tmig.rsf tfile=s_tfile_shifted.rsf tape=sr_tmig.sgy verb=1 > sr_tmig.sgy
sfsegywrite < sr_dmig_finalG.rsf.rsf tfile=s_tfile_shifted.rsf tape=sr_dmig_finalG.sgy verb=1 >
  → sr_dmig_finalG.sgy
sfsegywrite < sr_dmig_final_tQCG.rsf.rsf tfile=s_tfile_shifted.rsf tape=sr_dmig_final_tQCG.sgy
  → verb=1 > sr_dmig_final_tQCG.sgy

sfsegywrite < d_tmig.rsf tfile=d_tfile_shifted.rsf tape=d_tmig.sgy verb=1 > d_tmig.sgy
sfsegywrite < d_dmig_finalG.rsf.rsf tfile=d_tfile_shifted.rsf tape=d_dmig_finalG.sgy verb=1 >
  → d_dmig_finalG.sgy
sfsegywrite < d_dmig_final_tQCG.rsf.rsf tfile=d_tfile_shifted.rsf tape=d_dmig_final_tQCG.sgy
  → verb=1 > d_dmig_final_tQCG.sgy
```

B Figures



(a) Depth migrated baseline survey.

(b) Depth migrated monitor survey.

Figure B.1: Sections of the baseline and monitor surveys, which are depth migrated stacks by Kwok et al. (2017) and Kodaira et al. (2017).